

Analysing and Modelling Particle Distributions in Near-Earth Space: Machine Learning

Mayur Rajesh Bakrania

Mullard Space Science Laboratory

University College London

May 3, 2022

A dissertation submitted in partial fulfillment

of the requirements for the degree of

Doctor of Philosophy

of

University College London

I, Mayur Rajesh Bakrania, confirm that the work presented in this thesis is my own.
Where information has been derived from other sources, I confirm that this has been indicated in the work.

Please note that some of the contents of this thesis have been previously reported in the following journal papers:

- Bakrania et al. ‘Statistics of solar wind electron breakpoint energies using machine learning techniques’. *A&A*, 639 A46. (2020).
- Bakrania et al. ‘Using dimensionality reduction and clustering techniques to classify space plasma regimes’. *Front. Astron. Space Sci.* (2020).
- Bakrania et al. ‘Direct evidence of magnetic reconnection onset via the tearing instability’. (Under Review).

Abstract

This thesis contains the analysis of 10 years of ESA Cluster observations using machine learning techniques. In the first study, we investigate solar wind electron populations at 1 au. In the second study, we apply a novel machine learning technique to magnetotail data in order to better characterise particle distribution function. In the third study, we make the first in-situ observations of the tearing instability leading to magnetic reconnection in the magnetotail.

Solar wind electron velocity distributions at 1 au consist of three main populations: the thermal ‘core’ population and two suprathermal populations called halo and strahl. We apply unsupervised algorithms to phase space density distributions, to perform a statistical study of how the core/halo and core/strahl breakpoint energies vary. The results of our statistical study show a significant decrease in both breakpoint energies against solar wind speed. By fitting Maxwellians to the core, based on our study, we can discuss the relative importance of the core temperature on halo and strahl electrons.

Collisionless space plasma environments are characterised by distinct particle populations that typically do not mix. Although moments of their velocity distributions help in distinguishing different plasma regimes, the distribution functions themselves provide more comprehensive information about the plasma state. By applying dimensionality reduction and clustering methods to electron distributions in pitch angle and energy space, we distinguish between the different plasma regions. We identify several new distinct groups of distributions, that are dependent upon significantly more complex plasma and field dynamics.

Magnetic reconnection is a fundamental mechanism responsible for explosive energy

release in space and laboratory plasmas. The onset of reconnection is via the tearing instability. Due to its elusive nature, there is an absence of in-situ observations of the tearing instability. We present the first direct observations of the tearing instability and the subsequent evolution of plasma electrons and reconnection, using neural network outlier detection methods. Our analysis of the tearing instability and subsequent reconnection provides new insights into the fundamental understanding of the mechanism responsible for reconnection.

Impact Statement

We set out to understand the breakpoint energy between the thermal and non-thermal parts of a solar wind electron distribution. Characterising the breakpoint energy is important as this property of a distribution function provides a diagnostic of the relative importance of scattering mechanisms such as Coulomb collisions and wave-particle interactions. These mechanisms determine the shape of electron distribution functions in both solar wind and astrophysical plasmas. In addition to these benefits, understanding the location of this cut-off, using only a statistical analysis of the data, provides useful limiting parameters for future studies which require multi-component fits to the total electron velocity distribution.

Machine learning provides us with a robust method of classification from which fine variations of electron populations in relation to energy and pitch angle can be derived, with the advantage of not requiring prior assumptions of the distributions of these populations. Applying machine learning techniques to a large dataset builds upon previous empirical studies of the suprathermal breakpoint energy. By classifying individual electron distributions, we characterise solar wind electron populations on a higher energy resolution than previous studies. As a result, our method enables breakpoint energy to be explored further with respect to other solar wind parameters, and by doing so we draw physical conclusions based on the relationship between this fundamental property and each parameter, for both the halo and the strahl. Machine learning techniques will become increasingly important with the anticipated volume of high cadence electron data from, for example, the Solar Orbiter mission.

We use a novel neural network technique to locate instances of the tearing instability. With these in-situ observations, we investigate the process by which magnetic reconnection

is instigated via the electron tearing mode. These findings will help build a more consistent picture of the reconnection process in magnetospheric substorms, solar flares, and solar wind formation. Moreover, our findings also apply to astrophysical plasma processes, in-situ observations of which are not possible. These include the evolution of accretion disks around black holes, the formation of jets in active galactic nuclei, and gamma ray flares. The electron tearing mode is also an important process in nuclear fusion plasmas, where the instability forms plasmoids and degrades stability of the tokamak, making this area an important field of study.

Acknowledgements

I would firstly like to thank my primary supervisor, Jonny Rae. Since my first summer placement in the MSSL plasma group back in 2016, you have been a great supervisor and friend, and have always been happy to help with whatever issues I faced. It's been a privilege to have you as a supervisor. I know I didn't make your work easy with all the travel escapades I got up to in the last few years. I am also very thankful to my other three supervisors, who have all made my PhD an enjoyably challenging experience. Andrew Walsh - it's been great working with you, especially in Madrid. Your Cluster insight throughout my time has been invaluable. Daniel Verscharen - thank you for always pushing me in the plasma theory side. Your difficult questions during all the panel meetings has definitely showed me to not be complacent. Andy Smith - you've been a constant throughout my PhD and I always enjoy chatting with you. Best of luck for the future in both work and parenthood.

I'm also grateful to have met so many amazing people (PhD students, Post Docs and more) throughout the years working in plasma physics. Georgie Graham - I really enjoyed working with you over those two summers, and you played a big part in me wanting to undertake a PhD in plasma physics at MSSL. Caoimhe Doherty - I doubt I'll meet as good a party host who made sure I always have a Halloween outfit sorted. Thanks for all the great memories. Sam Walton - I'm going to miss having an office mate who I so easily get along with. Catherine Regan - I still forget that you're not in the plasma group. All the best with your future Mars adventures. Christian Lao and Abid Razavi - I hope this message finds you well. I haven't known you guys for long but it's been great having you in our plasma office. It's also been a pleasure to know/work with Colin Forsyth, Chris Owen, Andrew Fazakerley, and Rob Wicks. Clare Watt and Téo Bloch - thanks a lot for all of your input. And lastly

George Nicolaou, Lloyd Woodham, Allan Macneil, Frankie Staples, Jasmine Sandhu, Joel Abraham, Michaela Mooney, Seong-Yeop Jeong, Jeffersson Agudelo, Diego De Pablos, Will Dunn, Richard Haythornthwaite, Choong Ling Liew-Cain, and Angharad Weeks - best of luck for all of your future endeavours.

Many thanks to all of my friends outside of MSSL, as well as Meera Desai, who always takes the utmost interest in whatever I am working on. Thanks finally to my parents and brother, for your ever-lasting support.

I would also like to acknowledge the PEACE Operations Team at MSSL, without which my PhD would not be possible, and the UCL IMPACT and ESA NPI Studentships for all of the financial support.

Contents

1	Introduction	14
1.1	Motivation	14
1.2	Plasmas	14
1.3	Single Particle Motion	16
1.4	Adiabatic Invariants	19
1.5	Plasma Kinetic Theory	21
1.6	Magnetohydrodynamics	23
1.7	Magnetic Reconnection	26
1.8	Plasma Waves	28
1.8.1	Unmagnetised plasma waves	28
1.8.2	Magnetohydrodynamic waves	30
1.8.3	Cold electron plasma waves	31
1.9	Instabilities	32
1.9.1	Linear Instability	32
1.9.2	Growth Rate	33
2	Background	35
2.1	The Solar Wind	35
2.1.1	Solar Wind Electrons	36
2.2	The Earth's Magnetosphere	49
2.2.1	The Dayside Magnetosphere	50
2.2.2	The Magnetotail	51

2.2.3	The Dungey Cycle	52
2.2.4	Substorms	52
3	Instrumentation and Data	54
3.1	The Cluster Mission	54
3.1.1	The PEACE Instrument	54
3.1.2	The FGM Instrument	57
3.1.3	The CIS Instrument	58
4	Techniques	61
4.1	Machine Learning	61
4.1.1	Supervised Learning	61
4.1.2	Unsupervised Learning	61
4.2	Model Testing and Accuracy	62
5	Statistics of solar wind electron breakpoint energies using machine learning techniques	65
5.1	Data	65
5.2	Machine Learning Techniques	66
5.3	Distinguishing Between Suprathermal and Core Electron Populations	69
5.4	Separating Halo and Strahl Electrons	71
5.5	Calculating Relative Number Densities	74
5.6	Statistical Study of Breakpoint Energy versus Solar Wind Speed	76
5.6.1	Confirming Cluster is in Pristine Solar Wind	76
5.6.2	Results	81

5.7	Discussion	87
6	Using dimensionality reduction and clustering techniques to classify space plasma regimes	93
6.1	Machine Learning Models	94
6.1.1	Autoencoders	95
6.1.2	Principal Component Analysis	98
6.1.3	Mean Shift	99
6.1.4	Agglomerative Clustering	101
6.2	Method and Application	101
6.2.1	Data Preparation	102
6.2.2	Reducing Dimensionality	104
6.2.3	Clustering	106
6.3	Evaluation	108
6.4	Conclusion	116
7	Direct evidence of magnetic reconnection onset via the tearing instability	119
7.1	Introduction	119
7.2	Method	121
7.2.1	Data	121
7.2.2	Autoencoder	123
7.3	Coordinate system	124
7.4	Tearing mode stability criteria	125
7.5	Hall quadrupole field	126
7.6	Results	127

7.6.1	Tearing mode stability check	127
7.6.2	Case study	127
7.6.3	Statistical survey of tearing events	136
7.7	Discussion	146
8	Conclusions and Future Work	151

1 Introduction

1.1 Motivation

In this project, we apply machine learning techniques to identify and analyse electron particle distributions in the solar wind at 1 au, across all energies that have unique characteristics, such as distributions that show examples of multiple particle populations. Machine learning algorithms will then enable us to search through the Cluster Science Archive to determine when and why these distributions occur. Linking these occurrences to the ambient solar wind conditions will aid the development of statistical models of particle populations in near-Earth space. This new methodology can then be applied to any appropriate in-situ dataset, for example in different solar wind environments, to gain insight into new plasma regimes.

Machine Learning is still a relatively new concept in the field of space plasma research. However, with the introduction of recently launched Parker Solar Probe and Solar Orbiter, as well as the already existing large datasets from missions such as Cluster, Cassini, MMS (Magnetospheric Multiscale Mission) and Wind, machine learning techniques are becoming the logical tool to use to mine through this data.

1.2 Plasmas

A plasma is coined as the ‘fourth state of matter’. It is an ionised gas consisting of electrons and ions which exhibit collective behaviour and can interact with electromagnetic fields. A plasma has an overall net charge of zero.

Plasmas are good examples of quasi-neutral fluids. Even though the ensemble of parti-

cles have a zero net charge, individual charged particles can create and encounter electric potentials. Interactions between the particles in the plasma results in shielding of these local charge densities, so that the ensemble of particles will appear to be neutral. This phenomenon is quasi-neutrality.

Coulomb potential is defined as the electric potential encountered by a test charge due to a single point charge in a vacuum, and is given by

$$\phi_C = \frac{q}{4\pi\epsilon_0 r} \quad (1.1)$$

where q is the charge, ϵ_0 is the permittivity of free space and r is the distance to the potential source. In the case of a plasma, a sufficient number of charged particles are present. These will move to shield this Coulomb potential, resulting in the test charge experiencing a Debye potential:

$$\phi_C = \frac{q}{4\pi\epsilon_0 r} e^{-\frac{r}{\lambda_D}} \quad (1.2)$$

where λ_D is the Debye length, i.e. the distance at which a Coulomb potential is reduced by a factor of e due to the presence of shielding charged particles. This Debye length is dependent on the number density, n , and temperature of the shielding charged particles. Therefore, assuming a proton-electron plasma ($n = n_i = n_e$), it is given by

$$\lambda_D = \left(\frac{\epsilon_0 k_B T_e}{n q_e^2} \right)^{\frac{1}{2}} \quad (1.3)$$

where q_e is the electron charge, T_e the electron temperature and k_B is Boltzmann's constant. Electron temperature and charge is used as opposed to the ion's because electron exhibit greater mobility. Plasmas can only be described as quasi-neutral when their characteristic length scale is much greater than this Debye length ($L \gg \lambda_D$).

When the quasi-neutrality of a plasma is disturbed, such as when a perturbation is

applied, the electrons will move to correct the imbalance in the charge density. This involves accelerating towards the relatively static ions and oscillating around them due to the electrons' inertia. The frequency of electron oscillation is known as the electron plasma frequency and it characterises the plasma's fundamental mode of oscillation. This frequency is given by

$$\omega_{pe} = \left(\frac{n_e q_e^2}{m_e \epsilon_0} \right)^{\frac{1}{2}} \quad (1.4)$$

where m_e is the electron mass.

1.3 Single Particle Motion

Single particle dynamics is the most simple method for describing a plasma. This involves considering each particle individually and solving its equation of motion. This method only takes into account the effects on a particle's motion from magnetic and electric field, disregarding interactions between particles. The equation of motion of such particle is

$$m \frac{d\mathbf{v}}{dt} = q(\mathbf{E} + \mathbf{v} \times \mathbf{B}) \quad (1.5)$$

where \mathbf{v} is the particle's velocity while \mathbf{B} and \mathbf{E} are the magnetic and electric fields it is exposed to. The right hand side of equation (1.5) represents the Lorentz force.

By assuming that the electric field is zero and the magnetic field is constant, then taking the dot product of equation (1.5) with \mathbf{v} leads to

$$m \frac{d\mathbf{v}}{dt} \cdot \mathbf{v} = \frac{d}{dt} \left(\frac{mv^2}{2} \right) = 0, \quad (1.6)$$

which shows that the particle kinetic energy remains constant under a static magnetic field.

In a uniform magnetic field along the z axis, we obtain the components:

$$\begin{aligned} m\dot{v}_x &= qBv_y \\ m\dot{v}_y &= -qBv_x \\ m\dot{v}_z &= 0. \end{aligned} \tag{1.7}$$

Taking the second derivative, we obtain

$$\begin{aligned} \ddot{v}_x &= -\omega_g^2 v_x \\ \ddot{v}_y &= -\omega_g^2 v_y \end{aligned} \tag{1.8}$$

where ω_g is the gyrofrequency (also known as cyclotron frequency or Larmor frequency) and is defined as

$$\omega_g = \frac{qB}{m} \tag{1.9}$$

The gyroradius (or Larmor radius) of a charged particle around a magnetic field is given by

$$r_g = \frac{v_\perp}{\omega_g} \tag{1.10}$$

where v_\perp is the velocity of the particle perpendicular to the magnetic field direction.

The parallel component of a particle's velocity to the magnetic field, v_\parallel , remains at its initial value throughout its orbital motion. The angle between a particle's total velocity vector, $v_\parallel + v_\perp$, and the magnetic field direction is referred to as the pitch angle, α , and is given by

$$\alpha = \arctan\left(\frac{v_\perp}{v_\parallel}\right) \tag{1.11}$$

A particle with pitch angle 0° or 180° will travel entirely along the magnetic field, whereas a particle with pitch angle 90° only travels perpendicular to the magnetic field. Particles with pitch angles between 0° and 90° travel in a helical motion about its guiding centre (see Figure 1.1).

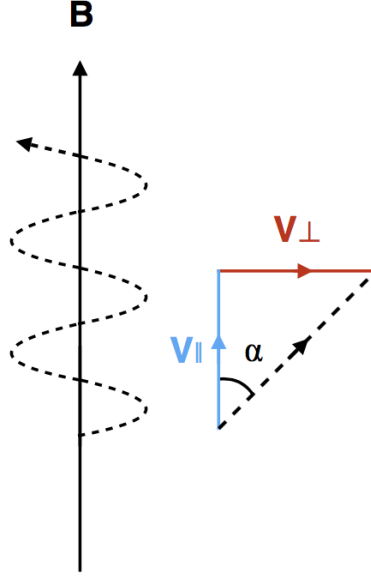


Figure 1.1: The gyromotion of a charged particle, with pitch angle $0^\circ < \alpha < 90^\circ$, in a magnetic field [Graham, 2018].

In geophysical plasmas under the presence of an electrostatic field, most parallel electric fields (to the magnetic field) are not sustained as they are cancelled out by electrons. By considering a constant, uniform, electric field perpendicular to the magnetic field (and therefore parallel to the x axis), we obtain the following components from equation (1.5):

$$\dot{v}_x = \omega_g v_y + \frac{q}{m} E_x \quad (1.12)$$

$$\dot{v}_y = -\omega_g v_x.$$

We then take the second derivative to obtain

$$\begin{aligned} \ddot{v}_x &= -\omega_g^2 v_x \\ \ddot{v}_y &= -\omega_g^2 \left(v_y + \frac{E_x}{B} \right) \end{aligned} \quad (1.13)$$

The electric field's perpendicular component to the magnetic field direction accelerates the charged particle in the plane of its gyromotion. This increases its velocity (and gyroradius)

on one side of the gyration, and decreases its velocity on the other side. This is equivalent to superposing a further velocity component onto the particle's gyromotion in the $-y$ direction.

This drift has the form

$$\mathbf{v}_d = \frac{\mathbf{E} \times \mathbf{B}}{B^2}, \quad (1.14)$$

where \mathbf{v}_d is the drift velocity of a particle's guiding centre. This is also referred to as $\mathbf{E} \times \mathbf{B}$ drift and, since it is independent of the particle's mass and charge, both electrons and ions have the same drift velocity. Figure 1.2 illustrates this $\mathbf{E} \times \mathbf{B}$ drift.

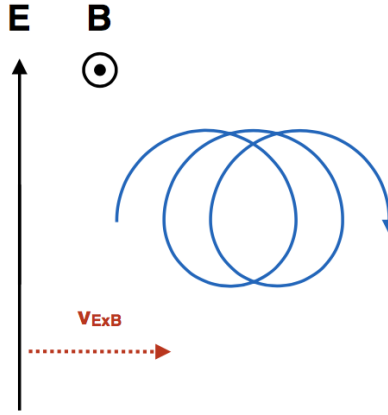


Figure 1.2: The drift motion of an ion, which is exposed to a constant, uniform magnetic and electric field [Graham, 2018].

1.4 Adiabatic Invariants

The characteristic constants of a particle in a field, which in fact change very slowly in comparison to the length and time-scales of the particle's motion, are known as the adiabatic invariants. Each type of particle motion (gyromotion, longitudinal motion and perpendicular drift) has a representative adiabatic invariant. In comparison to a typical particle's time or length scales, such as the gyrofrequency or Larmor radius, adiabatic invariants change over very long periods or distances.

The magnetic moment, μ , is the first invariant and it is associated with particle gyration about a magnetic field.

$$\mu = \frac{mv_{\perp}^2}{2B} = \frac{W_{\perp}}{B} \quad (1.15)$$

Equation (1.15) shows that the magnetic moment is the ratio of the perpendicular energy of a particle to the magnetic field strength. Using equation (1.11), the magnetic moment can also be written in terms of pitch angle:

$$\mu = \frac{mv^2 \sin^2 \alpha}{2B} \quad (1.16)$$

This leads us on to the phenomenon known as magnetic mirroring. Since the magnetic moment is invariant and the total energy remains constant, only the $\sin^2 \alpha$ term changes if the magnetic field strength varies along a gyration trajectory. Therefore, a particle would experience an increase in $\sin \alpha$ as it moves into a converging field and vice versa. When the pitch angle of a particle in a converging field reaches 90° , it loses all parallel velocity and reverses its trajectory (mirroring) due to the gradient force:

$$\mathbf{F}_{\nabla} = -\mu \nabla B \quad (1.17)$$

If a magnetic field is symmetric, in that the field converges on opposite sides (a dipole field), then a particle would bounce between these two mirror points along the magnetic field.

The longitudinal invariant, J , describes the motion of such a particle and is given by

$$J = \oint mv_{\parallel} ds \quad (1.18)$$

where ds is a line element of the guiding centre's path. The second adiabatic invariant states that particles bouncing between mirror points are fixed to a magnetic field line, assuming the time period of the bounce frequency is greater than the rate at which external

changes occur. This can relate to particles bouncing between the Earth's North and South poles. Not all particles, however, will remain trapped, even when the longitudinal invariant is conserved. For particles whose mirror points lie deep enough inside the Earth's atmosphere, they are more likely to collide with neutral particles and will therefore be lost to the atmosphere. This would occur when a particle's equatorial pitch angle is smaller than the width of the loss cone, α_l , at that particular altitude.

In a dipole field, particles also experience drift orbits around the dipole axis. The third adiabatic invariant, Φ , describes the conservation of magnetic flux enclosed within perpendicular drift orbits of particles in a dipole configuration. It is given by

$$\Phi = \oint v_d r d\Psi \quad (1.19)$$

where v_d is the net perpendicular drift velocity and r and $d\Psi$ are the radius and azimuthal element of a circular drift path. The third invariant states that particles remain trapped in drift shells, assuming the changes in geometry are slower than the period of particle motion around a drift shell.

1.5 Plasma Kinetic Theory

The principles of single particle motion are sufficient in describing the dynamics of a small number of particles exposed to an electromagnetic field, however they are not appropriate when characterising a large number of particles. Plasmas, for example, are often considered statistically by defining the distribution function of the particles. This involves describing six quantities: three positions (X, Y, Z) and three velocities (v_X, v_Y, v_Z). Each of these quantities represents a coordinate in six-dimensional phase space and they enable the evolution of a system with time to be studied. Due to the large number of particles in a plasma, the

volume element of phase space ($dX, dY, dZ, dv_X, dv_Y, dv_Z$), also referred to as the particle distribution function, is considered. Taking the first few moments of a distribution function, by integrating over its velocity components, enables relevant macroscopic properties of a plasma to be calculated. The i -th moment of a distribution function, $f(\mathbf{v}, \mathbf{x}, t)$ is defined as

$$M_i(\mathbf{x}, t) = \int f(\mathbf{v}, \mathbf{x}, t) \mathbf{v}^i d^3v \quad (1.20)$$

where \mathbf{v}^i denotes the i -fold dyadic product, a tensor of rank i . The zeroth order moment indicates the number density:

$$n = \int f(\mathbf{v}) d^3v \quad (1.21)$$

and the bulk flow velocity is given by the first order moment:

$$\mathbf{v}_b = \frac{1}{n} \int \mathbf{v} f(\mathbf{v}) d^3v \quad (1.22)$$

This is the average flow velocity of the particle species or component of interest. The contribution of the ensemble particles' velocity fluctuations from the bulk velocity is used to define the pressure tensor, \mathbf{P} . This calculation is based on the second order moment:

$$\mathbf{P} = m \int (\mathbf{v} - \mathbf{v}_b)(\mathbf{v} - \mathbf{v}_b) f(\mathbf{v}) d^3v \quad (1.23)$$

The third order moment, called the heat tensor, also describes deviations from the equilibrium:

$$\mathbf{Q} = m \int (\mathbf{v} - \mathbf{v}_b)(\mathbf{v} - \mathbf{v}_b)(\mathbf{v} - \mathbf{v}_b) f(\mathbf{v}) d^3v \quad (1.24)$$

Its trace vector, \mathbf{q} , is a more useful quantity, and is defined as

$$\mathbf{q} = \frac{m}{2} \int (\mathbf{v} - \mathbf{v}_b) \cdot (\mathbf{v} - \mathbf{v}_b)(\mathbf{v} - \mathbf{v}_b) f(\mathbf{v}) d^3v \quad (1.25)$$

This is known as the heat flux vector and it describes the direction of transport of heat in the plasma, which is not necessarily in the same direction as the mean flow.

1.6 Magnetohydrodynamics

Large systems which have scale sizes much greater than the Larmor radius, r_g , and much longer than the inverse of the Larmor frequency, ω_g^{-1} , can be described by the theory of magnetohydrodynamics (MHD) [Alfvén, 1942]. MHD considers a plasma to be an electrically conducting fluid and only depends on the macroscopic, bulk properties, such as the moments of a particle distribution function. MHD is derived from the combination of both fluid dynamics and Maxwell's equations, and it can be used to describe either one fluid (single-fluid MHD) or one fluid per particle species (multi-fluid MHD). Quasi-neutrality is assumed in all cases.

Assuming no gain or loss interaction processes occur, then a fluid will follow the continuity equation, which states that the particle number density, mass, and charge density are conserved during a fluid's motion:

$$\frac{\partial n_s}{\partial t} + \nabla \cdot (n_s \mathbf{v}_s) = 0, \quad (1.26)$$

where s represents either an ion or electron population. The momentum equation for a fluid is given by

$$n \left[\frac{\partial \mathbf{v}}{\partial t} + (\mathbf{v} \cdot \nabla) \mathbf{v} \right] + \frac{1}{m} \nabla \cdot \mathbf{P} - \frac{q}{m} n (\mathbf{E} + \mathbf{v} \times \mathbf{B}) = 0 \quad (1.27)$$

where \mathbf{P} is the pressure tensor. The equation of state relates the pressure (assumed as isotropic) and density of a given fluid:

$$p \propto n^\gamma \quad (1.28)$$

where γ is the polytropic index and, based on the assumption that a plasma behaves adiabatically and equates to $\frac{5}{3}$.

Defining a plasma with electrons and ions involves subtracting the equation of motion of

electrons from the ions' equations of motion to obtain the generalised Ohm's law:

$$\mathbf{E} + \mathbf{v} \times \mathbf{B} = \eta \mathbf{j} + \frac{1}{nq_e} (\mathbf{j} \times \mathbf{B} - \nabla \cdot \mathbf{P}_e) + \frac{m_e}{nq_e^2} \frac{\partial \mathbf{j}}{\partial t} \quad (1.29)$$

where η is the plasma's resistivity and \mathbf{j} is the current density. For an ideal MHD, $\eta = 0$, so the first term on the right hand side of equation (1.29) can be neglected. The third and fourth terms are also small enough to be neglected, due to restrictions on large length and timescale for an ideal MHD. Assuming that currents perpendicular to the magnetic field are weak in an ideal MHD, resulting in the second term being neglected, leads to

$$\mathbf{E} = -\mathbf{v} \times \mathbf{B} \quad (1.30)$$

which describes an ideal MHD, often referred to as the frozen-in flow approximation, where particles remain frozen to the same magnetic field line.

Retaining the $\eta \mathbf{j}$ term from the right hand side of equation (1.29), by considering a plasma with finite conductivity, and replacing η with $1/\sigma$, the inverse of the conductivity, then equation (1.29) can be rewritten as

$$\mathbf{j} = \sigma(\mathbf{E} + \mathbf{v} \times \mathbf{B}) \quad (1.31)$$

By using Ampère's Law to substitute for \mathbf{j} , followed by applying vector identities and substituting for \mathbf{E} using Faraday's Law, equation (1.31) can then be written as

$$\frac{\partial \mathbf{B}}{\partial t} = \nabla \times (\mathbf{v} \times \mathbf{B}) + \frac{1}{\mu_0 \sigma} \nabla^2 \mathbf{B} \quad (1.32)$$

where μ_0 is the permeability of free space. Equation (1.32) outlines how a magnetic field changes due to its convection with the plasma (first term on the right) and diffusion through the plasma (second term on the right). The ratio between the convection and diffusion term

is referred to as the magnetic Reynolds number, R_m :

$$R_m = \frac{|\nabla \times (\mathbf{v} \times \mathbf{B})|}{|\mu_0^{-1} \sigma^{-1} \nabla^2 \mathbf{B}|} \quad (1.33)$$

Using simple dimensional terms, where $\nabla \rightarrow 1/L$, equation (1.33) can be written as

$$R_m = \mu_0 \sigma L V \quad (1.34)$$

where L is the length scale over which the magnetic field varies and V is the convection velocity of the plasma. Since σ is a measure of the frequency of collisions in a plasma, then for a collisionless plasma ($\eta \rightarrow 0$) in which the magnetic field varies over large length scales, the magnetic Reynolds number is large ($R_m \gg 1$) and convection dominates over diffusion. A large magnetic Reynolds number describes an ideal MHD where the magnetic field is frozen-in to the plasma. For the opposite case in which diffusion dominates over convection ($R_m \ll 1$), the magnetic field will diffuse through the plasma. This implies that field variations over a length scale, L , are destroyed on a diffusion timescale:

$$t_{diff} = \frac{L^2 \mu_0}{\eta} \quad (1.35)$$

Ampère's law in the low frequency limit tells us that

$$\mathbf{j} \times \mathbf{B} = \frac{1}{\mu_0} (\nabla \times \mathbf{B}) \times \mathbf{B} \quad (1.36)$$

which is equivalent to

$$\mathbf{j} \times \mathbf{B} = -\nabla \left(\frac{B^2}{2\mu_0} \right) + \frac{1}{\mu_0} (\mathbf{B} \cdot \nabla) \mathbf{B} \quad (1.37)$$

The first term on the right represents the force resulting from the gradient in magnetic flux density, defined as the magnetic pressure:

$$p_B = \frac{B^2}{2\mu_0}. \quad (1.38)$$

The second term on the right side of equation (1.37) represents the magnetic tension force, which opposes the bending of the field lines in order for them to reach their minimum energy state.

The ratio of plasma pressure (or thermal pressure) to the magnetic pressure is called the plasma beta:

$$\beta = \frac{2p\mu_0}{B^2} \quad (1.39)$$

In a high beta plasma ($\beta > 1$), the thermal pressure dominates and the plasma drags the magnetic field. Whereas in a low beta plasma ($\beta < 1$), magnetic forces dominate and the magnetic field drags the plasma with it.

Restoring forces, a result of magnetic tension, can lead to Alfvén waves propagating through the plasma due to the transverse motion of field lines. In the case of frozen-in magnetic fields, these waves can act to displace the frozen-in particles. The wave's speed is therefore equivalent to the velocity plasma ions can be accelerated to by the magnetic field. This is known as the Alfvén speed:

$$v_A = \frac{B}{(\mu_0\rho)^{1/2}} \quad (1.40)$$

where ρ represents the plasma's mass density.

1.7 Magnetic Reconnection

The magnetic Reynolds number provides an indicator of how accurate the ideal MHD approximation is for a given plasma. When R_m is high and ideal MHD does hold, magnetic field lines from different sources and the particle populations frozen-in to them cannot mix. When the magnetic Reynolds number is around or lower than unity, thin current sheets for example, the frozen-in approximation no longer holds. This is the case in magnetic recon-

nection, which Figure 1.3 illustrates.

Consider two regions of anti-parallel magnetic field lines, separated by a thin current sheet, which are pushed together due to the flow of plasma frozen-in to the fields (Figure 1.3a). The dominant diffusion term means pairs of field lines diffuse through the plasma and reconnect to form highly bent field lines (Figure 1.3b). Magnetic tension will then act to straighten these newly formed lines which results in them being expelled from the reconnection site.

This whole process transfers magnetic energy to particle kinetic energy, as the particles frozen-in to the newly formed bent field lines will accelerate as these field lines straighten.

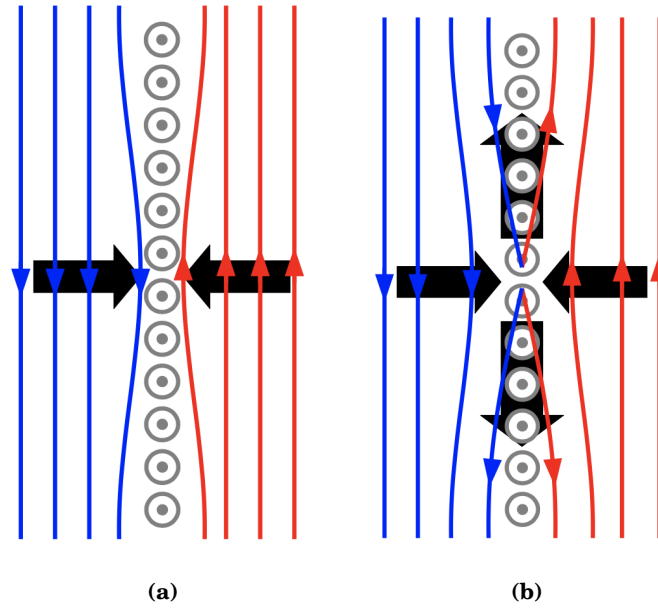


Figure 1.3: Illustration of a basic reconnection geometry. The blue and red lines are magnetic field lines, the grey circles represents a thin current sheet and the black arrows show the direction of the bending of the field lines [Walsh, 2009].

1.8 Plasma Waves

Every plasma in equilibrium experiences a certain amount of fluctuation, according to the plasma temperature, due to the thermal motion of its particles. External factors may also cause distortions of the plasma state. These distortions, or disturbances, can be described as a superposition of linear waves propagating across the plasma in order to transfer the energy of the distortion. The frequencies of these waves generally range from ~ 10000 Hz to ~ 0.01 Hz: very-low frequency (VLF) waves to ultra-low frequency (ULF) waves. The number of wave modes propagating in the plasma are discrete, rather than continuous, and the amplitude of the wave is always higher than the thermal noise level.

A plasma wave disturbance, $\mathbf{A}(\mathbf{x}, t)$, can be represented by plane waves (Fourier components). If the distortion is a plane wave, it comprises of a single Fourier component:

$$\mathbf{A}(\mathbf{x}, t) = \mathbf{A}(\mathbf{k}, \omega) \exp(i\mathbf{k} \cdot \mathbf{x} - i\omega t) \quad (1.41)$$

where \mathbf{A} is the amplitude, \mathbf{k} is the wave vector, and ω is the frequency. The phase and the group velocity of the wave are:

$$\mathbf{v}_{ph} = \omega \mathbf{k} / k^2 \quad (1.42)$$

$$\mathbf{v}_{gr} = \partial \omega / \partial \mathbf{k}. \quad (1.43)$$

The phase velocity is parallel to the wave vector and is the direction of the wave propagation. The group velocity describes the speed and direction of the wave's energy flow.

1.8.1 Unmagnetised plasma waves

There exist two types of waves in an unmagnetised plasma: internal plasma oscillations, and electromagnetic waves. Langmuir oscillations are an example of the first type unmag-

netised plasma waves. These oscillations occur under the condition that the ions are stationary relative to the electrons' movement. This is akin to high-frequency electron oscillations. The wave's linear oscillator equation, which describes the variation of the density, is

$$\frac{\partial^2 \delta n}{\partial t^2} + \frac{n_e e^2}{m_e \epsilon_0} \delta n = 0. \quad (1.44)$$

The angular frequency of the electrons about the ions is

$$\omega_{pe}^2 = \frac{n_e e^2}{m_e \epsilon_0}. \quad (1.45)$$

As the electrons have different initial velocities, they will react differently under an external attempt to displace them. We therefore introduce the adiabatic variation of the electron thermal pressure, $\delta p_e = \gamma_e k_B T_e \delta n_e$, into the electron momentum equation. Assuming that the electron temperature is constant, the displaced electron fluid's linearised equation of motion takes the form

$$\frac{\partial \delta v_{e,x}}{\partial t} = -\frac{e}{m_e} \delta E - \frac{\gamma_e k_B T_e}{m_e n_e} \frac{\partial \delta n}{\partial x}. \quad (1.46)$$

We then arrive at a more accurate equation for the variation in density

$$\frac{\partial^2 \delta n}{\partial t^2} - \frac{\gamma_e k_B T_e}{m_e} \frac{\partial^2 \delta n}{\partial x^2} + \omega_{pe}^2 \delta n = 0. \quad (1.47)$$

Solving this equation yields the relation between the angular frequency and wavenumber of the Langmuir wave, also known as the Langmuir dispersion relation:

$$\omega_l^2 = \omega_{pe}^2 + k^2 \gamma_e v_{th}^2, \quad (1.48)$$

where $v_{th} = (k_B T_e / m_e)^{1/2}$, i.e. the electron thermal velocity.

Moving charges, which are a result of electrostatic disturbances, can lead to oscillating plasma currents that become sources of electromagnetic waves. In an unmagnetised plasma,

the most common of such is the free-space electromagnetic wave. The dispersion relation of this wave in a plasma is

$$\omega_{om}^2 = \omega_{pe}^2 + c^2 k^2, \quad (1.49)$$

where ω_{om}^2 is the frequency of the ordinary mode wave, with its nomenclature deriving from having the same dispersion as a free-space wave in the absence of a plasma. The difference between an ordinary mode and a free-space wave is there is no real solution for the wavenumber for frequencies below the electron plasma frequency, with the wave ceasing to exist. The plasma frequency is therefore the cut-off of the ordinary mode. At this point, the direction of the propagation of the wave reverses.

1.8.2 Magnetohydrodynamic waves

At large scales, ideal MHD conditions can be used to describe waves. One particular wave supported by magnetised plasmas are Alfvén waves, a type of transverse wave. These waves propagate through a plasma via the transverse motion of field lines, which is caused by magnetic tension. The solution of the MHD wave equation, for a right-handed system where the wave vector's perpendicular component is parallel to the x axis, and the magnetic field is aligned to the z axis, can be written in the general form

$$\begin{bmatrix} \omega^2 - v_A^2 k_{\parallel}^2 - c_{ms}^2 k_{\perp}^2 & 0 & -c_s^2 k_{\parallel} k_{\perp} \\ 0 & \omega^2 - v_A^2 k_{\parallel}^2 & 0 \\ -c_s^2 k_{\parallel} k_{\perp} & 0 & \omega^2 - c_s^2 k_{\parallel}^2 \end{bmatrix} \begin{bmatrix} \delta v_{0x} \\ \delta v_{0y} \\ \delta v_{0z} \end{bmatrix} = 0 \quad (1.50)$$

where v_A is the Alfvén velocity and c_{ms} is the magnetosonic speed:

$$c_{ms}^2 = c_s^2 + v_A^2, \quad (1.51)$$

where $c_s = \gamma k_B T / m_i$ is the sound velocity.

Equation (1.50) shows that the velocity fluctuation in the y -direction decouples from the other fields, resulting in a wave with a linear dispersion relation:

$$\omega_A = \pm k_{\parallel} v_A. \quad (1.52)$$

This purely transverse electromagnetic wave is called the shear Alfvén wave, and propagates parallel to the ambient field.

The remaining four matrix elements in equation (1.50) couple the parallel velocity component to the transverse fluctuation in the x direction. The two roots are

$$\omega_{ms}^2 = \frac{k^2}{2} \left(c_{ms}^2 \pm \left[(v_A^2 - c_s^2)^2 + 4v_A^2 c_s^2 \frac{k_{\perp}^2}{k^2} \right]^{1/2} \right). \quad (1.53)$$

The expression in the curly brackets represent the phase velocities of two magnetosonic wave modes. The root with the positive sign represents the fast magnetosonic wave, and the root with the negative sign represents the slow magnetosonic wave. The fast mode propagates into the perpendicular direction, while the slow mode does not propagate. Therefore the only perpendicular MHD wave is the fast magnetosonic wave, as the shear Alfvén wave does not propagate into the perpendicular direction.

1.8.3 Cold electron plasma waves

Near to the ion-cyclotron and plasma frequencies, the differences between electron and ion dynamics become more important and a one-fluid MHD theory is no longer valid. As the electron and ion inertia are now to be taken into account, we consider a cold magnetised electron plasma where the ions are represented as a neutralising background. These waves therefore have much higher frequencies than all ion frequencies.

Cold electron dynamics is dominated by the motion of single-particle electrons in a strong magnetic field. The magnetic field of any wave in this environment is not affected by the mo-

tion of electrons. Electron whistler waves are a type of such wave which occur at sufficiently low frequencies. Their dispersion relation is

$$\omega_W = k^2 c^2 \omega_{ge} \omega_{pe}^{-2}, \quad (1.54)$$

where ω_{ge} is derived from the electron gyrofrequency vector:

$$\omega_{ge} = e\mathbf{B}_0/m_e. \quad (1.55)$$

These waves are frequently observed in the Earth's magnetosphere and on the ground. They can often be excited by lightning. They propagate along magnetic field lines from one hemisphere to the other, and their phase and group velocities are proportional to k , and to $\omega_W^{1/2}$. The high-frequency part of a whistler wave originating from the southern hemisphere will thereby reach the northern hemisphere before the low-frequency part.

1.9 Instabilities

Energy accumulated in a non-equilibrium system can be redistributed via the generation of an instability. There are three different non-equilibrium states that lead to instabilities: linearly unstable, metastable, and non-linearly unstable. For linearly unstable states, a linear instability occurs with the slightest linear distortion of the system. In a metastable state, the system remains stable under a linear distortion only for a certain period of time. In a non-linearly unstable state, a system is stable against small amplitude disturbances, whereas larger disturbances causes it to become unstable.

1.9.1 Linear Instability

In linear wave theory, waves are considered small disturbances if their amplitude is much smaller than the stationary state vector. For a disturbance δn of the density n , then

$\delta n(\mathbf{x}, t) \ll n(\mathbf{x}, t)$. However variations in n are much slower than variations in δn . The wave function as a result of the disturbance is represented by a superposition of plane waves which oscillate at a frequency ω , where ω is the solution of the linear dispersion relation. The Fourier decomposition of a wave field vector is

$$\delta A = \sum_{\mathbf{k}} A_{\mathbf{k}} e^{i\mathbf{k} \cdot \mathbf{x} - i\omega t}. \quad (1.56)$$

For real values of ω , the disturbances are oscillating waves. For complex solutions, the wave amplitude depends on the sign of the imaginary part of the frequency $\gamma(\omega_r, \mathbf{k})$. For negative γ values, the real part of the amplitude exponentially decreases with time and the wave is damped. For positive values, the wave amplitude grows exponentially and a linear instability is reached. In this case, γ is referred to as the growth rate. A linear instability relies on free energy sources in the plasma to energise the growing wave.

1.9.2 Growth Rate

The amplitude of an unstable wave is

$$A_{\mathbf{k}}(t) = A_{\mathbf{k}} e^{\gamma(\omega_r, \mathbf{k})t}. \quad (1.57)$$

This approximation breaks down when the amplitude is similar to the background amplitude of the field A_0 , at the time:

$$t_{nl} = \gamma^{-1} \ln\left(\frac{A_0}{A_{\mathbf{k}}}\right). \quad (1.58)$$

When the approximation is violated, non-linear processes occur which also involve the interaction of waves with each other. The larger the growth rate, the earlier t_{nl} is reached. For growth rates larger than the wave frequency, the wave amplitude will explode and not a single oscillation is performed during one period. Therefore the condition for instabilities

which remain linear over many wave periods is

$$\gamma/\omega \ll 1. \tag{1.59}$$

This condition is the case for weak instabilities. Strong instabilities are referred to as non-oscillating instabilities and will only occur in the lowest frequency range of a MHD plasma model.

2 Background

2.1 The Solar Wind

The solar wind is a highly-conducting plasma, constantly flowing out from the Sun as a result of supersonic expansion of the solar corona. Due to its high conductivity, the solar magnetic field is frozen-in to the plasma and is therefore carried out by the solar wind. The start points of this interplanetary magnetic field (IMF) are considered to be fixed to the Sun's photosphere and therefore rotate as the Sun's surface rotates. This rotation leads to the IMF forming a large Archimedean spiral (Figure 2.3), known as the Parker spiral [Parker, 1963].

It is generally assumed that there are two categories of solar wind: fast wind and slow wind [Feldman *et al.*, 2005]. Fast winds have velocities greater than 600 km/s and slow winds exhibit velocities generally less than 500 km/s. Studies show that fast winds are created in the interior of coronal holes [Zirker, 1977], which are regions of open magnetic field lines, and flows outwards to fill the heliosphere (a magnetic field and plasma bubble which originates from the Sun and encompasses the solar system). Slow wind has been found to emanate from the streamer belt, or closed-field region of the Sun [McComas *et al.*, 1998], however its precise origin is still up for discussion [Feldman *et al.*, 2005].

Three models have been proposed to describe the formation of slow solar wind. The 'expansion factor model' [Wang *et al.*, 1997] postulates that slow plasma is generated at the edge of a coronal hole near a streamer belt (bright loop-like structures over active regions on the Sun). At this edge, near the boundary of a streamer belt, slow winds are heated and accelerated on open flux tubes. This is because flux tubes near streamer belt boundaries are

assumed to expand a lot quicker than flux tubes in the inner regions of coronal holes [Kepko *et al.*, 2016].

The second model is known as the ‘interchange model’ [Edmondson, 2012], which credits the formation of slow wind to the interchange reconnection of open magnetic fields with closed streamer belt fields. Continuous interchange reconnection between these two regions theoretically results in open flux diffusing throughout streamer belt fields, releasing closed field plasma to the open field lines of the heliosphere [Kepko *et al.*, 2016]. The third model, referred to as the ‘S-Web model’, postulates that closed streamer belt field plasma is released due to a similar process as the interchange model. However this only occurs on the edge of coronal holes, at the boundary between open and closed magnetic flux [Antiochos *et al.*, 2011].

2.1.1 Solar Wind Electrons

Solar wind electron velocity distributions at 1 au consist of three main populations: the thermal (<50 eV) population called the core and two suprathermal (~60–1000 eV) populations called halo and strahl [Maksimovic *et al.*, 2005; Feldman *et al.*, 1975]. The core has a temperature at 1 au of $\sim 10^5$ K [Balogh and Smith, 2001] and exhibits a characteristic bi-Maxwellian velocity distribution. At 1 au, it makes up ~95%-96% of the total solar wind electron density in slow wind [McComas *et al.*, 1992; Maksimovic *et al.*, 2005; Štverák *et al.*, 2009] and ~90% in fast wind [Štverák *et al.*, 2009]. The halo, on the other hand, exhibits a kappa distribution and forms the tails of the total electron velocity distribution (see Figure 2.1). Halo electrons exist at a higher temperature ($\sim 100^5$ K) than core electrons [Feldman *et al.*, 1975]. The core and halo are quasi-isotropic populations, whereas the strahl travels along the interplanetary magnetic field (IMF) and can be observed in either the parallel or

anti-parallel magnetic field direction [Feldman *et al.*, 1978], or in both directions [Gosling *et al.*, 1987]. There are also cases where a strahl population does not exist [Anderson *et al.*, 2012], particularly in slow solar wind [Gurgiolo and Goldstein, 2017].

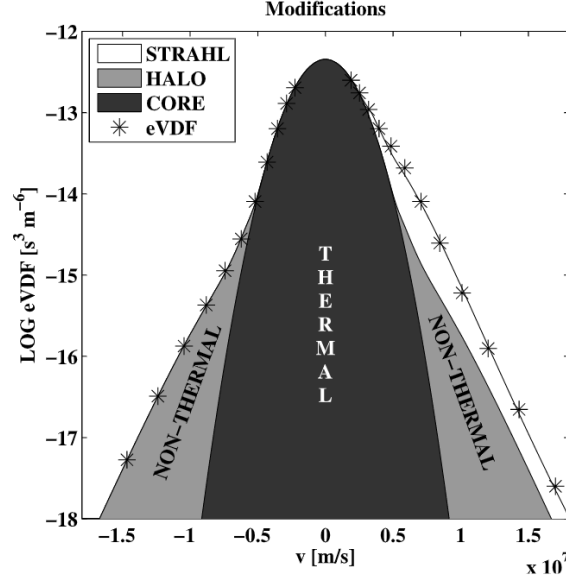


Figure 2.1: Two-dimensional velocity distribution function separated into its thermal (core) and non-thermal (strahl and halo) parts, obtained from Helios 1 and 2, Cluster II and Ulysses observations [Štverák *et al.*, 2009].

The thermal core originates from the corona, as a result of Coulomb collisions and wave-particle interactions [Pierrard *et al.*, 2001; Vocks *et al.*, 2008]. Suprathermal solar wind electrons are also generally considered to form in the solar corona [Vinas *et al.*, 2000; Che and Goldstein, 2014] due to Coulomb collisions and/or wave-particle interactions, and then evolve into the characteristic strahl and halo populations via various mechanisms as they travel anti-sunward. The strong field-aligned nature of strahl occurs due to adiabatic focusing effects [Owens and Forsyth, 2013], which are particularly prevalent closer to the Sun due to more radial field lines experiencing larger changes in magnetic field strength per

radial distance. As the strahl travels outwards, it undergoes scattering via wave-particle interactions in the solar wind, which forms the halo population [*Saito and Gary, 2007; Pagel et al., 2007*].

Part of the halo population can also originate from the solar corona before the suprathermal electrons experience adiabatic focusing. Work by *Che and Goldstein [2014]* suggests this is due to solar nanoflares, from the inner corona, which energises electrons and subsequently triggers instabilities. These instabilities would then create kinetic Alfvén and whistler mode wave turbulence, which combined with scattering produces a halo.

The velocity filtration model can be used to explain the evolution of suprathermal electrons into their characteristic velocity distribution functions. This model describes how a suprathermal electron population, originating in the low corona, experiences velocity filtration via gravitational and electrostatic fields [*Scudder, 1992*]. As a result, the suprathermal electrons exhibit higher temperatures as they move into higher altitudes, and form the halo and strahl, as measured in the solar wind.

At 1 au, it is expected that solar wind electron should not undergo any significant Coulomb collisions [*Vocks et al., 2005*]. This implies that adiabatic focusing should be the dominant mechanism experienced by these electrons. Adiabatic focusing describes how an electron moving into a region of weaker magnetic field strength will experience a decrease in pitch angle, and vice versa. When no scattering effects are taking place, an electron's pitch angle evolution with heliocentric distance is dependent on the conservation of magnetic moment [*Owens et al., 2008*]:

$$\sin^2 \alpha(R) = \frac{B_{TOT}(R) \sin^2 \alpha(R_0)}{B_{TOT}(R_0)} \quad (2.1)$$

where $B_{TOT}(R)$ is the magnetic field strength at heliocentric distance R and R_0 is a ref-

erence heliocentric distance. Due to magnetic flux conservation, the heliospheric magnetic field's radial component is proportional to $1/R^2$ [Owens *et al.*, 2008], which combined with equation (2.1) culminates in $\sin^2 \alpha$ decreasing when R increases.

This process of adiabatic focusing leads to the assumption that the strahl narrows with heliocentric distance into a collimated beam of width $< 1^\circ$ [Anderson *et al.*, 2012]. However, strahl beams have been found to have pitch angles of greater than 20° at 1 au [Anderson *et al.*, 2012], implying there exists other wave-particle scattering processes further out from the Sun. Using Ulysses data, Hammond *et al.* [1996] showed that the average strahl pitch angle width continued increasing with heliocentric distance past 1 au (Figure 2.2), further supporting this implication. Graham *et al.* [2017], using data from Cassini, also found evidence of this strahl broadening, at various energies, up to 5.5 au (Figure 2.5).

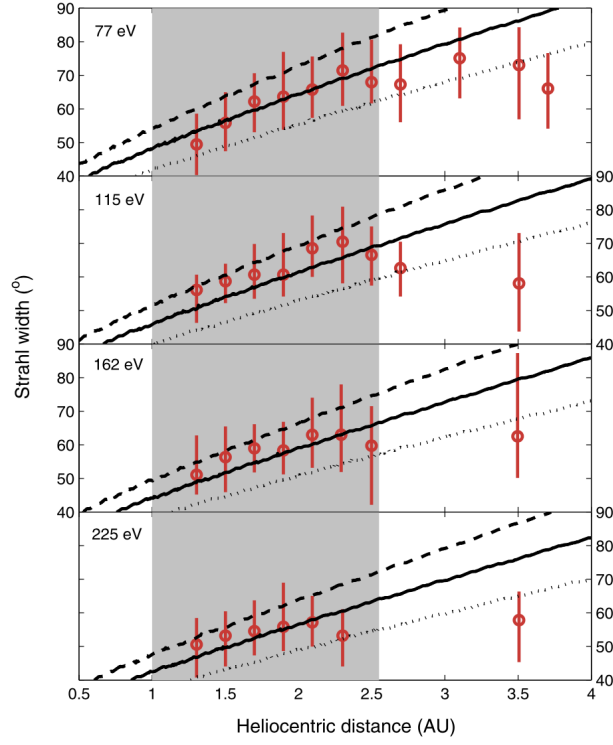


Figure 2.2: Strahl width medians plotted against heliocentric distance. The red circles represent data obtained from Ulysses observations. The error bars depict the upper and lower quartiles of the distribution within each 0.2 au radial distance bin. The gray region shows the range of radial distances at which the observed strahl width increases linearly. The solid black lines plot the results of numerical simulations of electron evolution with radial distance [Owens *et al.*, 2008]. The scattering rate at each energy has been set to a factor which matches 77 eV Ulysses observations. The black dashed lines represent model results for higher and lower scattering rates.

One model [Owens *et al.*, 2008], which assumes a constant pitch angle scattering rate with time, distance and electron kinetic energy, can be used to explain the strahl width [Hammond *et al.*, 1996] increase up to 2.5 au (see Figure 2.2). At greater heliocentric distances, the Parker spiral interplanetary magnetic field becomes more unwound (less radial) so electrons at this radial distance will experience a diminished adiabatic focusing effect,

due to a smaller gradient in the decrease of magnetic field strength (Figure 2.3). This results in the constant scattering rate having a greater influence. Adiabatic focusing should also decrease with helio-latitude due to the same Parker spiral effect [Owens *et al.*, 2008].

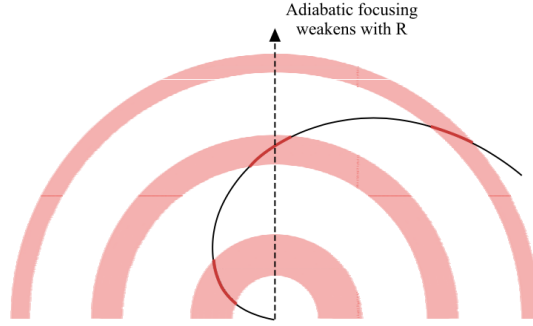


Figure 2.3: The Parker spiral superimposed with red regions, which represent the radial distance an electron moves for a fixed period of time as it moves out from the Sun [Owens *et al.*, 2008].

Characterising the dependence of strahl width on electron energy would help determine the role different scattering mechanisms play as the strahl travels along interplanetary magnetic field lines. Studies of the strahl energy relation at 1 au have produced differing results, indicating that various wave-particle scattering mechanisms are in operation. Multiple studies show that strahl pitch angle widths have decreased with larger electron energies [Feldman *et al.*, 1978; Fitzenreiter *et al.*, 1998]. However, when there are enhanced magnetic field fluctuations in the solar wind, observations have found that strahl width can increase with electron energy [Pagel *et al.*, 2007]. Other extensive studies conclude that strahl widths can increase or decrease with increasing electron energies, with equal probabilities [Anderson *et al.*, 2012]. One study, which observed that strahl pitch angles decrease with larger electron energies, found that the type of solar wind (fast or slow) has no effect on the strahl width energy relation [Fitzenreiter *et al.*, 1998].

Using both Ulysses and Cassini data, investigations into the relationship between the rate of strahl width increase (with distance) and electron energy have also been carried out. *Hammond et al.* [1996] showed that low energy strahl electrons exhibit greater broadening per au than higher energy electrons. Measurements from Cassini, on the other hand, showed that there is a slight increase in the strahl pitch angle scattering rate with increasing energy [*Graham et al.*, 2017]. Using a modelled scattering rate, which was constant with time, distance and electron energy, *Owens et al.* [2008] realised a negative correlation between strahl broadening per au and energy. However, the calculated gradient of decrease was much smaller than the Ulysses results [*Hammond et al.*, 1996]. Figure 2.4 illustrates these three trends.

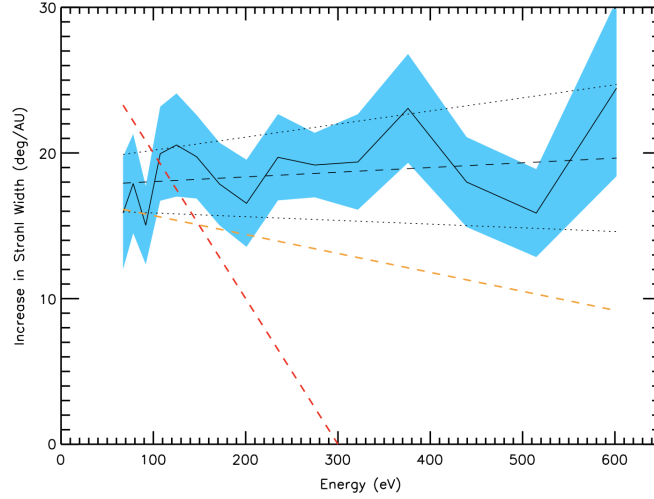


Figure 2.4: The relationship between strahl broadening per au and electron energy. The solid black line shows the results from the Cassini study, plotted using linear fits to the strahl pitch angle against heliocentric distance distributions [Graham *et al.*, 2017]. The shaded blue area represents a one standard deviation error on either side. The black dashed line depicts the linear fit to the Cassini with 1σ error on either side (black dotted lines). The red dashed line and orange dashed line were obtained by the extrapolating Ulysses results [Hammond *et al.*, 1996] and the empirical model results [Owens *et al.*, 2008] respectively [Graham *et al.*, 2017].

Time-of-flight effects can be used to explain the empirical model’s simulations of a gradual decrease in strahl broadening per au with energy. Electrons with larger kinetic energies, and therefore larger velocities, travel further along the field lines per second, and so would experience a larger decrease in magnetic field strength per second. This leads to higher energy electrons undergoing greater adiabatic focusing. The difference between the model’s results and in-situ observations further suggests that other scattering mechanisms are at play.

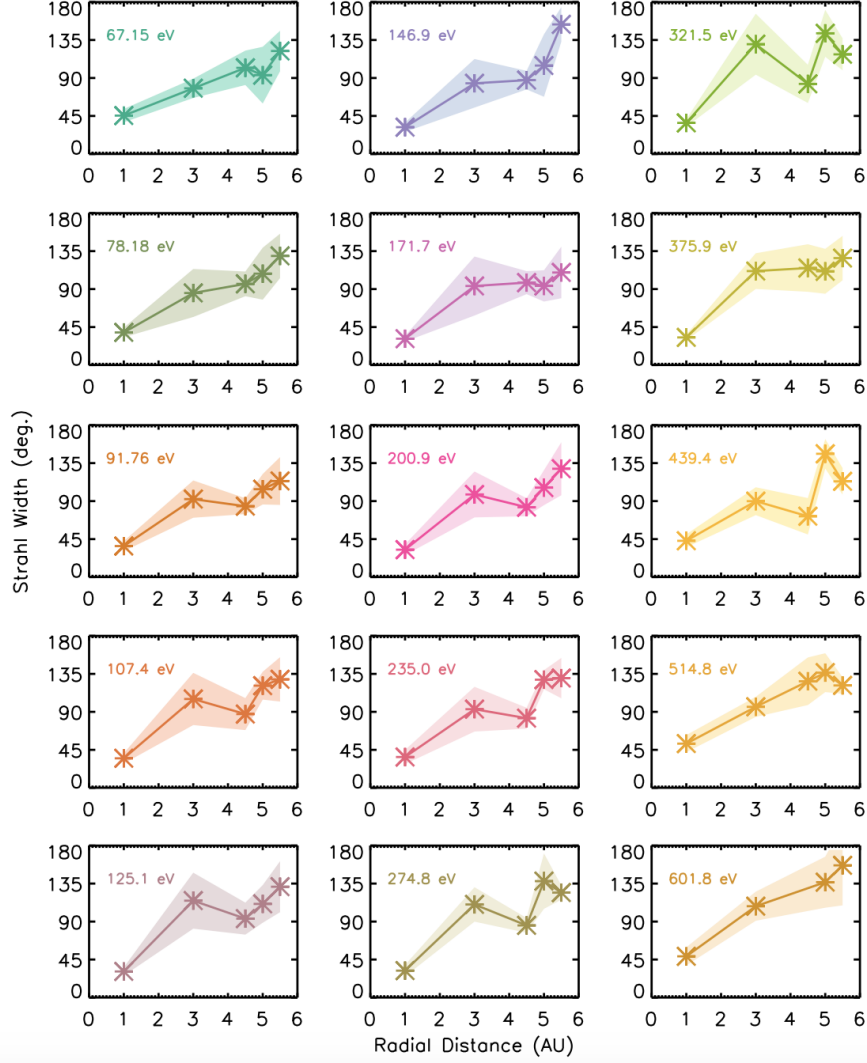


Figure 2.5: Median strahl width as a function of radial distance for CAPS-ELS energy bins. The coloured regions represent the median absolute standard deviation [Graham *et al.*, 2017].

Strahl scattering has also lead to a decrease in the relative density of strahl (compared to the total non-thermal electron density) as the heliocentric distance increases. Concurrently, the relative halo density increases with heliocentric distance, indicating that these wave-particle scattering mechanisms cause the strahl to broaden and eventually scatter into the isotropic halo. This trend is shown in Figure 2.6 for both fast and slow wind [Štverák *et al.*,

2009]. Extrapolating the relative halo density from the lowest radial distance bin, 0.3 au, towards the Sun shows that the contribution of halo electrons to the total electron density is minimal before strahl scattering takes place.

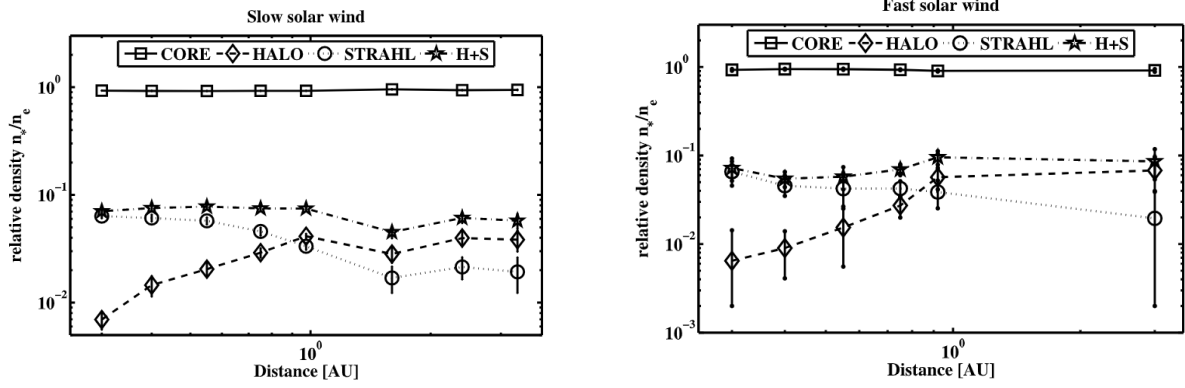


Figure 2.6: Radial evolution of the relative densities of each component of the electron velocity distribution function for both slow (left) and fast (right) wind [Štverák *et al.*, 2009].

Assuming the solar wind undergoes an isotropic steady state expansion, the core's density should be proportional to r^{-2} . This theoretical profile is indicated by the dots (labelled as radial expansion) in Figure 2.7. There is a clear agreement between the core's measured density evolution and this profile, with the core's density varying as $r^{-2.03 \pm 0.08}$ for slow wind and $r^{-2.11 \pm 0.17}$ for fast wind.

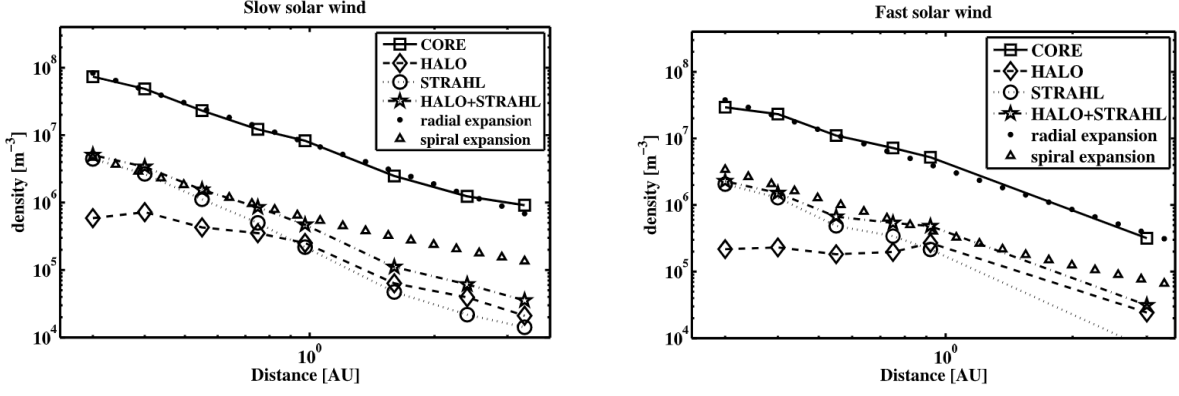


Figure 2.7: Radial evolution of the absolute density of both slow (left) and fast (right) solar wind [Štverák *et al.*, 2009].

As discussed previously, the evolution of non-thermal electron densities is more complex, due to a combination of adiabatic focusing effects and wave-particle interactions. Unlike the core, the strahl expands along the magnetic field, which is approximately radial at short distances but then follows a spiral configuration. Therefore, a property (such as density or heat flux) of a non-thermal population expanding along such a magnetic field in a spiral configuration is proportional to equation (2.2) [Scime *et al.*, 1994].

$$\propto \frac{1}{r^2} \sqrt{1 + \left(\frac{r\omega}{v_{sw}}\right)^2} \quad (2.2)$$

Where r is the radial distance from the sun, ω is the sun's angular speed of rotation and v_{sw} is the solar wind speed. This theoretical profile is represented by the triangles (labelled as spiral expansion) in Figure 2.7, and have been plotted using a slow solar wind speed, v_{sw} of 400 m/s and fast solar wind speed of 650 m/s. Previously stated interaction mechanisms are responsible for the divergence, at greater radial distances, between the measured strahl density evolution and this profile.

The temperature of electrons within the solar wind also evolves with radial distance.

For core electrons only undergoing adiabatic expansion, the temperature should decrease with $r^{-4/3}$. While electrons undergoing Coulomb collisions should have their temperature decrease proportional to $r^{-1/3}$ [Scudder and Olbert, 1979]. In practice, observations using in-situ measurements of bulk electron temperatures at various radial distances shows this decrease varies between a profile of $r^{-0.24}$ and $r^{-1.26}$ [Balogh and Smith, 2001]. Ulysses data also show that the energy of halo distributions decreases with heliocentric distance.

Multiple studies have been undertaken in order to identify the breakpoint energy i.e. the energy at which non-thermal tails start to deviate from the Maxwellian core. Coulomb collisions are thought to be the main driving force behind the breakpoint energy. Particles above a certain energy experience minimal interactions/collisions, creating the non-thermal tails in the electron velocity distribution function [Scudder and Olbert, 1979] and forming halo and strahl. Based on the properties of Coulomb collisions and the inhomogeneity of the solar wind, and assuming minimal wave-particle interactions in the heliosphere, this breakpoint energy relates to heliocentric radial distance as [Scudder and Olbert, 1979]:

$$E_{bp}(r) = 7k_B T_{core}(r) \quad (2.3)$$

At 1 au, the average breakpoint energy is considered to be 60 eV [Feldman et al., 1975], however this varies with the local core temperature and solar wind speed [Štverák et al., 2009]. The breakpoint energy also differs depending on whether it is between the core and halo or the core and strahl, as Figure 2.8 shows.

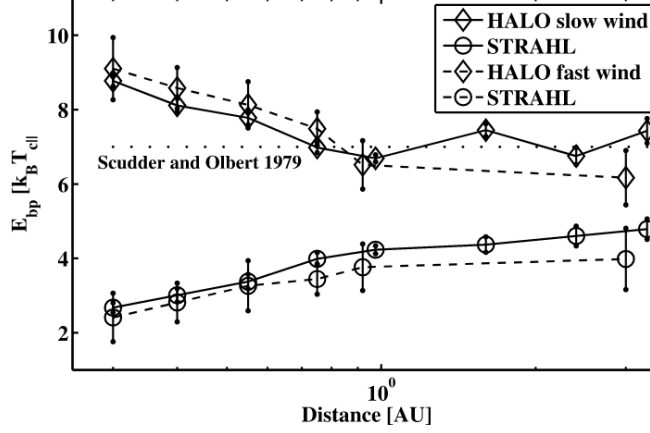


Figure 2.8: Electron velocity distribution function analysis, using Ulysses data, of breakpoint energy against radial distance for both halo and strahl [Štverák *et al.*, 2009].

Empirical studies, using core and halo parameters derived from 3D electron distribution data collected by Ulysses' electron spectrometer, have also characterised the relation between breakpoint energy and radial distance [McComas *et al.*, 1992]. This research has found that the breakpoint energy decrease with distance is proportional to $r^{-0.4}$, and ranges between 47 eV and 60 eV at 1 au.

Studies show that heat flux is aligned with magnetic field direction [Feldman *et al.*, 1975; Scime *et al.*, 1994]. The strahl is predominantly responsible for transporting the majority of solar wind heat flux (equation 1.25). However if the strahl is not present, the drift of halo electrons relative to the core carries the majority of the heat flux [Bale *et al.*, 2013]. Observations, using Helios spacecraft, at a range of radial distances (0.3-1 au) show that current kinetic models overestimate the magnitude of solar wind heat flux, meaning it cannot be accurately described by Coulomb collisions alone [Pilipp *et al.*, 1990]. Characterising the radial evolution of solar wind heat flux up to ~5 au with Ulysses showed the heat flux is proportional to $r^{-2.9}$ [Pilipp *et al.*, 1990]. The measured magnitudes at these distances

are also lower than predicted by models. The mechanism known as the heat flux instability [Gary *et al.*, 1994], which predicts a similar heat flux proportion of r^{-3} , can potentially limit the heat flux, therefore explaining this discrepancy.

2.2 The Earth's Magnetosphere

The Earth's magnetosphere is the environment around Earth that is dominated by Earth's own magnetic field. The magnetosphere acts to exclude any external magnetic fields and particles. The collision of the solar wind against the magnetosphere causes a compression of its dayside, and an elongation of its nightside, which is also known as the magnetotail. This is shown in Fig. 2.9, which also highlights the different regions of the dayside and nightside magnetosphere.

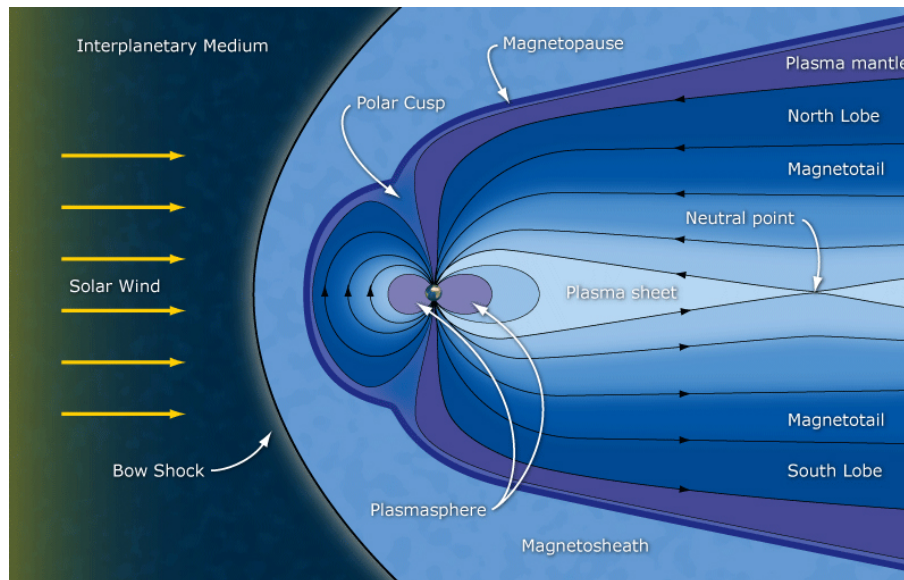


Figure 2.9: A 2D schematic of the Earth's magnetosphere, taken perpendicular to the Earth-Sun line [Russel, 2011].

2.2.1 The Dayside Magnetosphere

Due to the frozen-in approximation, particles associated with magnetic fields of different sources do not mix. This therefore means that the magnetosphere acts as an obstacle for solar wind particles, causing them to rapidly slow down and be heated by shock waves caused by the collision. This occurs at the edge of the magnetosphere, which is known as the bow shock. The bow shock is approximately $14 R_E$ away from the Earth [Hughes, 1995]. The magnetosheath is the next region of the magnetosphere that is downstream of the bow shock. It comprises of a subsonic flow of plasma, that is denser and hotter than the pre-collision solar wind, due to the conservation of mass-flux around the bow shock, and the conversion of kinetic energy to thermal energy due to the collision. The boundary between the IMF and the Earth's magnetic field creates a gradient in magnetic field. According to Ampere's Law, this gradient induces a current, which in the case of the Earth's magnetosphere results in a thin current sheet the magnetopause. The magnetopause is approximately $10 R_E$ away from the Earth, with this distance depending on the balance between magnetospheric and solar wind pressures.

The cusps, located above each of the Earth's poles, are the point of entry for solar wind plasma into the inner magnetosphere. The plasmasphere is a region of the inner magnetosphere, and has a density of $\sim 10^3 \text{ cm}^{-3}$, making it the densest region in the magnetosphere. It is located roughly $4 R_E$ away from the Earth, and consists of cold ionospheric plasma that co-rotates with Earth in a toroidal shape. Closer to the Earth are the inner and outer Van Allen radiation belts. These belts contain highly energetic particles, and are located between $\sim 0.1 R_E$ and $\sim 6 R_E$.

2.2.2 The Magnetotail

The interaction between the Earth’s magnetosphere and the solar wind causes the stretching of the magnetotail up to a distance of $\sim 600 R_E$ from the Earth. The magnetotail is traditionally divided into three different regions: the plasma sheet (PS), the plasma sheet boundary layer (PSBL), and the lobes [Hughes, 1995]. These regions are defined by their plasma and magnetic field characteristics. The low temperature (~ 85 eV) outermost northern and southern lobes are on open magnetic field lines which results in a much lower plasma density of $\sim 0.01 \text{ cm}^{-3}$ [Lui, 1987]. The plasma sheet boundary layer exists on the reconnected magnetic field lines. This region forms the transition region in between the plasma sheet and the lobes, and is characterised by a population of field-aligned particles and a plasma β , which is the ratio of the plasma pressure to the magnetic pressure, of ~ 0.1 [Lui, 1987].

The innermost plasma sheet typically contains a comparatively hot (~ 4250 eV) and isotropic plasma with a relatively high particle density of $\sim 0.01 \text{ cm}^{-3}$. At the centre of the plasma sheet is the thin neutral current sheet, which is characterised by a relatively high plasma β of ~ 10 , and a magnetic field strength of near zero [Lui, 1987]. Although isotropic electron pitch angle distributions (PADs) are the most dominant in the plasma sheet, many cases of pitch angle anisotropy have also been found [e.g. Walsh *et al.*, 2013; Artemyev *et al.*, 2014; Liu *et al.*, 2020]. These intervals correspond to a colder and denser electron population and are linked to: cold anisotropic ionospheric outflows [Walsh *et al.*, 2013], and a penetration of cold electrons from the magnetosheath near the flanks [Artemyev *et al.*, 2014].

2.2.3 The Dungey Cycle

So far we have been describing the magnetosphere using the closed magnetosphere model. However, when considering magnetic reconnection, whereby ideal MHD breaks down, the frozen-in approximation is no longer valid, allowing plasmas of different sources to mix. In our case, this process connects the magnetosphere to the IMF via reconnection in the magnetopause and magnetotail current sheet. We therefore use the open magnetosphere model, as well as the Dungey cycle [Dungey, 1961] to describe this interaction.

When the IMF is pointed Southward, i.e. in the opposite direction to the Earth's magnetic field, reconnection can take place in the dayside magnetosphere. Subsequently, two new field lines, each connecting the IMF to the Earth's poles, are created. They are therefore open to the solar wind. The magnetic tension force causes these lines to straighten, and they are subsequently dragged tailward by the solar wind. As more magnetic flux is added to the nightside magnetosphere, the magnetotail is stretched further from the Earth, and a reconnection site is formed at the neutral line. The result of this magnetotail reconnection is a closed field line connected to the Earth, and an IMF field line pushed out by the solar wind. The new closed field line convects back to the dayside due to magnetic tension, and undergoes the same process again.

2.2.4 Substorms

In the nightside magnetosphere, reconnection is usually part of a larger series of events called a substorm [Mcpheeron *et al.*, 1973]. Substorms dissipate energy captured by the solar wind in the solar wind-magnetospheric-ionospheric system. They are divided into three phases: the growth phase, expansion phase, and recovery phase. The initial growth phase

adds magnetic flux to the tail lobes from dayside reconnection. The subsequent expansion phase is characterised by an exponential increase in auroral intensity and an enhancement of electrojet currents in the nightside magnetosphere. Lastly, during the substorm recovery phase, there is a reorganisation of the magnetospheric current system.

3 Instrumentation and Data

3.1 The Cluster Mission

This project uses data from ESA’s Cluster mission [*Escoubet et al.*, 1997], also known as Cluster II. Cluster II was launched in 2001 after the original Cluster mission was lost during launch in 1996. The mission consists of four spacecraft, in tetrahedral formation, each spinning at a rate of 15 rotations per minute. This setup enables Cluster to collect three-dimensional data on how the solar wind interacts with and affects Earth’s magnetosphere, atmosphere and aurorae. It has a highly elliptical polar orbit which evolves over time, so that the line of apsides has slowly rotated southwards. The spacecraft have a perigee of $\sim 4 R_E$ and an apogee of $\sim 19.6 R_E$. Throughout the course of a year, the spacecraft spend time in different regions of the Earth’s magnetosphere due to the relative motion of the magnetosphere to the spacecrafts’ fixed planes of orbits in inertial space.

Each spacecraft carries the same eleven instruments, as listed in Table 1.

3.1.1 The PEACE Instrument

The PEACE instrument measures the three-dimensional velocity distributions of electrons at a resolution of 4 s. The instrument is made up of two top-hat sensors, HEEA (High Energy Electron Analyser) and LEEA (Low Energy Electron Analyser), as well as a data processing unit [*Johnstone et al.*, 1997]. The sensitivity of LEEA is 5 times lower than HEEA as this instrument is optimised for higher electron fluxes at lower energies. These two sensors are mounted on opposite sides of each of the four spacecraft, with their field of view pointing radially away from the spin axis to reduce the entry of photoelectrons from the spacecraft.

FGM	Fluxgate Magnetometer
EDI	Electron Drift Instrument
ASPOC	Active Spacecraft Potential Control experiment
STAFF	Spatio-Temporal Analysis of Field Fluctuation experiment
EFW	Electric Field and Wave experiment
DWP	Digital Wave Processing experiment
WHISPER	Waves of High frequency and Sounder for Probing of Electron density by Relaxation experiment
WBD	Wide Band Data instrument
PEACE	Plasma Electron And Current Experiment
CIS	Cluster Ion Spectrometry experiment
RAPID	Research with Adaptive Particle Imaging Detectors
WEC	Wave Experiment Consortium (DWP, EFW, STAFF, WBD, and WHISPER)

Table 1: The eleven instruments on each Cluster spacecraft.

The 180° field of view of each electrostatic analyser is divided into 12 equal bins of width 15°. A pitch angle of 0° (180°) projects parallel (anti-parallel) to the magnetic field. The instrument has an energy range of 0.6 eV to 26.46 keV and can take measurements at 88 distinct energy bins. The first 16 energy bins are spaced linearly between energies 0.6 eV and 9.5 eV, whereas the remaining bins are spaced logarithmically across the rest of the energy range. The number of bins used depends on the chosen instrument mode.

Electrostatic Analysers Figure 3.1 illustrates the basic geometry of a top hat electrostatic analyser, as employed by the PEACE instrument. The device is comprised of an inner and outer hemisphere and a top cap. The inner hemisphere is given a positive voltage in comparison to the grounded outer hemisphere. Depending on the potential difference between hemispheres, an electron with a specific energy passes through the gap and hits the anode detector. Higher energy particles hit the outer hemisphere, while lower energy particles hit the inner hemisphere. Particle velocity distribution functions are measured by varying the potential difference to select different energy particles.

Two micro-channel plates (MCPs) are mounted between the detector and the hemispheres. These MCPs contain microscopic pores which are angled to allow particles to hit the pores' walls, causing the emission of secondary electrons that are accelerated towards the detector. These secondary electrons impact on more walls creating a cloud of secondary electrons, which are more easily detected by the anodes.

Data Mode This project has used data collected in the 'PITCH_SPIN' instrument mode. This data product, which is available every spin, is based on two instantaneous measurements of the pitch angle distribution per spin. The anode provides measurements for up

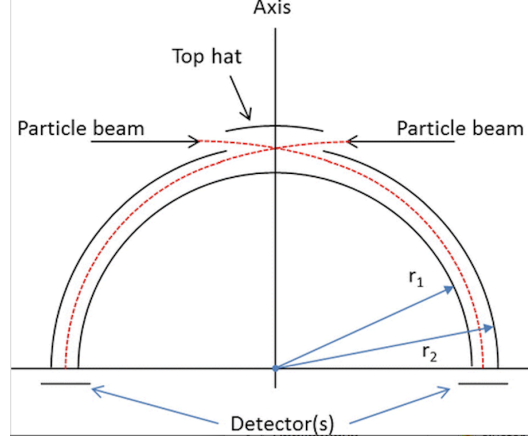


Figure 3.1: Basic geometry of a top hat electrostatic analyser. The path of the electrons is determined by the voltage [Farnell *et al.*, 2017].

to two pitch angles during each spin by recording at two specific azimuth angles separated by 180° . The PITCH_SPIN dataset is a two-dimensional product containing the twelve 15° pitch angle bins and 44 energy bins. At energies and pitch angles covered by both the HEEA and LEEA sensors, the average of the measured value is used.

3.1.2 The FGM Instrument

The FGM (FluxGate Magnetometer) instrument [Balogh *et al.*, 1997], which provides magnetic field information, plays an important part in determining the PITCH_SPIN data from the PEACE instrument, as velocity distribution functions are resolved in reference to the direction of the magnetic field. Each spacecraft is attached to a 5.2 m long boom, which holds two tri-axial fluxgate sensors to measure the magnetic field. The primary sensor is located at the end of the boom in order to reduce the effects of the spacecraft's magnetic field on its measurements. In normal mode, the instrument sends ~ 22 vectors/s to the ground. During burst mode, this increases to ~ 67 vectors/s. The resolution of the instrument varies depending on the magnitude of the magnetic field, ranging from a resolution of 7.8×10^{-3} nT

to 0.5 nT as the magnetic field increases from ± 64 nT to ± 4096 nT.

Fluxgate magnetometers consist of a ring core of a permeable alloy which is highly magnetic. Two coil windings: the drive winding and sense winding, are wrapped around this ring core. The ring core is made up of two separate half cores. As a current flows through the drive winding, one of the half cores will generate a magnetic field in the same direction as the external magnetic field, while the other half core will generate a second field in the opposite direction to the external magnetic field. Under an external magnetic field, the half core generating the opposing field comes out of saturation sooner than its counterpart. During this period, the two fields do not cancel out and the sense winding experiences a net change in flux. This net change induces a spike in voltage. A second voltage spike is also induced when the half core generating the opposing field comes out of saturation after the other half core towards the end of a current revolution in the drive winding. The magnitude and direction of the external magnetic field can be deduced by the size and phase of the two spikes in voltage.

3.1.3 The CIS Instrument

Ion measurements are provided by the Cluster Ion Spectroscopy (CIS) experiment [*Rème et al.*, 1997], which consists of two separate sensors called the COmposition and DIstribution Function analyser (CODIF) and the Hot Ion Analyser (HIA). Both instruments follow the top hat design. The HIA sensor has not been functional on Spacecraft 2 and 4, while the CODIF instrument has only been consistently reliable on Spacecraft 4.

CODIF CODIF measures the distributions functions of four different ion species: H^+ , He^+ , He^{2+} , and O^+ , with the use of a time-of-flight mechanism. In regions of very high ion flux,

however, the heavier mass channels become contaminated with protons. Ions which are selected by the top hot analyser traverse through a thin carbon foil which creates a secondary cloud of electrons. Once these electrons are detected by a secondary detector, a timer measures the time between the ions traversing the carbon foil and their detection at the primary detector. This enables the ions' charge per mass to be calculated.

CODIF is divided into a high G and low g section in order to the range of fluxes experienced by Cluster. The high G section has a geometric factor 100 times higher than the low g section. Each section has a field of view of $180^\circ \times 8^\circ$. The field of view of CODIF is tangential to the spacecraft. This enables the high G and low g sections to look spinward and anti-spinward respectively. The polar resolution is 22.5° and the azimuthal resolution is 11.2° . Due to bandwidth constraints, both sections cannot be operated simultaneously. Therefore, high G or low g are picked depending on the region Cluster is in. For example, high G is used in the magnetotail.

HIA The HIA sensor, on the other hand, does not distinguish between different ion species. The sensor measures ions in the energy to charge ratio range of 5 eV/e to 32 KeV/e, in comparison to 15 eV/e to 38 KeV/e for CODIF. HIA also has a high G and low g section, however the geometric factor difference between high G and low g is only 25 times in this case. HIA's field of view is also tangential to the spacecraft. The polar resolution of the high G section is 11.25° . The low g section has 8 central polar zones and 8 outer zones with resolutions of 5.625° and 11.25° respectively.

Data Products Onboard and ground-calculated moments are available from both the HIA and CODIF sensors. Due to calibration issues, the onboard moments for CODIF are in-

ferier to the ground-calculated moments. For HIA, onboard moments are calculated using full resolution distributions, while ground-calculated moments are calculated using lower resolution distributions telemetered from the spacecraft. In this case, the ground and onboard calibrations are the same, so onboard moments are preferred. As the upper limit of CODIF's energy range is higher than HIA's, CODIF moments are preferred for studying the magnetotail plasma sheet, where ion energies can extend beyond the energy range of both sensors, causing densities, temperatures, and velocities to be underestimates.

4 Techniques

4.1 Machine Learning

Machine learning allows computers to learn from existing datasets in order to gain an understanding of the data's structure via a hierarchy of concepts. The two types of machine learning [Sarkar *et al.*, 2018] used in this project are supervised learning and unsupervised learning.

4.1.1 Supervised Learning

In supervised learning, the machine learns to predict an output from the labelled training data provided. Mathematically, supervised learning derives the mapping function, $Y = f(X)$, between some input variables (training data), X , and their associated output variables (labels), Y , in order to assign labels to an unseen set of arrays. Supervised learning can further be divided into two types:

1. Classification: where the output variable is a class or group, e.g. strahl or halo.
2. Regression: where the output variable is a continuous value, e.g. estimating flux intensity.

4.1.2 Unsupervised Learning

In unsupervised learning, no training data is present so the algorithms are left to discover the internal representations of the input. Unsupervised learning can be further divided into three subsets:

1. Clustering: discover the inherent groupings of the data (sorting the data into clusters).

2. Density estimation: learn representations of the data via probability distributions.
3. Dimensionality reduction: provide compact, low-dimensional representation of the data.

4.2 Model Testing and Accuracy

A number of methods can be used to test the accuracy of supervised learning models and validate their results. A simple accuracy score comparing a trained model's labelling to pre-labelled data is generally the first step towards model validation. However, unless the dataset has roughly equally weighted classes, an accuracy score is not representative of the model's performance.

For datasets with high class imbalances, the F1 score and the ROC AUC (Receiver operating characteristic - Area under curve) score are more useful metrics [Flach and Kull, 2015]. The F1 score represents the harmonic mean of a model's precision, i.e. the proportion of predicted positives that are correctly classified, and recall, i.e. the proportion of actual positives that are correctly classified (also known as true positive rate or sensitivity).

Explicitly:

$$\text{precision} = \frac{\text{TP}}{\text{TP} + \text{FP}} \quad (4.1)$$

$$\text{recall} = \frac{\text{TP}}{\text{TP} + \text{FN}} \quad (4.2)$$

TP, TN, FP and FN represents the number of true positives, true negatives, false positives and false negatives respectively. This leads to:

$$\text{F}_1 \text{ score} = 2 \frac{\text{precision} \times \text{recall}}{\text{precision} + \text{recall}} = \frac{\text{TP}}{\text{TP} + \frac{\text{FN} + \text{FP}}{2}} \quad (4.3)$$

The ROC AUC score compares a binary classification model's specificity and sensitivity performance. The specificity is defined as the proportion of actual negatives that are

correctly classified:

$$\text{specificity} = \frac{\text{TN}}{\text{TN} + \text{FP}} \quad (4.4)$$

To calculate the ROC AUC score, the true positive rate (sensitivity) is plotted against the false positive rate (1 - specificity) for various thresholds, as varying the threshold changes the trade-off between these two values. The area under the plotted relationship between true and false positive rates corresponds to the ROC AUC score.

A more robust validation of a supervised learning models involves the use of the K-fold cross-validation procedure [Kohavi, 1995]. This builds off the simple train/test split validation method [Kohavi, 1995], whereby the manually labelled data is split into a training set and testing set. A model would use the training set to find how the labels correspond to the data input, and subsequently use its knowledge to classify the testing data, without having received this dataset's labels. An accuracy score can then be computed between the actual labels of the testing set and the model's predictive labelling. An advantage of this method means the model is not being trained and tested on the same dataset, which decreases the chance of models that over-fit from obtaining good scores. The K-fold cross-validation method splits the dataset into K-parts. The model will use K-1 parts to train, and subsequently use the remaining part for testing, obtaining an accuracy score. The same untrained model will cycle through all the parts to use a different one for testing, while training on the rest. This can be seen in Figure 4.1. This procedure builds up a more comprehensive picture of an accuracy metric, as the entire labelled dataset has been used in both training and testing. Ten folds were used during this project, as recommended [Kohavi, 1995]. It was also important to use a K-fold cross-validation programme [Scikit-Learn, 2007] which represents the weightings of classes in each individual part, in order to portray the entire

dataset.

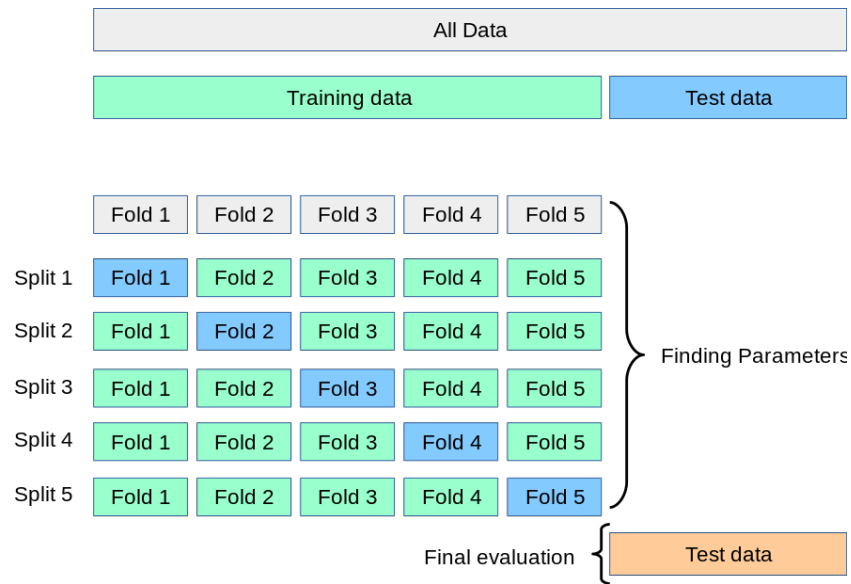


Figure 4.1: An example of the K-fold cross-validation procedure, where $K=5$ in this case [Scikit-Learn, 2007].

In terms of what is considered a good metric score, 90% is considered the benchmark for an excellent fitting model [Vallantin, 2018]. A model obtaining scores of above 70% is usually considered good, depending on the size of dataset and number of classes, and above 80% indicates a very good fitting model. If a model is showing metric scores of very close to 100%, then caution should be taken to make sure it is not overfitting to the training data.

5 Statistics of solar wind electron breakpoint energies using machine learning techniques

This work has been published in Bakrania et al. ‘Statistics of solar wind electron breakpoint energies using machine learning techniques’. A&A, 639 A46. (2020).

In this chapter, we demonstrate how machine learning techniques such as clustering can be applied to solar wind electron data, and we discuss its advantages over previous traditional methods, which involve fitting to electron velocity distributions. In order to demonstrate specific advantages, we analyse a particular physical property of solar wind electron populations - the breakpoint energy - by identifying core, halo, and strahl distributions at 1 au. Characterising the breakpoint energy is important as this property of a distribution function provides a diagnostic of the relative importance of scattering mechanisms such as Coulomb collisions and wave-particle interactions.

5.1 Data

We used the solar wind speed measurements from the Cluster-CIS instrument onboard the C4 spacecraft [Rème et al., 2001], while the position and magnetic field measurements are taken from the Cluster-FGM instrument [Balogh et al., 1997]. Using the CIS measurements, we initially separated our input electron pitch angle distribution data into three (fast, medium and slow) solar wind regimes to test our machine learning models. These regimes cover roughly 1-2 hours of data and have average solar wind velocities of 686 km/s, 442 km/s and 308 km/s. The time periods we identify with these fast, medium and slow wind regimes are 08:51-10:19 (02/03/2004), 00:38-01:35 (30/01/2003) and 04:33-06:18

(08/02/2009), respectively [Kajdič *et al.*, 2016]. We use these specific time intervals since they contain enough data points ($> 10,000$ samples) to effectively train and test our machine learning models.

5.2 Machine Learning Techniques

We predominantly used unsupervised learning algorithms to determine breakpoint energies, as well as separate halo and strahl. Unsupervised learning algorithms do not require ‘training’ so they are more time efficient than supervised learning algorithms. Our choice of algorithm is the K-means clustering method [Arthur, 2007] from the scikit-learn library [Pedregosa *et al.*, 2011]. Unsupervised learning algorithms have the advantage of not needing the user to assign labels to training data, which reduces bias and allows large surveys to be carried out more efficiently. In the K-means algorithm, the number of clusters, K , is manually set to 2 to reflect the number of populations we aim to distinguish between: a core cluster and a suprathermal cluster. To calculate the breakpoint energy at a specific pitch angle, our algorithm sorts between energy distributions, at that pitch angle, and separates the distributions into two groups on either side of the determined breakpoint energy. We define x_i as the vector representation of the phase space density (PSD) tuples, where the index i labels tuples of three subsequent energy bins (i.e. energy distributions spanning three energy bins). We define μ_j as the vector representation of two random PSD tuples, where the index j labels each cluster. The algorithm sorts these energy distributions into clusters by minimising the function:

$$\sum_{i=1}^n \sum_{j=1}^{K=2} \omega_{ij} \|x_i - \mu_j\|^2, \quad (5.1)$$

where

$$\mu_j = \frac{\sum_{i=1}^n \omega_{ij} x_i}{\sum_{i=1}^n \omega_{ij}}, \quad (5.2)$$

$$\omega_{ij} = \begin{cases} 1 & \text{if } x_i \text{ belongs to cluster } j \\ 0 & \text{otherwise,} \end{cases} \quad (5.3)$$

and n is the number of 3-tuples at a fixed pitch angle. As each 3-tuple overlaps with its neighbouring 3-tuples, $n = N_e - 2$, where N_e is the number of energy bins at each pitch angle. By minimising the function in Eq. (5.1), our algorithm calculates the breakpoint energy by: (1) randomly selecting two PSD vectors in the dataset to become the central points of each cluster, μ_j , known as centroids, (2) assigning all remaining PSD vectors, x_i , to the closest centroid, based on the least-square error between each vector and the centroids, (3) computing new centroids, μ_j , by calculating the average vector representation of the PSD vectors assigned to the previous centroid, (4) reassigning each PSD vector, x_i , to the new nearest centroid, μ_j , and (5) iterating steps 3 and 4 until no more reassignments occur.

Once the two clusters have been finalised, the breakpoint energy at the relevant pitch angle is determined to be the midpoint between the uppermost energy bin in the cluster of 3-tuples associated with lower energies (which represents the core), and lowest energy bin in the cluster of 3-tuples associated with higher energies (which represents suprathermal electrons). As the PSD decreases with increasing energy in the relevant energy range, we are able to locate a clear boundary between the two clusters. To separate strahl and halo electrons, we use energy distributions in conjunction with pitch angle distributions. The process of applying our K-means algorithm to pitch angle distributions is analogous to the method described above, with x_i now representing a pitch angle distribution at a certain energy, however in this case we find the ‘break’ in pitch angle instead. A detailed account of

how the K-means algorithm works is provided by *Arthur* [2007].

Figure 5.1 shows an example of how a simple collection of samples are sorted into clusters using the K-means clustering algorithm [*Arthur*, 2007].

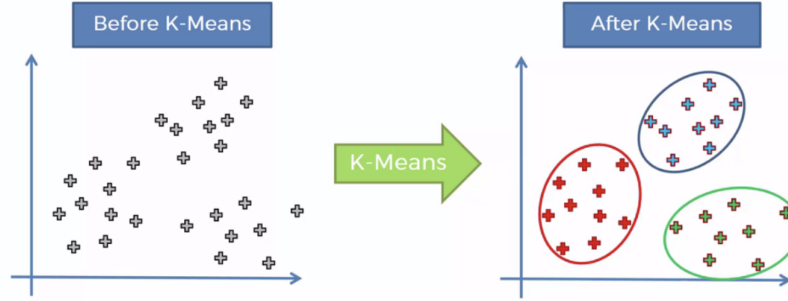


Figure 5.1: An illustration of how the K-means clustering algorithm sorts a scatter plot into three clusters [*Patil*, 2018].

We validate our clustering method by comparing test cases to an accurate supervised learning algorithm, trained on a subset of manually labelled (as halo or strahl) pitch angle and energy distributions. Once trained, the supervised learning algorithm predicts which class (halo or strahl) a new pitch angle or energy distribution belongs to. We compare supervised learning algorithms by calculating their ROC scores [e.g. *Flach and Kull*, 2015]. We find the K-Nearest Neighbours (KNN) [e.g. *Peterson*, 2009] algorithm performs best, achieving ROC scores $> 90\%$ in all tests. This model classifies data by finding the ‘majority vote’ of the nearest (labelled) neighbours to each unclassified data-point.

Figure 5.2 shows how two KNN models would be applied to the same set of data. Each dot represents a labelled data-point (by colour) and the empty space can be considered as unlabelled data-points. The colour shading shows how that particular space would be labelled from a model training on either the nearest labelled dot to that space (left) or the 5 nearest labelled dots to that space (right).

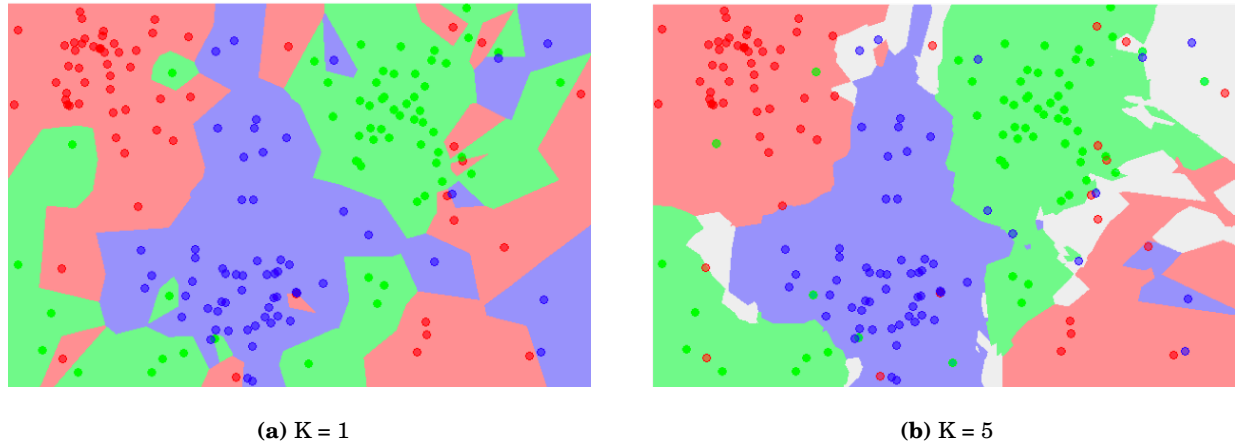


Figure 5.2: An illustration of how the KNN model decides classification boundaries based on labelled data. The circles represent labelled (by colour) data-points and the shading has been applied by each model depending on the closest coloured circles to that region [Mirkes, 2011].

5.3 Distinguishing Between Suprathermal and Core Electron Populations

We demonstrate the use of unsupervised clustering to calculate the breakpoint energy. Figure 5.3, which shows a cut of the differential energy flux distribution at constant pitch angle, visualises this breakpoint energy. Figure 5.3 contains three regions with different distribution functions. At energies below the spacecraft potential at ~ 10 eV, photo-electrons dominate (blue dots). At slightly higher energies, between 10 eV and ~ 45 eV, the distribution represents core electrons. At larger energies we observe the halo population. We fit a Maxwellian (red) and κ -distribution (yellow) [Štverák *et al.*, 2009] to the core and halo respectively, to determine the energy at which the distributions intersect, that is, the ‘breakpoint energy’.

The intersection in Figure 5.3 results in an estimated halo breakpoint energy of 45 ± 3 eV. We apply the same method to flux measured at pitch angles 0° and 180° , where the strahl

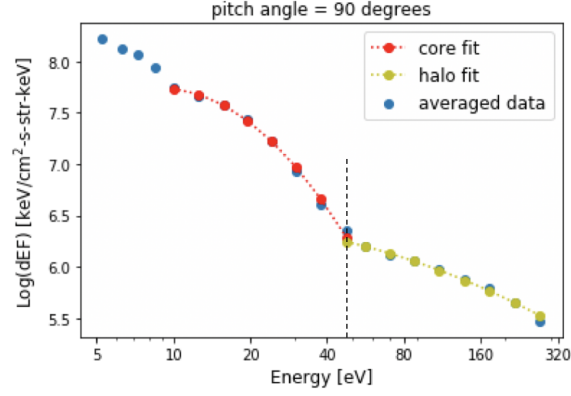


Figure 5.3: Differential energy flux as a function of energy at 90° , averaged across times 08:51-10:19 (02/03/2004) during our fast wind regime. The red curve represents a fit to the core electron energy range and the yellow curve to the halo energy range. The grey dashed line marks the so-called ‘breakpoint energy’ at 45 ± 3 eV.

carries the highest value of the flux density in the suprathermal energy regime. These intersections show a separation between the core and suprathermal strahl population at 42 ± 3 eV. We use the core-halo intersection in Figure 5.3, which is labelled by the dashed line, to validate our use of clustering analysis to calculate breakpoint energy, detailed below.

We omit energies below 10 eV and above 540 eV from our dataset and use the K-means clustering algorithm [Arthur, 2007] to classify the suprathermal and core populations, and hence calculate the breakpoint energy, at our choice of pitch angle. We assess the algorithm’s performance by comparing its classifications of the core population at each time step to an averaged distribution of the data, such as in Figure 5.3. This unsupervised learning method produces encouraging results. At 90° pitch angle, the algorithm estimates the average breakpoint energy to be $45 \text{ eV} \pm 3$. The accuracy score between algorithm’s classifications and a fit to the averaged distribution is 92.9%. As we predict binary classifications, we consider metric scores close to 90% as ‘good’ scores when testing our models, based on

what previous studies achieve [e.g. *Qian et al.*, 2015; *Zhang et al.*, 2017].

5.4 Separating Halo and Strahl Electrons

Figure 5.4 illustrates a typical differential energy flux distribution as a function of pitch angle and energy distribution for one particular time (08:57:28-08:57:32 on 02/03/2004) recorded by Cluster-PEACE. We limit the energy range to the suprathermal energy regime, as a result of our breakpoint energy analysis.

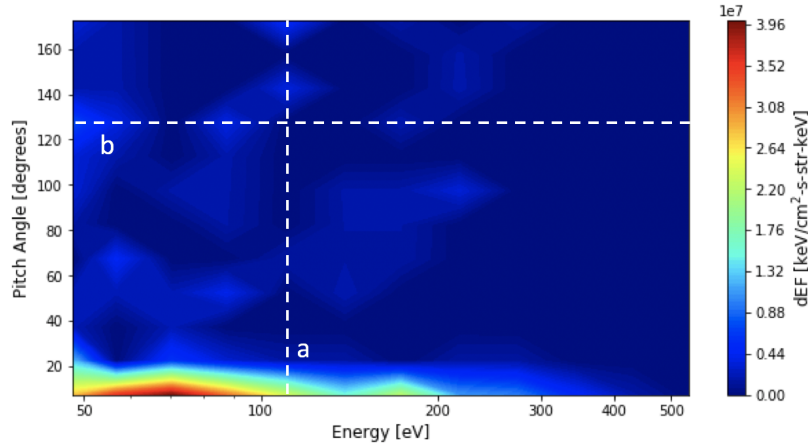


Figure 5.4: Two-dimensional colour plot of the measured electron differential energy flux, across a 4 second window (08:57:28-08:57:32 on 02/03/2004) during our fast wind regime. The data are plotted as a function of pitch angle (degrees) and energy (eV), across an energy range of ~ 44 eV to ~ 540 eV. The vertical and horizontal white dashed lines represent where cuts are made to obtain: a) the pitch angle distribution at 110.09 eV, and b) the energy distribution at 127.5° .

In order to show the average pitch angle distribution (PAD), we take vertical slices in Figure 5.4 at a given energy. The white line (a) in Figure 5.4 represents the slice from which we obtain the example PAD in Figure 5.5a. Below the typical breakpoint energy these distributions are relatively isotropic across all pitch angles, which is in contrast to

the strahl distribution [McComas *et al.*, 1992]. At higher energies within the suprathermal regime, PADs either show a quasi-isotropic distribution, which represents the halo, or an anisotropic distribution with peak fluxes recorded at 0° and/or 180° , which represents the halo population at all pitch angles overlaid with field-aligned strahl.

From our breakpoint energy analysis, we limit our input data to energies above 44 eV and convert these suprathermal data to PADs across our energy range, e.g. as shown in Figure 5.5a. We use an arbitrary 10-minute subset of time intervals, equivalent to 1800 samples, as training data. We assign each PAD a label, depending on whether strahl is or is not present. Subsequently, the entire set of PADs during our chosen wind speed regime are classified, based on a trained KNN model. We find a strong agreement between this supervised method and using K-means to cluster the fast wind set of PADs into two groups (halo and strahl), with a calculated ROC score of 90.3%.

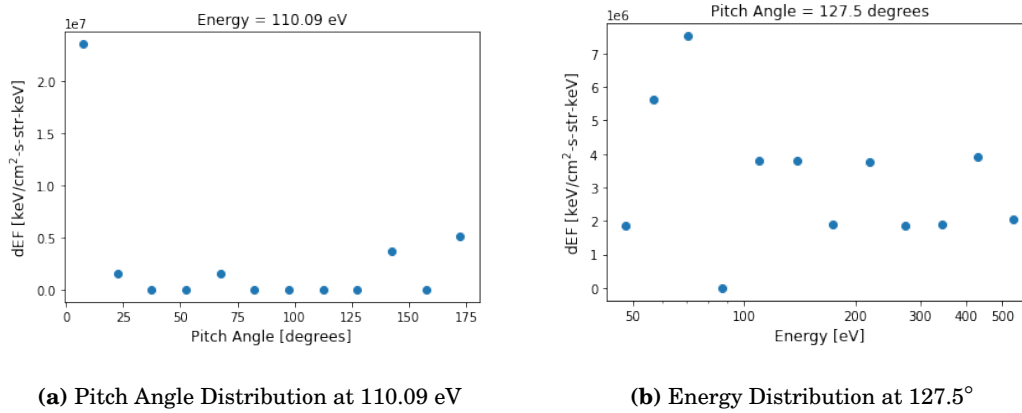


Figure 5.5: a) Pitch angle distribution at an energy of 110.09 eV and, b) energy distribution at a pitch angle of 127.5° as projected from the vertical and horizontal white lines in Figure 5.4.

Classifying PADs informs us of whether a strahl is present at a certain energy, however we require classification of the energy distributions at each pitch angle to extract the width

of the strahl. The white line (b) in Figure 5.4 represents the slice from which we obtain the example energy distribution in Figure 5.5b. We now use a 10-minute interval of energy distributions, at each pitch angle, for our training data and provide labels depending on whether strahl is present or not at that pitch angle. We find a strong similarity between the supervised and unsupervised methods, when classifying the entire set of flux-energy distributions, with a ROC score of 98.3%. This comparison therefore validates the use of the unsupervised method for any larger statistical survey.

For each time step, we combine the classifications of suprathermal PADs and suprathermal energy distributions to create a grid detailing whether the measured flux in each energy and pitch angle bin is dominated by halo electrons or by strahl electrons. A bin is identified as containing strahl if both the PAD and energy distribution it resides in are classed as strahl by the K-means algorithm. We show the results of our strahl and halo classification in fast wind in Figure 5.6. Each point represents a single measurement at a given pitch angle and energy, with the colour depicting the class (halo or strahl). The higher fluxes near 0° and 180° are associated with strahl (blue points). On occasion, broader strahl is detected, as illustrated by the presence of blue points at higher fluxes near 75° . The existence of red points across all pitch angles at lower fluxes confirms the presence of the halo as an isotropic population.

We show the results of our strahl and halo classification in slow wind in Figure 5.7. We see that the number of blue points, associated with the strahl, is much reduced in the slow wind than in the fast wind (see Figure 5.6). This finding is consistent with the observed lower occurrence of strahl during times of slow solar wind [e.g. *Gurgiolo and Goldstein, 2017*]. Both Figures 5.6 and 5.7 confirm that only halo electrons exist at pitch angles around

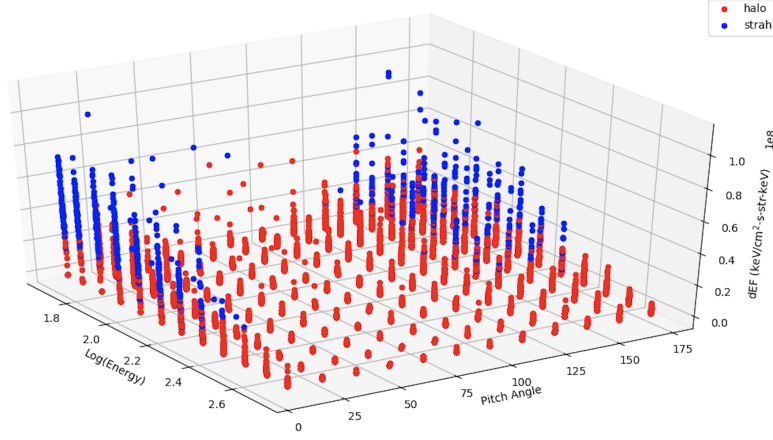


Figure 5.6: 3D scatter plot of the differential energy flux as a function of pitch angle and energy, for the fast solar wind dataset. The colours define whether the K-means clustering algorithm labels each bin as either containing strahl and halo flux (blue) or only halo flux (red).

90°. We see for both fast and slow wind cases that the strahl exhibits higher differential energy fluxes than the halo. The scattering of strahl electrons into the halo results in a larger spread of electrons across all pitch angles, decreasing the peak flux at any one pitch angle.

5.5 Calculating Relative Number Densities

After classifying the dataset into core, halo and strahl regions, we calculate the differential energy flux attributed to each population. In order to account for halo electrons in strahl pitch angle and energy bins, we subtract the halo flux, averaged over all pitch angles at a fixed energy, from strahl fluxes at that energy and assign it to the total halo flux. Differential energy flux relates to the partial number density (cm^{-3}) of each electron population as according to Eq. (5.4) [Wüest *et al.*, 2007]:

$$\Delta n \approx 5.4 \times 10^{-10} E^{-\frac{3}{2}} \Delta E \Delta \Omega J \text{ (cm}^{-3}\text{)}, \quad (5.4)$$

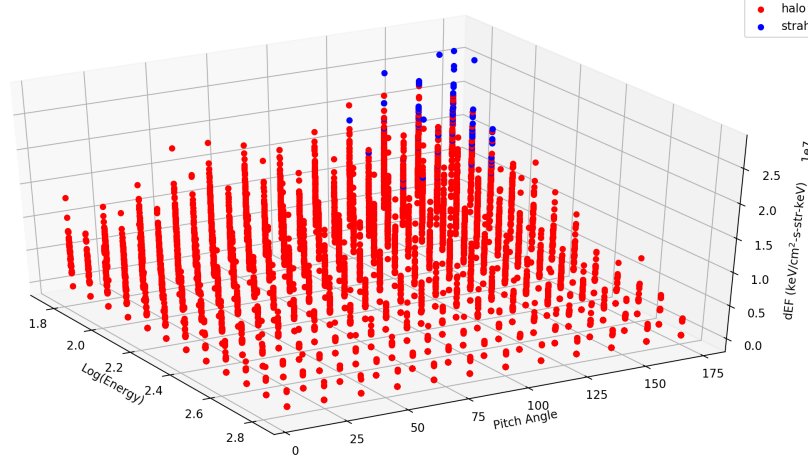


Figure 5.7: 3D scatter plot of the differential energy flux as a function of pitch angle and energy, for the slow solar wind dataset.

where E is the average energy within interval ΔE (both measured in keV/Q) and J is the average differential energy flux (keV/cm²-s-str-keV) at energy E . $\Delta\Omega$ is the solid angle ($\leq 4\pi$) over which J is measured and relates to the pitch angle widths.

In Figure 5.8, we show the conversion of differential energy flux to number density. In slow wind: the ratio $n_s/n_h = 0.003$ and $(n_s + n_h)/n_c = 0.025$ where n_s , n_h and n_c represent the strahl, halo and core number densities. In intermediate wind: $n_s/n_h = 0.53$ and $(n_s + n_h)/n_c = 0.043$ while in fast wind: $n_s/n_h = 0.79$ and $(n_s + n_h)/n_c = 0.094$.

Our calculated densities are of the same order as those determined by Štverák *et al.* [2009], who found $(n_s + n_h)/n_c = \sim 0.1$ and 0.04-0.05 in fast and slow wind respectively. This test confirms that our algorithm is capable of differentiating between solar wind electron populations to a similar degree as previous results, with a very different method.

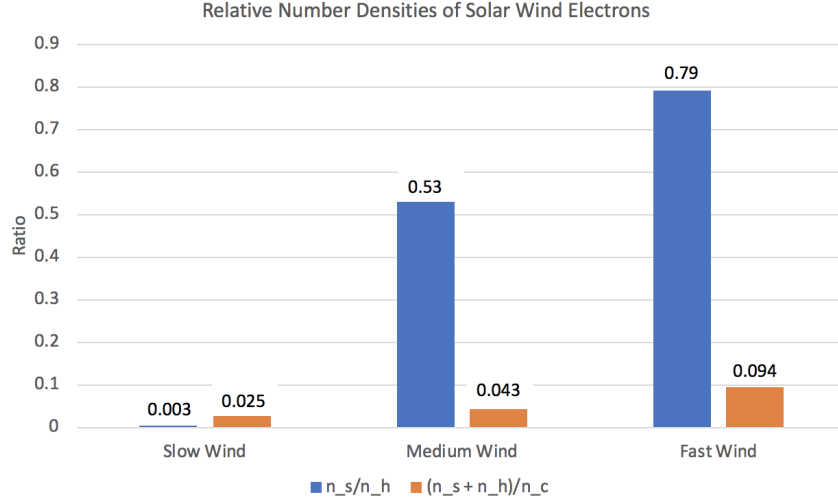


Figure 5.8: n_s/n_h and $(n_s + n_h)/n_c$ ratios for slow, medium and fast solar wind.

5.6 Statistical Study of Breakpoint Energy versus Solar Wind Speed

We then used ten years of pristine solar wind data, from 2001 to 2010, to quantify the relationship between strahl and halo breakpoint energies and other solar wind parameters, notably solar wind speed and core temperature. By quantifying the halo and strahl breakpoint energies separately, we determine if each suprathermal population is governed to the same extent by ambient conditions, or if they scale with each bulk parameter differently. For this study, we use Cluster-PEACE data in units of phase space density and split the data into four-minute intervals. The average solar wind speed during each interval is recorded using CIS measurements.

5.6.1 Confirming Cluster is in Pristine Solar Wind

The first step towards a statistical study involved collating a list of times when Cluster is in the pristine solar wind. This means the spacecraft should be outside the bow shock and not magnetically connected to it. To determine this, we used a model of the Earth's bow shock

position [*Chao et al.*, 2002]:

$$r = r_0 \left(\frac{1 + \epsilon}{1 + \epsilon \cos \theta} \right)^\alpha \quad (5.5)$$

where r_0 is the sub-solar bow shock standoff distance, α represents the level of tail flaring, ϵ represents the bow shock's eccentricity. r is the distance from the bow shock's surface to the centre of the Earth at an angle θ from the x -direction in GSE coordinates. ϵ is equal to 1.029 [*Chao et al.*, 2002] and α and r_0 are given by the following equations:

$$\alpha = a_5(1 + a_6 B_z)(1 + a_7 D_p)(1 + a_{10} \ln(1 + \beta))(1 + a_{14} M_{MS}) \quad (5.6)$$

$$r_0 = a_1(1 + a_3 B_z)(1 + a_9 \beta)(1 + a_4 \frac{((a_8 - 1)M_{MS}^2 + 2)}{((a_8 + 1)M_{MS}^2)})D_P^{-1/a_{11}} \quad (5.7)$$

where B_z is the IMF north-south component, D_p the upstream solar wind dynamic pressure, β is the plasma beta and M_{MS} the magnetosonic mach number. The variables in equations (5.6) and (5.7) were calculated as [*Chao et al.*, 2002]: $B_z = -0.35$, $D_p = 2.48$, $\beta = 2.08$, $M_{MS} = 6.96$, $a_1 = 11.1266$, $a_3 = -0.0005$, $a_4 = 2.5966$, $a_5 = 0.8182$, $a_6 = -0.017$, $a_7 = -0.0122$, $a_8 = 1.3007$, $a_9 = -0.0049$, $a_{10} = -0.0328$, $a_{11} = 6.047$ and $a_{14} = -0.002$.

The value θ in equation (5.5) was determined by Clusters position. When Cluster is on the dayside:

$$\theta = \sin^{-1} \left(\frac{\sqrt{p_y^2 + p_z^2}}{\sqrt{p_x^2 + p_y^2 + p_z^2}} \right) \quad (5.8)$$

and on the nightside:

$$\theta = \pi - \sin^{-1} \left(\frac{\sqrt{p_y^2 + p_z^2}}{\sqrt{p_x^2 + p_y^2 + p_z^2}} \right) \quad (5.9)$$

where p_x , p_y and p_z are Cluster's position coordinates obtained from the FGM instrument onboard [*Balogh et al.*, 1997]. Times were then collected for when Cluster's position d :

$$d = \sqrt{p_x^2 + p_y^2 + p_z^2} \quad (5.10)$$

is larger than the value of r at the angle θ .

Once times of when Cluster was outside the bow shock were obtained, FGM measurements [Balogh *et al.*, 1997] were used to determine the magnetic field direction during those times. By combining Cluster's position coordinates with the magnetic field vector at that point, we could collate a list of times when the field is not intersecting with the Earth's bow shock, meaning it is not magnetically connected. Figure 5.9 displays a particular time when this is the case.

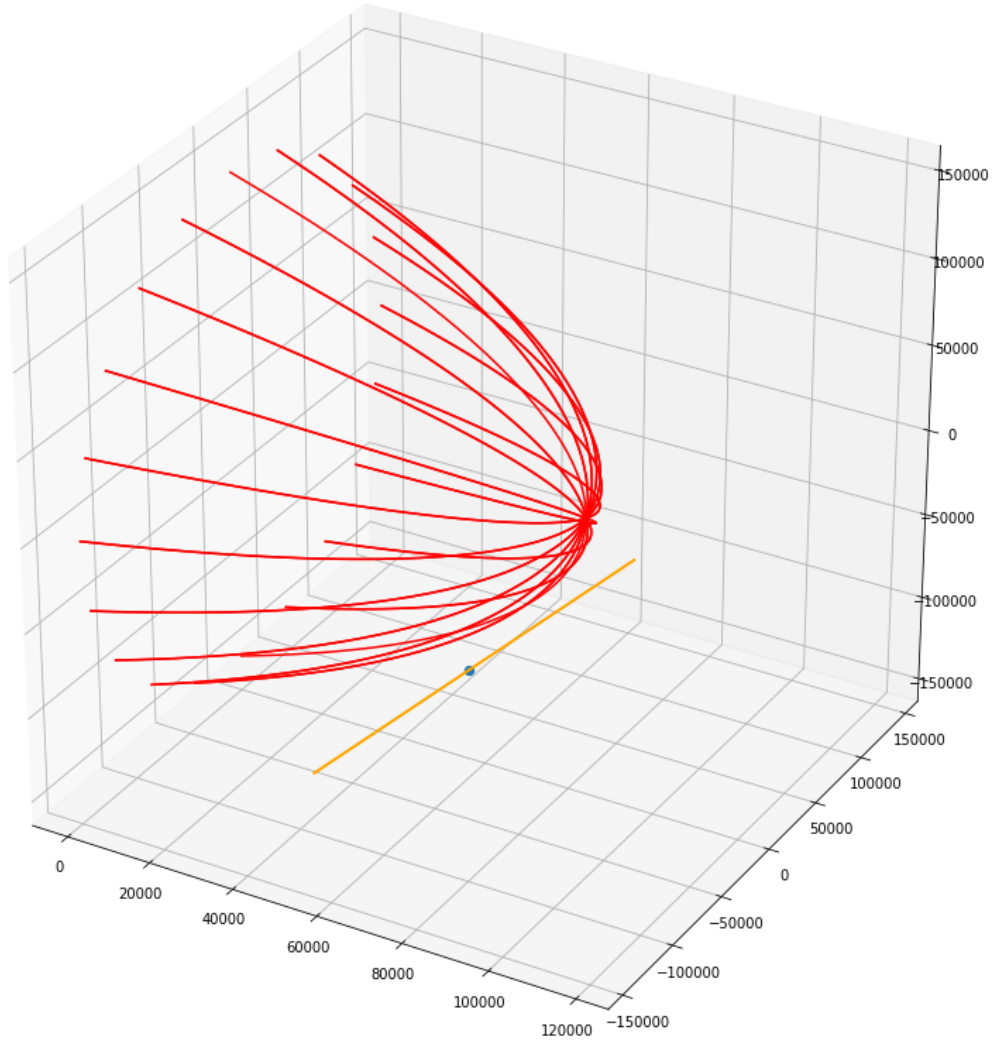


Figure 5.9: A plot showing a particular time when Cluster is outside the bow shock and magnetically disconnected from it. The red curves represent the bow shock surface, the blue dot is Cluster's position and the orange lines show the direction of the magnetic field at that point and time.

We calculate the halo breakpoint energy, during each four-minute interval, by applying K-means clustering to phase space density values at 90° pitch angles, over a range of energies from 19 eV to 240 eV. Calculating the strahl/core breakpoint energy entails applying

these K-means models to pitch angles and intervals which contain strahl. We achieve this by classifying flux-energy distributions during each interval, using the method in Section 5.4, to determine if strahl is present at 0° or 180° .

Once the breakpoint energy during each 4-minute interval had been determined, the core energies below the breakpoint energy were converted to velocities. Converting to velocities allowed a Maxwellian velocity distribution function (see equation 5.11) [Štverák *et al.*, 2008] to be fitted to the phase space density data across these core velocities.

$$f_c = n_c \left(\frac{m}{2\pi k} \right)^{3/2} \frac{1}{T_{c\perp} \sqrt{T_{c\parallel}}} \exp \left\{ \left[-\frac{m}{2k} \left(\frac{v_\perp^2}{T_{c\perp}} + \frac{v_\parallel^2}{T_{c\parallel}} \right) \right] \right\} \quad (5.11)$$

Where n_c is the core density, m the electron mass, k is Boltzmann's constant, $T_{c\perp}$ and $T_{c\parallel}$ are the core perpendicular and parallel temperatures and v_\perp and v_\parallel are the perpendicular and parallel velocities. By inputting known values for f_c (the phase space density), m , v and k , our fitting programme [SciPy, 2016] was able to estimate the core temperature and density which would enable a fit to converge on the smaller core velocities. An example of this is seen in Figure 5.10.

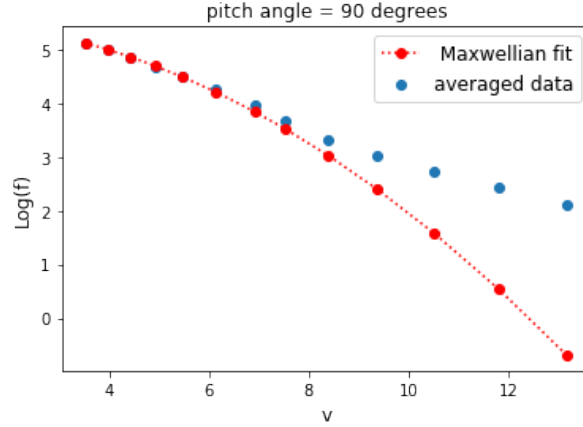


Figure 5.10: A velocity distribution plot showing average phase space density (blue scatter points) vs. velocity over a 4-minute interval. The red line represents a Maxwellian fit to energies below the breakpoint energy.

5.6.2 Results

Figure 5.11 shows the halo breakpoint energy vs. core temperature distribution in a ‘violin plot’ to visualise the distribution of data points after binning the data into widths of 50 km/s. A violin plot is similar to a box plot, with the addition that the horizontal extent of each violin element represents a density plot of the data at different values. The red regions in Figure 5.11 visualise these density plots.

The widths of the red regions show that data are clustered about certain energies across all wind speeds. These regions of higher density in fact point to the energy channels (30.1 eV, 37.7 eV, 47.9 eV, 56.7 eV and 70.5 eV) within the C2-PEACE instrument’s dataset. As the instrument contains discrete energy channels with relatively large spacing, we observe bumps in the violin plots rather than a smooth distribution, due to our reliance on these energy channels for calculating the breakpoint energy. Figure 5.11 shows a clear positive correlation between halo breakpoint energy and core temperature, $k_B T_c$, with a gradient of

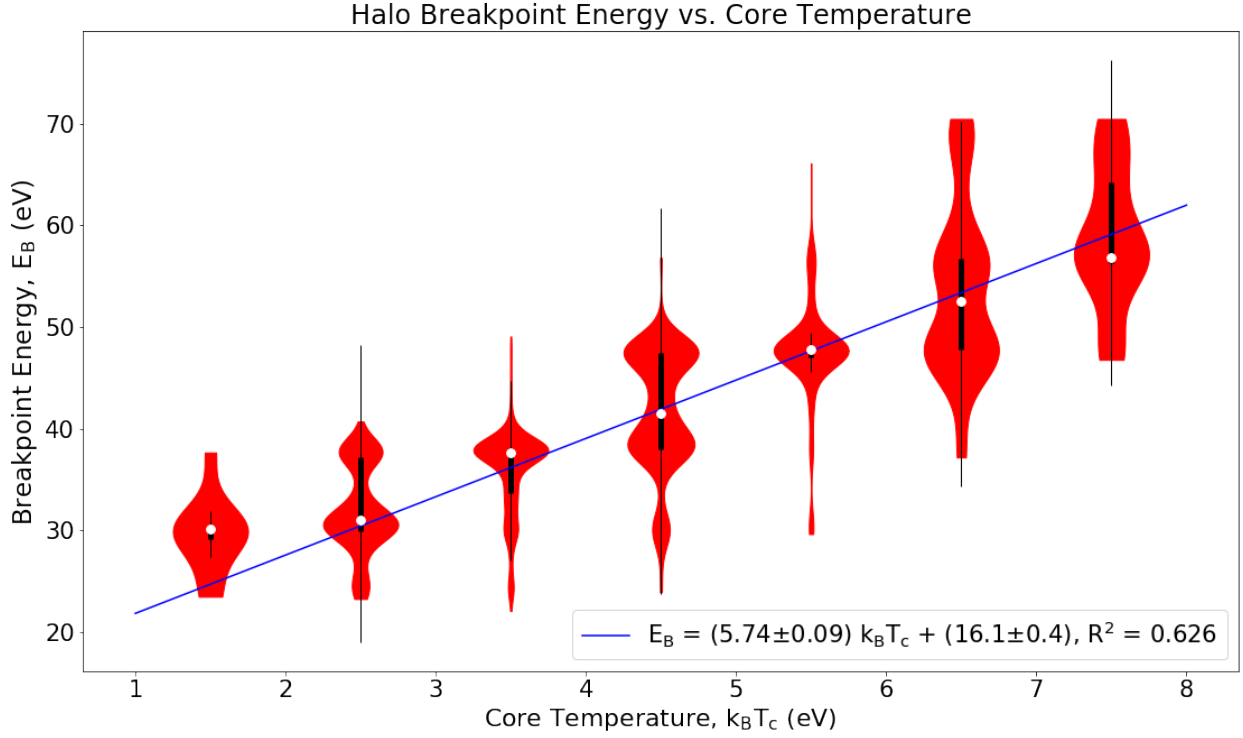


Figure 5.11: ‘Violin plot’ of halo breakpoint energy against core temperature. The blue line shows the line of best fit. The white dots indicate the median of breakpoint energies and the thick black lines show the inter-quartile ranges (IQR). We plot the thin black lines to display which breakpoint energies are outliers. They span from $Q3 + 1.5 \times IQR$ to $Q1 - 1.5 \times IQR$, where $Q3$ and $Q1$ are the upper and lower quartiles, respectively. The horizontal width of the red regions represents the density of data points at that given breakpoint energy.

5.74 ± 0.09 . A statistical P-test produces a p-value of < 0.0001 , showing this relationship is significant at the $p = 0.05$ (5%) level [Rice, 1990]. The R-squared value of 0.626 indicates ~63% of variation in halo breakpoint energy can be described by this correlation. Very small inter-quartile ranges are observed in the 1-2 eV and 5-6 eV bins, while large inter-quartile ranges are observed in bins 4-5 eV and 6-7 eV. The results for the strahl breakpoint energy vs. core temperature are shown in Figure 5.12.

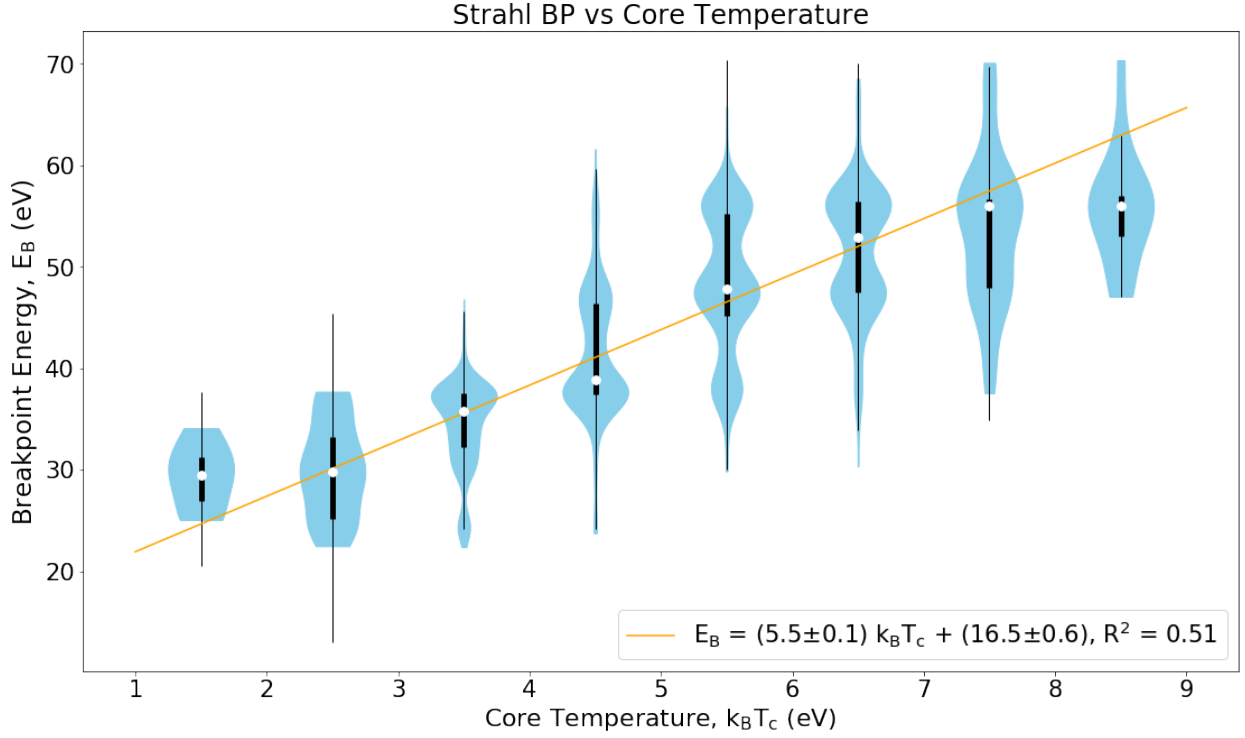


Figure 5.12: ‘Violin plot’ of strahl breakpoint energy against core temperature. The orange line shows the line of best fit. The remaining features are the same as in Figure 5.11.

In both Figures 5.11 and 5.12, there is small discrepancy between the line of best fit and the median at core temperatures between 2 eV and 8 eV. When $T_c < 2$ eV, the linear fit underestimates all of the measured breakpoint energies, lying below the lower quartile range in both cases. In the strahl’s case, the median and upper quartile at $T_c > 8$ eV drop significantly below the line of best fit. Figure 5.12 suggests the dependence between core temperature and halo and strahl breakpoint energies differs. This is evidenced by the strahl breakpoint energy relation exhibiting a smaller gradient (5.5 ± 0.1) and larger variance, based on the R-squared value of 0.51, with T_c than the halo’s relation. A p-value of < 0.0001 suggests that this positive correlation between strahl breakpoint energy and core temperature is also highly significant at the $p = 0.05$ level.

Figure 5.13 shows the results of our study to determine the relationship between halo breakpoint energy and solar wind speed. The collisionality of the solar wind plasma varies with its velocity, with slow wind typically exhibiting a higher collisionality than fast wind [Scudder and Olbert, 1979; Lie-Svendsen *et al.*, 1997; Salem *et al.*, 2003; Gurgiolo and Goldstein, 2017]. Therefore, comparing breakpoint energy to solar wind velocity provides useful information on the scaling of breakpoint energy with the collisionality of the ambient plasma. Solar wind velocity is also a good indicator of the origin of the solar wind [Geiss *et al.*, 1995; Habbal *et al.*, 1997], enabling us to investigate if breakpoint energy profiles vary with differing solar wind source regions. The gradient in Figure 5.13 is -5.9 ± 0.1 eV per 100 km/s. The R-squared value of 0.487 is lower than 0.626 in Figure 5.11, indicating that halo breakpoint energy exhibits a stronger correlation with core temperature than with solar wind speed. A statistical P-test produces a p-value of <0.0001 , showing this relationship is significant at the $p = 0.05$ (5%) level.

The distribution of breakpoint energies with wind speed in Figure 5.13 displays a step function at about 500 km/s. The lower quartile within the 450-500 km/s bin lies above the upper quartiles in faster speed bins. Fitting two linear fits to solar wind speeds below and above 500 km/s separately produces gradients of -4.2 ± 0.1 eV per 100 km/s and -3.5 ± 0.1 eV per 100 km/s respectively. The associated R-squared values are 0.588 and 0.651 respectively; both larger than a value 0.487 for a single linear fit, indicating that two separate correlations better describe the distribution in Figure 5.13 than a single correlation. The two correlations are also significant at the $p = 0.05$ (5%) level. The data-points in Figure 5.13 are distributed along a larger range of breakpoint energies at lower wind speeds than higher wind speeds. However, according to the inter-quartile ranges for the majority of data-

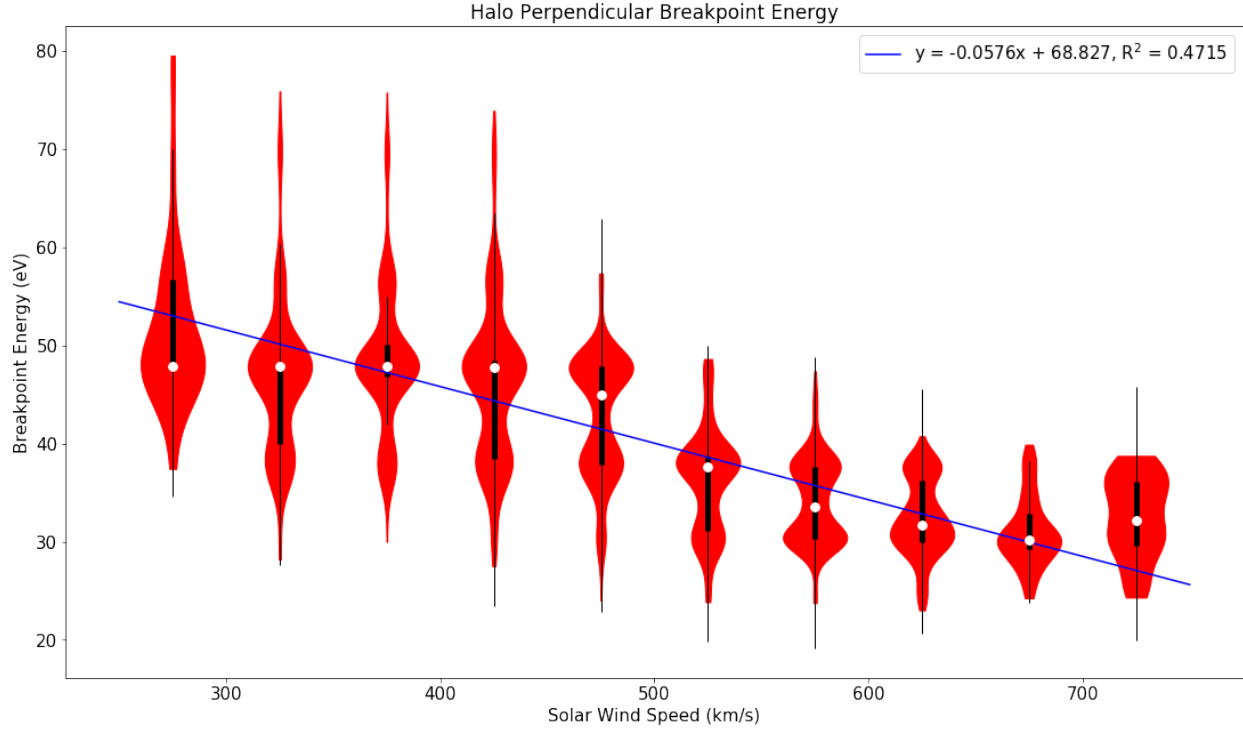


Figure 5.13: ‘Violin plot’ of halo breakpoint energy against solar wind speed. The blue line shows the line of best fit. The remaining features are the same as in Figure 5.11.

points, the variance about the median values is relatively small, with the exception of a few outliers. The medians themselves do not deviate significantly from the line of best fit across all wind speeds, with the largest median residual equalling 5 eV in the <300 km/s bin. There is some evidence for positive or negative skewness at certain solar wind velocities, such as in the <300 km/s and 400-450 km/s bins, as can be seen when the median appears to lie on one of the edges of the inter-quartile range.

Figure 5.14 shows the strahl breakpoint energy variation with solar wind speed. According to our linear fit, the rate of decrease of strahl breakpoint energy with solar wind speed is -5.7 ± 0.1 eV per 100 km/s. Solar wind speed has a smaller correlation with strahl breakpoint energy than halo breakpoint energy, based on the steepness of each gradient and R-squared

values. This R-squared value of 0.460 in Figure 5.14 also indicates that the strahl breakpoint energy has a weaker correlation statistically with solar wind speed than with core temperature, as the line of best fit describes less of the variation. This is also the case for the halo breakpoint energy. A p-value of <0.0001 indicates that this negative correlation is also highly significant at the $p = 0.05$ level.

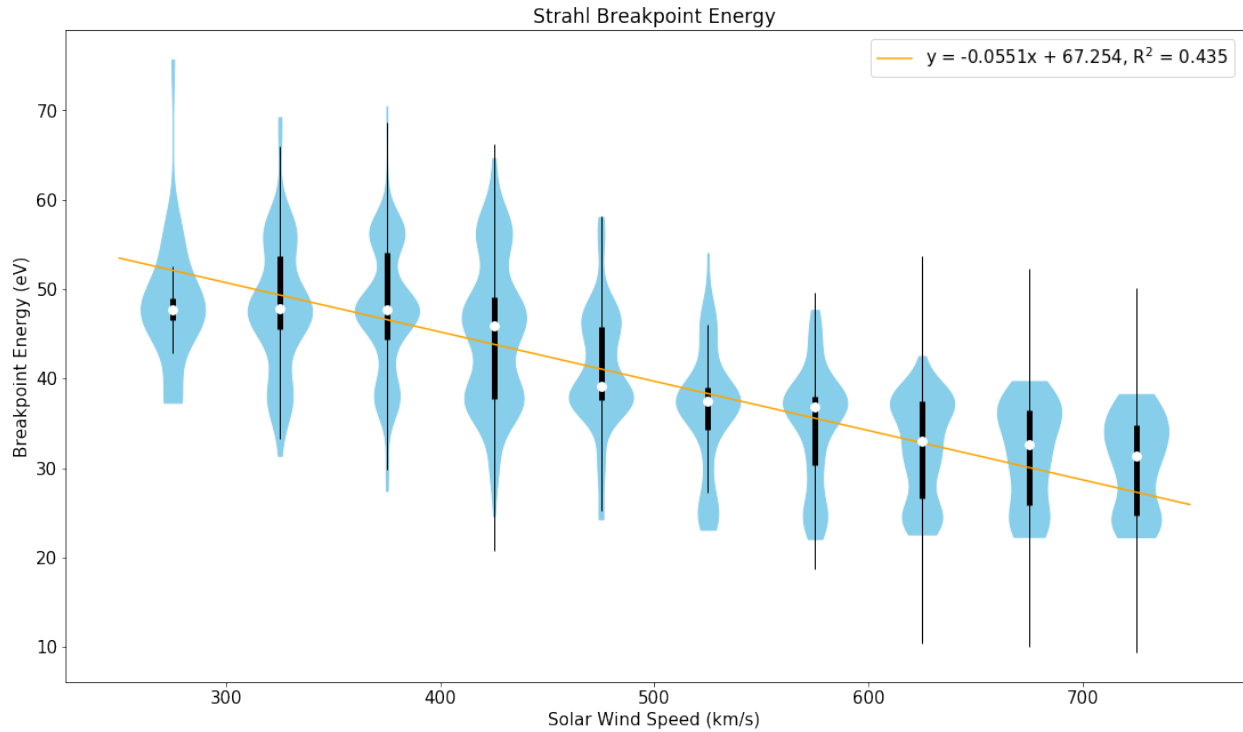


Figure 5.14: ‘Violin plot’ of strahl breakpoint energy against solar wind speed. The orange line shows the line of best fit. The remaining features are in the same format as Figure 5.11.

Similar to Figure 5.13, the variation in breakpoint energy in the strahl violin plot is larger at smaller wind speeds. However, unlike for halo, the 400-450 km/s bin has a much larger variance than the <300 km/s bin, as evidenced by their inter-quartile ranges. This larger spread of data at medium wind speeds explains why the strahl’s R-squared value is lower than the halo’s. The lack of skewness in Figure 5.14 shows that the data are dis-

tributed more symmetrically in the strahl's case than the halo's. The sum of the median residuals are also smaller for the strahl, with the largest median residual at 3.5 eV in the <300 km/s solar wind speed bin. A step function is less apparent in Figure 5.14, however there is a clear distinction between the median breakpoint energy relation with wind speed in slow winds (<450 km/s), compared to fast winds. Table 2 contains the gradients and R-squared values of the correlations in Figures 5.11, 5.12, 5.13, and 5.14.

Table 2: Correlations between halo and strahl breakpoint energies with core temperature, T_c and solar wind speed, V_{sw} , as represented by the gradients and R-squared, R^2 , values.

Population	T_c		V_{sw}	
	E_{bp}/T_c	R^2	E_{bp}/V_{sw}	R^2
			[eV/(km/s)]	
Halo	5.74	0.626	-0.059	0.487
Strahl	5.5	0.51	-0.057	0.460

5.7 Discussion

In this study, we use the K-means algorithm to successfully distinguish between the three populations and we train a supervised learning algorithm (K-nearest neighbours) to classify a subset of the pitch angle and energy distributions. There is a strong agreement between the two machine learning methods, allowing us to apply the K-means clustering method to a larger subset of solar wind electron data at different solar wind velocities. Machine learning algorithms provide us with an efficient method of classification from which small scale variations of electron populations in relation to energy and pitch angle can be derived. By classifying a single distribution at each time step, we build up a high resolution pic-

ture of suprathermal breakpoint energy and relative number density, including how they evolve with different parameters. The techniques we employ can be easily applied to any classification problem where sufficient data are available.

Distinguishing between strahl, halo, and core electron populations allows us to calculate their relative number densities, in order to compare our method to previous results. *Štverák et al.* [2009] show that suprathermal electrons in the fast wind constitute $\sim 10\%$ of the total electron number density, while in slow wind they occupy 4% to 5% of the total electron density. In comparison, we obtain values of $\sim 9.4\%$ and 2.5-4.3% for fast and slow wind respectively. Obtaining densities of the same order as *Štverák et al.* [2009] confirms that our method is capable of distinguishing between multiple solar wind electron populations to a similar degree as alternative methods. Being a zeroth order moment, there is a smaller level of uncertainty when calculating the density, as opposed to the breakpoint energy or higher order moments, by fitting distribution functions. Using machine learning techniques instead of fitting bi-Maxwellian and bi-Kappa functions to electron velocity distributions, which involves fixing certain parameters [*Štverák et al.*, 2009], eliminates the need to use prior assumptions about these solar wind electron populations. Therefore, our new method results in more robust estimations of the solar wind electrons' breakpoint energies.

The observation that the majority of the halo population is formed due to strahl scattering [*Saito and Gary*, 2007; *Pagel et al.*, 2007; *Štverák et al.*, 2009] explains the relationship between n_s/n_h and wind speed in Figure 5.8. Strahl in slow solar wind undergoes more scattering per unit distance than in faster wind [e.g. *Fitzenreiter et al.*, 1998], leading to a higher value of n_h/n_e at 1 au. We observe a near absence of strahl in very slow solar wind at velocities of 308 km/s (see Figures 5.7 and 5.8), which is consistent with observations from

previous studies [e.g. *Fitzenreiter et al.*, 1998; *Gurgiolo and Goldstein*, 2017; *Graham et al.*, 2018]. By analysing a number of periods of slow solar wind, *Fitzenreiter et al.* [1998] find that the strahl generally has a larger width in slow solar winds than fast, while *Gurgiolo and Goldstein* [2017] find that strahl is often not present at solar wind velocities $\lesssim 425$ km/s. *Graham et al.* [2018] also note an absence of strahl during certain slow solar wind times. This absence of strahl remains unexplained. Possible hypotheses include: Coulomb pitch angle scattering which counteracts magnetic focussing effects during strahl formation [*Horaites et al.*, 2019], intense scattering due to broadband whistler turbulence [*Pierrard et al.*, 2001], and the lack of initial strahl formation during the production of slow solar wind [*Gurgiolo and Goldstein*, 2017].

Instead of finding the intersection between core and suprathermal fitting functions [e.g. *Pilipp et al.*, 1987a; *McComas et al.*, 1992; *Štverák et al.*, 2009], a method which according to *McComas et al.* [1992] produces ‘somewhat arbitrary’ values, our method calculates the breakpoint energy based on the data recorded in each individual pitch angle and energy bin. Our method calculates breakpoint energy values of both sunward and anti-sunward strahl, occasionally obtaining two strahl breakpoint energy values at a single time if bi-directional strahl is present. An alternative method is presented by *Štverák et al.* [2009] who discard sunward strahl in their calculations of the strahl $E_{bp}/k_B T_c$ ratio at each radial distance. By characterising both sunward and anti-sunward strahl, our method significantly improves the characterisation of all electron beams in the solar wind.

Our work on the core velocity distribution functions elucidates the relative correlation between core temperature, T_c , and both halo and strahl breakpoint energies. Using core temperature as a reference point enables us to predict to what extent strahl and halo char-

acteristics scale to characteristics of the core. The core temperature has a strong correlation with both suprathermal breakpoint energies, with the halo breakpoint energy exhibiting a closer correlation than the strahl's. Both halo and strahl breakpoint energies statistically have a stronger correlation with core temperature than with solar wind speed. The gradients between breakpoint energy and core temperature are calculated as 5.74 ± 0.09 and 5.5 ± 0.1 for halo and strahl respectively.

The linear relationship that we observe between breakpoint energy and core temperature is in line with previous measurements [e.g. *McComas et al.*, 1992; *Štverák et al.*, 2009], for both the halo and strahl. According to *Scudder and Olbert* [1979], a linear trend in the halo relation also follows under the assumption that binary Coulomb collisions dominate electron dynamics in the solar wind. However, in order to align with available experimental data, *Scudder and Olbert* [1979] set a scaling factor of $E_{bp}/k_B T_c = 7$, which differs from our scaling factor of $E_{bp}/k_B T_c = 5.5 \pm 0.1$. With a scaling factor of $E_{bp}/k_B T_c = 7$, *Scudder and Olbert* [1979] predict that a transformation of thermal electrons into the suprathermal population occurs as the solar wind flows out from the Sun. Findings by *Štverák et al.* [2009], on the other hand, show that the $(n_h + n_s)/n_c$ ratio remains roughly constant with heliocentric distance in the slow wind, suggesting a lack of interchange between the thermal and suprathermal populations. However *Štverák et al.* [2009] observes some variability in the $(n_h + n_s)/n_c$ ratio in the fast wind, which they attribute to either statistical effects due to a lack of samples or a possible ‘interplay’ between thermal and suprathermal electrons. *Scudder and Olbert* [1979] also predict that the halo $E_{bp}/k_B T_c$ ratio remains constant with heliocentric distance, whereas *Štverák et al.* [2009] find that the halo $E_{bp}/k_B T_c$ ratio decreases with heliocentric distance. These findings by *Štverák et al.* [2009], along with the discrep-

ancy between our calculated ratio of $E_{bp}/k_B T_c = 5.5 \pm 0.1$ and the prediction of $E_{bp}/k_B T_c = 7$, suggest that the model of *Scudder and Olbert* [1979] requires a minor update to either the theory or to the input parameters. The discrepancy, however, may also be indicative of other processes, such as wave-particle scattering [e.g. *Gary et al.*, 1994], that possibly modifies the ratio between breakpoint energy and core temperature while preserving its linear relationship.

In our statistical study, we find that both strahl and halo breakpoint energies decrease with solar wind speed. At all solar wind velocities, as well as core temperatures, the halo breakpoint energy is larger than the strahl's at equivalent velocities and temperatures. The halo breakpoint energy exhibits a higher correlation with the solar wind speed than strahl. The anti-correlation between the two parameters corresponds with the finding that $(n_h + n_s)/n_c$ increases with solar wind speed [Štverák *et al.*, 2009], where n_h , n_s and n_c represent the halo, strahl, and core number densities. Assuming all plasma parameters are kept constant, except for the core density and temperature, the relative density of suprathermal electrons will increase if the breakpoint energy decreases. This observed relationship between solar wind speed and electron ratios is most likely a result of the lower collisionality of fast solar wind [*Scudder and Olbert*, 1979; *Lie-Svendsen et al.*, 1997; *Salem et al.*, 2003; *Gurgiolo and Goldstein*, 2017], which results in more distinctive non-thermal features of the electron velocity distribution function. Further work is required to analyse whether different breakpoint energy relations exist that depend on the source of solar wind. Initial findings in this study suggest the existence of two distinct relationships in the halo breakpoint energy vs. wind speed distribution, with a step function at 500 km/s. This finding links to a sharp distinction between fast and slow solar winds [*Feldman et al.*, 2005]. There-

fore the origin of the solar wind, i.e., coronal holes for fast wind or streamer belt regions for slow wind, potentially plays a role in the definition of thermal and non-thermal electron populations. A step function is less obvious in the strahl breakpoint energy vs. solar wind speed distribution.

6 Using dimensionality reduction and clustering techniques to classify space plasma regimes

This work has been published in Bakrania et al. ‘Using dimensionality reduction and clustering techniques to classify space plasma regimes’. Front. Astron. Space Sci. (2020).

Particle populations in collisionless space plasma environments, such as the Earth’s magnetotail, are traditionally characterised by the moments of their distribution functions. 2D distribution functions in pitch angle and energy, however, provide the full picture of the state of each plasma environment, especially when non-thermal particle populations are present that are less easily characterised by a Maxwellian fit. These non-thermal plasma populations are ubiquitous across the solar system. They make crucial contributions to the bulk properties of a plasma, such as the temperature and collisionality [Hapgood et al., 2011]. Magnetic reconnection, for example, heats non-thermal seed populations in both the diffusion and outflow regions, making them an important component of the overall energisation process [Øieroset et al., 2002]. High-quality measurements and analysis of collisionless plasmas are consequently of key importance when attempting to understand these non-thermal populations.

Distribution functions, unlike moments, are not easily classified by a small number of parameters. We therefore propose to apply dimensionality reduction and clustering methods to particle distributions in pitch angle and energy space as a new method to distinguish between the different plasma regions. 2D distributions functions in pitch angle and energy are derived from full 3D distributions in velocity space based on the magnetic field direction and the assumption of gyrotopry of electrons.

6.1 Machine Learning Models

In this section, we give a detailed account of the internal operations of each of the unsupervised machine learning algorithms used in our method. In unsupervised learning, algorithms discover the internal representations of the input data without requiring training on example output data. Dimensionality reduction is a specific type of unsupervised learning in which data in high-dimensional space is transformed to a meaningful representation in lower dimensional space. This transformation allows complex datasets, such as 2D pitch angle and energy distributions, to be characterised by analysis techniques (e.g. clustering algorithms) with much more computational efficiency. Our machine learning method utilises four separate algorithms: autoencoders [*Hinton and Salakhutdinov*, 2006], principal component analysis [PCA, *Abdi and Williams*, 2010], mean shift [*Fukunaga and Hostetler*, 1975], and agglomerative clustering [*Lukasová*, 1979]. We obtain the autoencoder algorithm from the Keras library [*Chollet et al.*, 2015], and the PCA, mean shift, and agglomerative clustering algorithms from the scikit-learn library [*Pedregosa et al.*, 2011].

We use the autoencoder to compress the data by a factor of 10 from a high-dimensional representation. We subsequently apply the PCA algorithm to further compress the data to a three-dimensional representation. The PCA algorithm has the advantage of being a lot cheaper computationally than an autoencoder, however the algorithm only captures variations that emerge from linear relationships in the data, while autoencoders also account for non-linear relationships in the dimensionality reduction process [*Bishop*, 1998]. For this reason, we only utilise the PCA algorithm after the data have been compressed via an autoencoder. After compressing the data, we use the mean shift algorithm to inform us of how many populations are present in the data using this three-dimensional representation.

While the mean shift algorithm provides us with this estimate of the requisite number of clusters, the algorithm is ineffective in constraining the shapes of the clusters to determine which population each data-point belongs to. Therefore, we use an agglomerative clustering algorithm to assign each data-point to one of the populations.

6.1.1 Autoencoders

Autoencoders are a particular class of unsupervised neural networks. They are trained to learn compressed representations of data by using a bottleneck layer which maps the input data to a lower dimensional space, and then subsequently reconstructing the original input. By minimising the ‘reconstruction error’, or ‘loss’, the autoencoder is able to retain the most important information in a representative compression and reconstruction of the data. As a result, autoencoders have applications in dimensionality reduction [e.g. *Hinton and Salakhutdinov*, 2006], anomaly detection [e.g. *Kube et al.*, 2019] and noise filtering [e.g. *Chandra and Sharma*, 2014].

During training, an autoencoder runs two functions simultaneously. The first, called an ‘encoder’, maps the input data, \mathbf{x} , to the coded representation in latent space, \mathbf{z} . The second function, called a ‘decoder’, maps the compressed data, \mathbf{z} , to a reconstruction of the input data, $\hat{\mathbf{x}}$. The encoder, $E(\mathbf{x})$, and decoder, $D(\mathbf{z})$, are defined by the following deterministic posteriors:

$$E(\mathbf{x}) = p(\mathbf{z}|\mathbf{x};\theta_E), \tag{6.1}$$

$$D(\mathbf{z}) = p(\hat{\mathbf{x}}|\mathbf{z};\theta_D),$$

where θ_E and θ_D are the trainable parameters of the encoder and decoder respectively.

Figure 6.1 illustrates the standard architecture of an autoencoder.

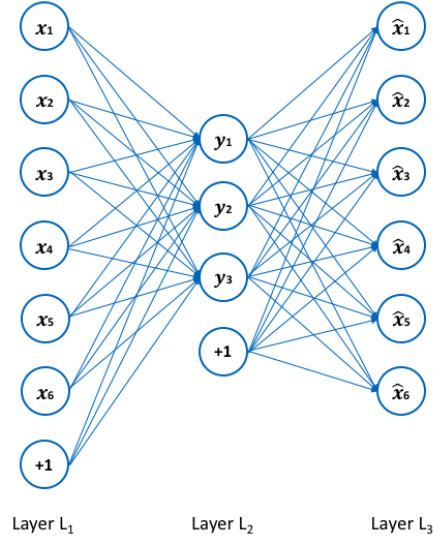


Figure 6.1: The architecture of an autoencoder, adapted from *Sakurada and Yairi* [2014]. Each circle represents a neuron corresponding to a data-point. Layer L₁ represents the input data, layer L₂ the encoded data in latent space, and layer L₃ the reconstructed data. The circles labelled ‘+1’ are known as ‘bias units’, which are parameters that are adjusted during training to improve the performance of the neural network.

In feed-forward neural networks, such as autoencoders, each neuron computes the following sum:

$$y = \sum_i w_i x_i + b, \quad (6.2)$$

where x_i represents the input from the previous layer, w_i denotes the weights associated with the connections between neurons in different layers, and b denotes the bias term associated with each layer (represented by the circles labelled ‘+1’ in figure 6.1). The number of neurons in each layer defines the dimension of the data representation in that layer. The output of each neuron, $f(y)$, is called the activation function. ReLU [Rectified Linear Unit, *Hahnloser et al.*, 2000] is the most commonly used activation function due to its low compu-

tational cost [Agarap, 2018]. The function is described as:

$$f(y) = \max(0, y). \quad (6.3)$$

The sigmoid activation function [Chandra and Singh, 2004] is also commonly used. It is defined by:

$$f(y) = \frac{1}{1 + e^{-y}}, \quad (6.4)$$

where y is defined in Equation (6.2). Analysis of the use of various activation functions in the remit of plasma physics are given by Kube *et al.* [2019].

In order to improve the representation of the compressed data in layer L_2 and minimise the discrepancy between the input and reconstruction layer, the autoencoder adjusts the weights and biases by minimising a loss function through an optimiser (described below). The binary cross-entropy loss function [de Boer *et al.*, 2005] is typically used when the input data, \mathbf{x} , are normalised to values between 0 and 1. The loss value, c , increases as the reconstruction data, $\hat{\mathbf{x}}$, diverge from the input data. The loss function is defined as:

$$c = -[\mathbf{x} \ln(\hat{\mathbf{x}}) + (1 - \mathbf{x}) \ln(1 - \hat{\mathbf{x}})]. \quad (6.5)$$

An overview of various loss functions is provided by Janocha and Czarnecki [2017]. Optimisers are used to ensure the autoencoder converges quickly to a minimum loss value by finding the optimum value of the weight, w_i , of each neuron. This is achieved by running multiple iterations with different weight values, known as gradient descent [Ruder, 2016].

The weights are adjusted in each iteration, t , according to:

$$w_t = w_{t-1} - \alpha \frac{\partial c}{\partial w}, \quad (6.6)$$

where $\partial c / \partial w$ is the gradient, which is a partial derivative of the loss value with respect to the weight. The learning rate, α , updates all the weights simultaneously with respect

to the gradient descent. This learning rate is randomly initialised between 0 and 1 by the algorithm. A low learning rate results in a slower convergence to the global minimum loss value. However a too high value for the learning rate impedes the gradient descent (Equation 6.6) from converging on the optimum weights. The Adadelata optimiser [Zeiler, 2012] is commonly used due to its rapid convergence to the minimum loss value and its ability to adapt the learning rate depending on each parameter. The optimiser updates each parameter, θ , according to:

$$\Delta\theta_t = -\frac{\text{RMS}[\Delta\theta]_{t-1}}{\text{RMS}[g]_t}g_t, \quad (6.7)$$

where $\Delta\theta_t$ is the parameter update at the t -th iteration, g_t is the gradient of the parameters at the t -th iteration, and RMS is the root mean square. The parameter θ represents a combination of both the weights w and biases b . An overview of the various optimisers is provided by *Khandelwal* [2019].

6.1.2 Principal Component Analysis

Principal component analysis is a statistical procedure that, as well as autoencoders, also reduces the dimensionality of input data. The algorithm achieves this by transforming the input data from a large number of correlated variables to a smaller number of uncorrelated variables, known as principal components. These principal components account for most of the variation in the original input data, making them a useful tool in feature extraction.

Before the procedure, the original data, \mathbf{X}_0 , are represented by a $(n \times Q)$ matrix, where n is the number of observations and Q is the number of variables (also called dimensions). In the first step, the algorithm scales and centres the data:

$$\mathbf{X} = (\mathbf{X}_0 - \bar{\mathbf{X}}_0)\mathbf{D}^{-1}, \quad (6.8)$$

where $\bar{\mathbf{X}}_0$ contains the means of each of the variables, and \mathbf{D} is a diagonal matrix that contains the scaling coefficient of each variable. Typically, $D_{ii} = \sigma_i$ where σ_i is the standard deviation of variable with index i [Peerenboom *et al.*, 2015]. The algorithm then uses \mathbf{X} to calculate the covariance matrix:

$$\mathbf{C}_\mathbf{X} = \frac{1}{n-1} \mathbf{X}^T \mathbf{X}, \quad (6.9)$$

which measures the correlation between the different variables. The principal components are calculated as the eigenvectors, \mathbf{A} , of the covariance matrix:

$$\mathbf{C}_\mathbf{X} = \mathbf{A} \mathbf{L} \mathbf{A}^T, \quad (6.10)$$

where \mathbf{L} is a diagonal matrix containing the eigenvalues associated with \mathbf{A} . These principal components are ordered in decreasing order, whereby the first principal components account for most of the variation in the input data. These input data are finally projected into the principal component space according to:

$$\mathbf{Z} = \mathbf{X} \mathbf{A}, \quad (6.11)$$

where \mathbf{Z} represents the output data containing the principal component scores. The dimensionality of these output data are determined by the number of principal components used.

6.1.3 Mean Shift

The mean shift algorithm is a non-parametric clustering technique that is used for locating the maxima of a density function in a sample space. The algorithm aims to discover the number of clusters within a dataset, meaning no prior knowledge of the number of clusters is necessary.

For a dataset containing n data-points \mathbf{x}_i , the algorithm starts finding each maximum of the dataset's density function by randomly choosing a data-point to be the mean of the distribution, \mathbf{x} . The algorithm then uses a kernel function, K , to determine the weights of the nearby data-points for re-estimating the mean. The variable h is the width of the kernel window. Typically, a Gaussian kernel, k , is used:

$$K\left(\frac{\mathbf{x}-\mathbf{x}_i}{h}\right) = c_k k\left(\left\|\frac{\mathbf{x}-\mathbf{x}_i}{h}\right\|^2\right) = \exp\left(-c_k \left\|\frac{\mathbf{x}-\mathbf{x}_i}{h}\right\|^2\right), \quad (6.12)$$

where c_k is the normalising constant. With the kernel function, the multivariate kernel density estimator is obtained:

$$f(\mathbf{x}) = \frac{1}{nh^d} \sum_{i=1}^n K\left(\frac{\mathbf{x}-\mathbf{x}_i}{h}\right), \quad (6.13)$$

where d is the dimensionality of the dataset. The gradient of the density estimator is then:

$$\begin{aligned} \nabla f(\mathbf{x}) &= \frac{2c_k}{nh^{d+2}} \sum_{i=1}^n (\mathbf{x}_i - \mathbf{x}) g\left(\left\|\frac{\mathbf{x}-\mathbf{x}_i}{h}\right\|^2\right) \\ &= \frac{2c_k}{nh^{d+2}} \left[\sum_{i=1}^n g\left(\left\|\frac{\mathbf{x}-\mathbf{x}_i}{h}\right\|^2\right) \right] \mathbf{m}_h(\mathbf{x}), \end{aligned} \quad (6.14)$$

where $g(\mathbf{x}) = -k'(\mathbf{x})$. The first term is proportional to the density estimate at \mathbf{x} , and the second term, $\mathbf{m}_h(\mathbf{x})$, is:

$$\mathbf{m}_h(\mathbf{x}) = \frac{\sum_{i=1}^n \mathbf{x}_i g\left(\left\|\frac{\mathbf{x}-\mathbf{x}_i}{h}\right\|^2\right)}{\sum_{i=1}^n g\left(\left\|\frac{\mathbf{x}-\mathbf{x}_i}{h}\right\|^2\right)} - \mathbf{x}, \quad (6.15)$$

which is the mean shift vector and points towards the direction of the maximum increase in density. The mean shift algorithm therefore iterates between calculating the mean shift vector, $\mathbf{m}_h(\mathbf{x}^t)$, and translating the kernel window:

$$\mathbf{x}^{t+1} = \mathbf{x}^t + \mathbf{m}_h(\mathbf{x}^t), \quad (6.16)$$

where t is the iteration step. Once the window has converged to a point in feature space where the density function gradient is zero, the algorithm carries out the same procedure

with a new window until all data-points have been assigned to a maximum in the density function.

6.1.4 Agglomerative Clustering

Agglomerative clustering is a type of hierarchical clustering that uses a ‘bottom-up’ approach, whereby each data-point is first assigned a different cluster. Then pairs of similar clusters are merged until the specified number of clusters has been reached. During each recursive step, the agglomerative clustering algorithm combines clusters typically using Ward’s criterion [Ward, 1963], which finds pairs of clusters that lead to the smallest increase in the total intra-cluster variance after merging. The increase is measured by a squared Euclidean distance metric:

$$d_{ij} = d(C_i, C_j) = \|C_i - C_j\|^2, \quad (6.17)$$

where C_i represents a cluster with index i . The algorithm implements Ward’s criterion using the Lance-Williams formula [Lance and Williams, 1967]:

$$\begin{aligned} d(C_i \cup C_j, C_k) = & \frac{n_i + n_k}{n_i + n_j + n_k} d(C_i, C_k) \\ & + \frac{n_j + n_k}{n_i + n_j + n_k} d(C_j, C_k) - \frac{n_k}{n_i + n_j + n_k} d(C_i, C_j), \end{aligned} \quad (6.18)$$

where C_i , C_j , and C_k are disjoint clusters with sizes n_i , n_j , and n_k , and $d(C_i \cup C_j, C_k)$ is the squared Euclidean distance between the new cluster $C_i \cup C_j$ and C_k . The clustering algorithm uses Equation (6.18) to find the optimal pair of clusters to merge.

6.2 Method and Application

In this section, we detail the steps required to classify different regions within a space plasma environment using machine learning techniques. As an example, we classify Cluster-

PEACE [Plasma Electron And Current Experiment, *Johnstone et al.*, 1997; *Fazakerley et al.*, 2010] data [*Laakso et al.*, 2010] from the Earth’s magnetotail to showcase our method, as this allows us to compare to the Cluster-ECLAT [*Boakes et al.*, 2014] database for evaluation. The same method, however, can be applied to any plasma regime where energy and pitch angle measurements are available. Our steps are as follows:

1. **Data preparation:** We obtain the Cluster-PEACE data from different magnetotail regions based on the Cluster-ECLAT database, and prepare the data for testing.
2. **Reducing dimensionality:** We build our autoencoder and use the encoder part to reduce the dimensionality of each pitch angle and energy distribution by a factor of 10. We use a PCA algorithm to further compress each distribution to a set of coordinates in 3D space.
3. **Clustering:** We apply the mean-shift algorithm to determine how many clusters exist within the compressed magnetotail electron data, and use an agglomerative clustering algorithm to separate the compressed dataset into this number of clusters. This allows us to determine how many plasma regimes exist within the overall dataset.
4. **Evaluation:** We estimate the probabilities of the agglomerative clustering labels and compare our clustering results to the original ECLAT labels in order to evaluate our method.

6.2.1 Data Preparation

We prepare PEACE instrument data from the Cluster mission’s C4 spacecraft [*Escoubet et al.*, 2001] to test and present our method. The Cluster mission comprises of four spacecraft, each spinning at a rate of 0.25 s^{-1} . The PEACE data have a 4 s time resolution and are

constructed from two instantaneous pitch angle distribution measurements per spin. Each of our distributions is a two-dimensional differential energy flux product containing twelve 15° wide pitch angle bins and 26 energy bins, spaced logarithmically between 93 eV and 24 keV. The dimensionality of each distribution is 312 (12×26). We normalise the differential energy flux linearly between 0 and 1 based on the maximum flux value in the dataset. An example of an individual differential energy flux distribution used in our analysis is shown in figure 6.2. We correct for spacecraft potential with measurements from the Cluster-EFW instrument [Gustafsson *et al.*, 2001] and corrections (19% increase) according to the results of Cully *et al.* [2007].

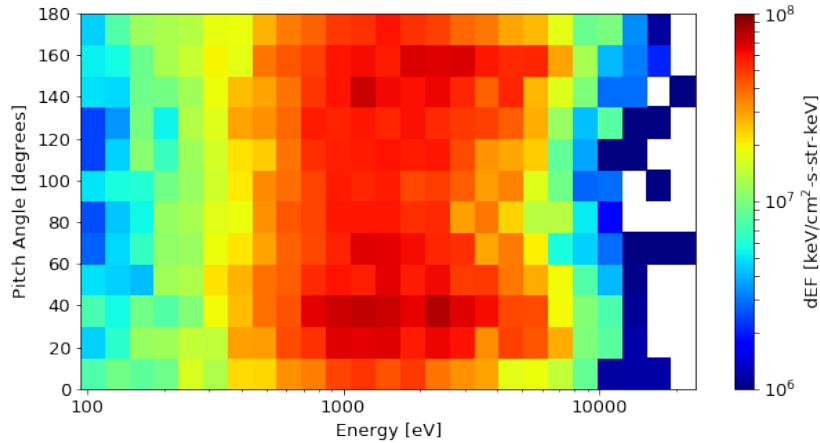


Figure 6.2: An example two-dimensional electron differential energy flux distribution, as a function of pitch angle (degrees) and energy (eV), measured by the Cluster-PEACE instrument in the magnetotail across a 4 second window (09:51:23-09:51:27 on 13/10/2003).

The ECLAT dataset consists of a detailed list of plasma regions encountered by each of the four Cluster spacecraft in the nightside magnetosphere. The dataset is available from July to October during the years 2001-2009. Using plasma and magnetic field moments from the PEACE, CIS [Rème *et al.*, 2001] and FGM [Balogh *et al.*, 1997] instruments, the

dataset provides a list of (inner and outer) plasma sheet, boundary layer, and lobe times. These regions are identified based on the plasma β , the magnetic field measurements, and the current density vectors. A comprehensive account of the ECLAT identification routine for each plasma region is provided by *Boakes et al.* [2014]. To ensure that we test our method on a large number of data from each of the magnetotail regions (>50 000 samples), we obtain PEACE data from times when the C4 spacecraft has spent at least 1 hour in each region, according to ECLAT.

6.2.2 Reducing Dimensionality

After preparing the dataset to include a series of >50 000 time intervals, each with its associated 2D pitch angle and energy distributions (e.g. figure 6.2), the first step towards reducing the dataset’s dimensionality is to build a suitable autoencoder (described in Section 6.1.1). We construct our autoencoder using the Keras library. This step requires defining the number of neurons in each layer. The input and reconstruction layer should have the same number, which is equal to the dimensionality of the original dataset (312 for each time interval in this example). The middle encoded layer typically contains a compressed representation of the data that is by a factor of 10 smaller than the input data [*Hinton and Salakhutdinov*, 2006]. We therefore specify our encoded layer to contain 32 neurons. The next step involves specifying the activation function for the neurons in the first and middle layers. We use the standard ReLU activation function [*Hahnioser et al.*, 2000] in the encoder part of our autoencoder and the sigmoid activation function [*Chandra and Singh*, 2004] in the decoder part, as this function is used to normalise the output between 0 and 1.

The next step defines which loss function and optimiser the autoencoder uses in order to representatively compress and reconstruct the input data. As we use normalised output

data, we choose the standard binary cross-entropy loss function [de Boer et al., 2005]. In terms of the optimiser, we utilise the Adadelata optimiser [Zeiler, 2012] due to its speed and versatility. All of the activation functions, loss functions, and optimisers are available in the Keras library.

In the next step, we set the hyperparameters used for training the autoencoder. These hyperparameters include: the number of epochs, the batch size, and the validation split ratio. The number of epochs represents the number of training iterations undergone by the autoencoder, with the weights and biases updated at each iteration. The batch size defines the number of samples that are propagated through the network at each iteration. It is equal to 2^n , where n is a positive integer. The batch size (256 in our case) is ideally set as close to the dimensionality of the input data as possible. The validation split ratio determines the percentage of the input data that should remain ‘unseen’ by the autoencoder in order to verify that the algorithm is not overfitting the remaining training data. We set the validation split ratio to 1/12, which is commonly used for large datasets [Guyon, 1997]. At each iteration, a training loss value and a validation loss value are produced, which are determined by the binary cross-entropy loss function. Both of these values converge to their minima after a certain number of iterations, at which point the autoencoder cannot be optimised to the input data any further. Loss values <0.01 are typically considered ideal [Le et al., 2018].

After retrieving the compressed representation of the input data from the encoding layer (with a dimensionality of 32 in our case), we apply a PCA algorithm (see Section 6.1.2) to the compressed data to reduce the dimensionality to 3. We obtain the PCA algorithm from the scikit-learn library. We set the output dimensionality of the PCA algorithm to 3 as

the following clustering algorithms used in this method are computationally expensive and their performance scales poorly with increasing dimensionality [Comaniciu and Meer, 2002; Lukasová, 1979]. Setting the dimensionality to 3 has the added benefit that the clusters can be visualised.

6.2.3 Clustering

Once the dimensionality reduction stage has taken place and each pitch angle and energy distribution is represented by 3 PCA values, we use clustering algorithms to separate the dataset into the different particle populations. To first determine how many populations exist within the dataset (8 in our case), we apply a mean shift clustering algorithm (see Section 6.1.3) to the data to find the number of maxima, n_c , in the distribution of data-points. We obtain the mean shift algorithm from the scikit-learn library. We set the bandwidth, represented by h in Equation (6.15), to 1, which we find optimises the time taken for the algorithm to converge on the maxima in the density distribution.

After determining the number of clusters in the dataset, we use an agglomerative clustering algorithm (see Section 6.1.4) to assign each data-point to one of the n_c clusters. We obtain the agglomerative clustering algorithm from the scikit-learn library and instantiate the algorithm by specifying the number of clusters, n_c , before applying it to the compressed dataset. Assigning several clusters to a large dataset with 3 dimensions is a computationally expensive task, however we find the agglomerative clustering algorithm converges relatively quickly in comparison to other clustering algorithms. A further advantage of the hierarchical clustering procedure, used in the agglomerative clustering algorithm, is that data-points belonging to a single non-spherical structure in the 3-dimensional parameter space are not incorrectly separated into different clusters, unlike the more widely used K-

means algorithm [Arthur, 2007].

Figure 6.3 contains a flow diagram detailing our method.

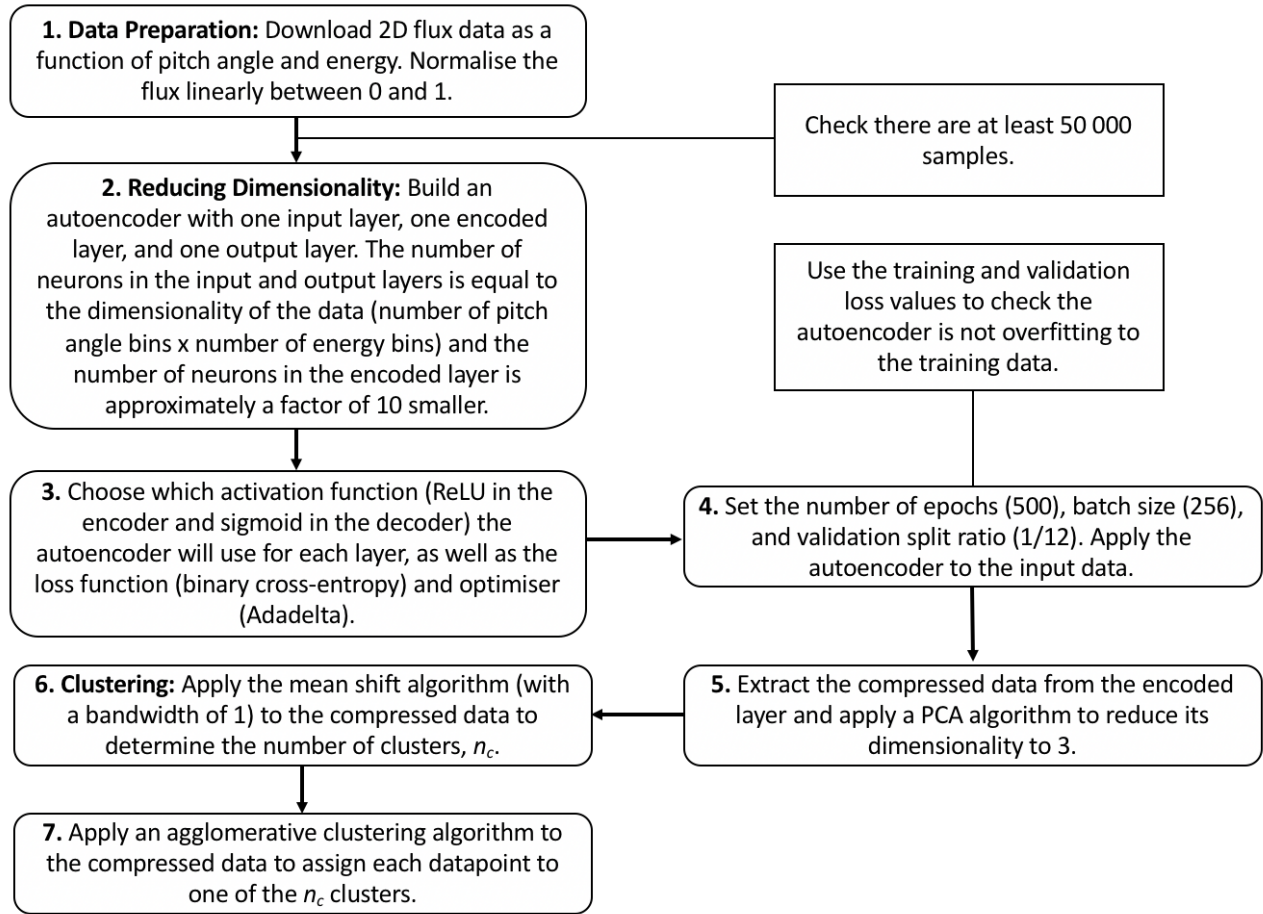


Figure 6.3: Flow diagram illustrating the steps we take to reduce the dimensionality of the dataset and subsequently apply clustering algorithms to characterise the different populations. Our choices for the functions and input parameters necessary to train the autoencoder are shown in brackets in steps 3 and 4.

6.3 Evaluation

Figure 6.4 shows the training and validation loss values associated with each iteration during the training of our autoencoder. We use this graph to check if the autoencoder is overfitting to the training data, which is evident if the training loss starts to decrease more rapidly than the validation loss. In this case, our autoencoder is not overfitting at any iteration during training. Figure 6.4 shows that both the loss values start to rapidly level off in less than 100 epochs. Both loss values, however, continue to decrease, with the training loss value converging to 0.0743 after 444 iterations, and the validation loss value converging to 0.0140 after 485 iterations. We therefore set the number of epochs to 500. As both loss values are lower than 0.01, we conclude the autoencoder is accurately reconstructing both sets of input data, assuring us that the encoded data with a lower dimensionality is representative of the original 2D distribution functions. The lower validation loss than training loss in figure 6.4 indicates the presence of anomalous data in the training set that is not represented in the validation set. We discuss this anomalous data later in this section.

Figure 6.5 shows the result of applying the agglomerative clustering algorithm to the compressed magnetotail electron data after the implementation of the autoencoder and PCA algorithms. The 3-dimensional representation shows that the clustering algorithm is able to assign data-points of varying PCA values to the same cluster if they belong to the same complex non-spherical structure, e.g. clusters 0, 4, and 6. The clustering algorithm is able to form clear boundaries between clusters with adjacent PCA values, e.g. between clusters 0, 1, and 7, with no mixing of cluster labels on either side of the boundaries. The clustering algorithm locates the boundaries by finding areas with a low density of data-points in comparison to the centres of the clusters.

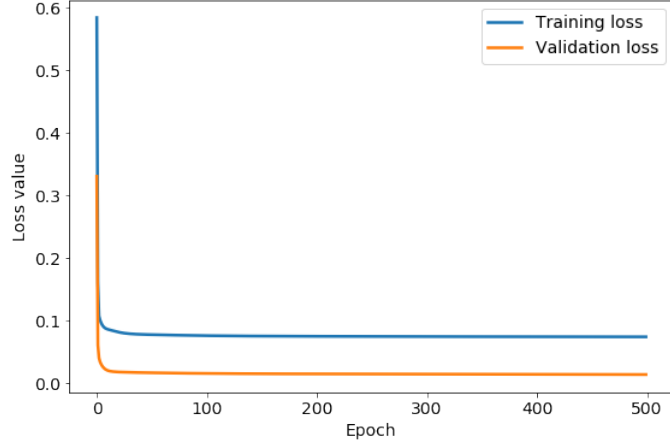


Figure 6.4: The evolution of the training loss value and validation loss value as the autoencoder iterates through 500 steps (epochs).

Figure 6.6 shows the results of averaging the 2D differential energy flux distributions in pitch angle and energy space for each of the 8 clusters. Using moments data collected by the PEACE, FGM, and CIS instruments, we compare the proton plasma β s, electron densities and temperatures, and magnetic field strengths to the average 2D distribution of each cluster. This process allows us to verify the consistency of the clustering method and provide general region classifications in order to make comparisons with the ECLAT labels. Our classifications (shown in the captions below each sub-figure) are produced with the aid of previous analyses of electron pitch angle distributions [e.g. *Walsh et al.*, 2011; *Artemyev et al.*, 2014] and the plasma and magnetic field parameters [e.g. *Lui*, 1987; *Artemyev et al.*, 2014] in the magnetotail.

The individual sub-figures in figure 6.6 display large differences in the average electron 2D pitch angle and energy distributions. Each average distribution differs by either: the energy of the peak flux, the peak value of the flux, or the amount of pitch angle anisotropy, i.e. the difference in flux between the parallel and perpendicular magnetic field direction. The

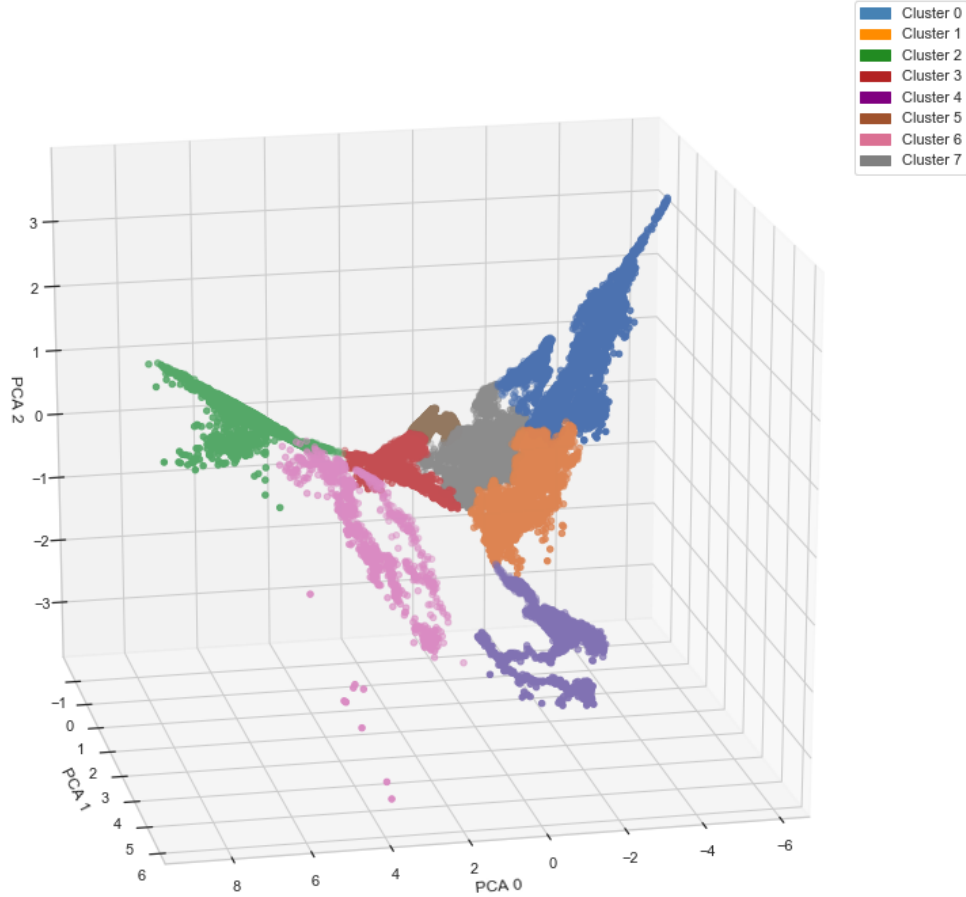
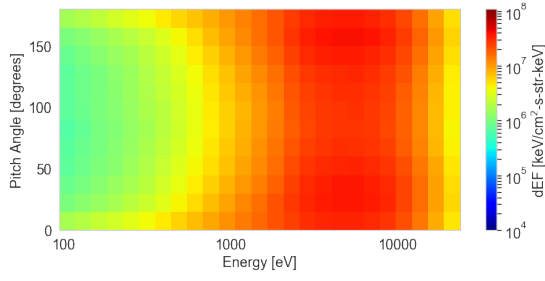


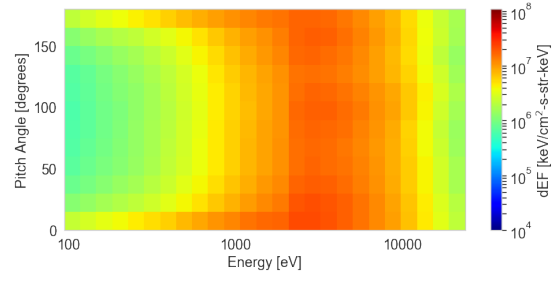
Figure 6.5: Three-dimensional representation of the magnetotail data after undergoing dimensionality reduction via an autoencoder and PCA algorithm. The colours represent the clustering results from the agglomerative clustering algorithm.

lack of identical average distributions amongst the clusters shows the mean shift algorithm has not overestimated the number of clusters. By observing the individual 2D distributions within each cluster, we see a distinct lack of intra-cluster variance, showing the mean shift algorithm does not underestimate the number of clusters.

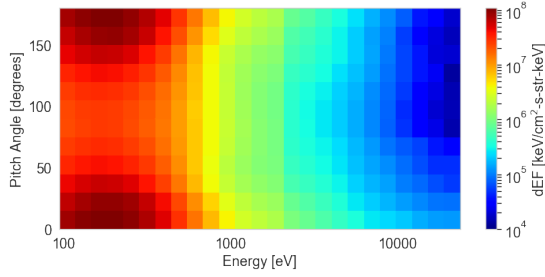
A limitation of using the agglomerative clustering algorithm is that outliers or anomalous data are not differentiated from the main clusters. Clustering a sizeable number of outliers with the main populations can lead to ambiguity in the defining characteristics of



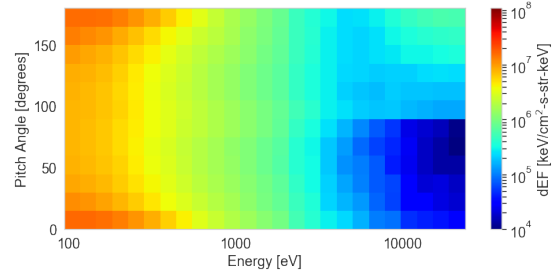
(a) Cluster 0 - PS a



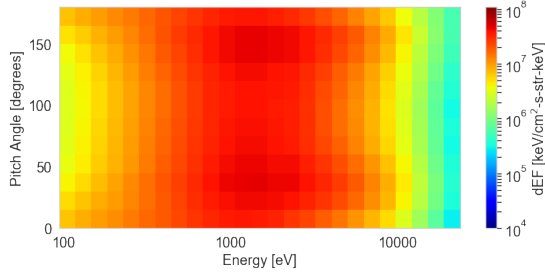
(b) Cluster 1 - PS b



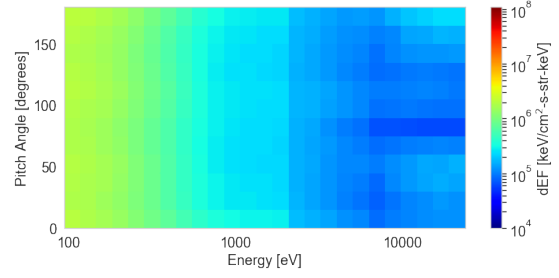
(c) Cluster 2 - PS c



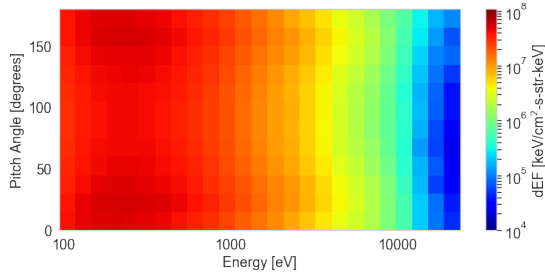
(d) Cluster 3 - PSBL



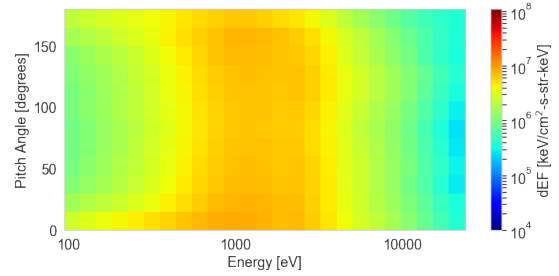
(e) Cluster 4 - PS d



(f) Cluster 5 - Lobes



(g) Cluster 6 - PS e



(h) Cluster 7 - PS f

Figure 6.6: Average electron differential energy flux distributions as a function of pitch angle and energy for each of the eight clusters. Each cluster is assigned a magnetotail region based on our interpretation of their plasma and magnetic field parameters.

each population, reducing the robustness of our method. In our case, figure 6.5 shows only 9 data points, within cluster 6, that are disconnected from the main structure of cluster 6 due to their distinct PCA values. We observe similar phenomenon to a lesser extent with cluster 2. To counteract this issue, we perform an outlier detection procedure using the reconstructed output of the autoencoder. By calculating the mean square error (MSE) between each input data-point and its reconstructed output, we isolate outliers in the dataset from the agglomerative clustering analysis based on their large MSE values, in comparison to 99.95% of the data-points. During training, the autoencoder learns the latent space representation that defines the key characteristics of the bulk populations present in the dataset. The most relevant features of an anomalous particle distribution are not present in this subspace, resulting in a large mean square error between the reconstructed data, which lacks these important features, and the original data. This technique effectively identifies the 9 obvious outliers observable by eye in figure 6.5, along with 6 from cluster 2 and 5 from cluster 1.

We use Gaussian mixture models [GMMs, *McLachlan and Peel*, 2000] to establish the probabilities of each of the data-points belonging to the clusters they have been assigned to by the agglomerative clustering algorithm, providing useful information on the uncertainty associated with our region classification method. We obtain the GMM from the scikit-learn library. For each data-point, x_i , a GMM fits a normal distribution, \mathcal{N} , to each cluster and computes the sum of probabilities as:

$$p(x_i) = \sum_{j=1}^k \phi_j \mathcal{N}(x_i; \mu_j, \tau_j) = 1, \quad (6.19)$$

where μ_j and τ_j are the mean and covariance of the normal distribution belonging to cluster j , and ϕ_j is the mixing coefficient which represents the weight of Gaussian j and is calcu-

lated by the Expectation-Maximisation (EM) algorithm [Dempster *et al.*, 1977]. A complete description of GMMs and the EM algorithm is provided by Dupuis *et al.* [2020].

Figure 6.7 shows a histogram of the probabilities, calculated by the GMM, associated with each data-point belonging to the cluster it is assigned to by the agglomerative clustering algorithm. More than 92% of the data-points have a probability of over 0.9, and <1% of the data-points have a probability of <0.5. This indicates a high certainty in our clustering method and validates the high precision in our region classifications. Further investigations of the data-points with associated probabilities of <0.5 show that these data-points exist on the boundary between clusters 0 and 1, i.e. two plasma sheet populations that differ by temperature. This illustrates a small limitation in the agglomerative clustering method when distinguishing between relatively similar plasma regimes.

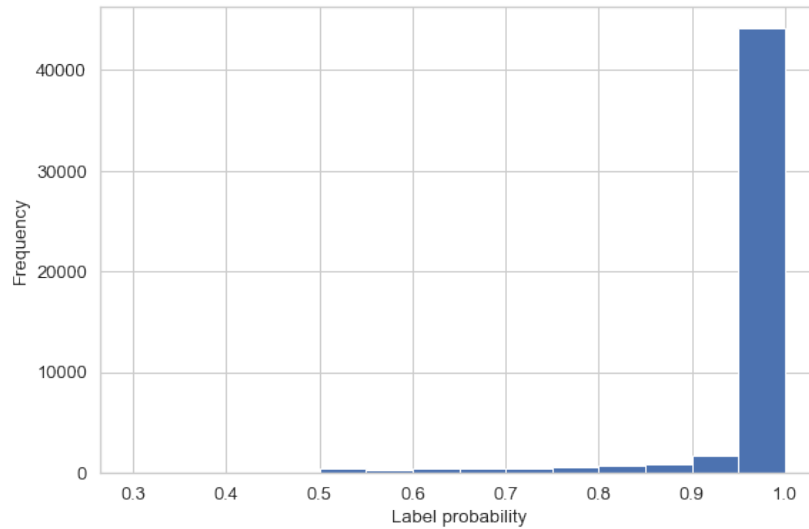


Figure 6.7: Histogram showing the probabilities, generated by GMMs, that the data-points belong to the cluster assigned to them by the agglomerative clustering algorithm.

Table 3 shows the median and upper and lower quartiles of the electron density, electron temperature, magnetic field, and ion plasma β for each of the 8 clusters designated by our

agglomerative clustering algorithm. None of the 8 clusters have comparable median and quartile values across all four of the chosen parameters. Certain pairs of clusters exhibit similarities in the median and quartile values for one or two of the four parameters, e.g. clusters 0 and 4 exhibit similar electron densities and magnetic field strengths, and clusters 3 and 6 exhibit similar magnetic field strengths. However there are large differences in the values of the remaining parameters for these pairs of clusters. These results show that clear differences in the 2D pitch angle and energy distributions (see figure 6.6) can translate into distinctions between certain but not all plasma parameter measurements, providing a strong indicator that full 2D distributions can effectively be used to distinguish between similar particle populations. Regarding the ECLAT classifications, which are based on magnetic field and plasma β measurements, certain pairs of clusters exhibit a similar range of values in both of these measurements, e.g. clusters 0 and 4 and clusters 1 and 7. As the majority of data-points for all of these clusters are considered the same plasma sheet population by ECLAT (see table 4), we conclude that using a limited number of parameters to provide classifications overlooks distinctions between different populations and incorrectly groups them into the same category.

Table 4 shows our comparison between the eight agglomerative clustering (AC) labels and the region names given in the ECLAT database, for the magnetotail data used in our example.

In table 4, there is some disagreement with three of our clusters, namely AC labels 3, 5, and 7, which correspond to the plasma sheet boundary layer, the lobes, and a plasma sheet population respectively. However for each of these clusters, the majority of labels are in agreement with the ECLAT regions (72.4%, 86.8%, and 86.9% for AC clusters 3, 5, and

Table 3: Comparisons of the median, Q2, and upper, Q3, and lower, Q1, quartile values of the electron density n_e , electron temperature T_e , magnetic field $|\mathbf{B}|$, and plasma β associated with each of the 8 clusters. The AC labels 0, 1, 2, 4, 6, and 7 belong to the plasma sheet, according to ECLAT, 3 belongs to the plasma sheet boundary layer, and 5 belongs to the lobes.

AC labels	n_e (cm ⁻³)			T_e (eV)			$ \mathbf{B} $ (nT)			plasma β		
	Q1	Q2	Q3	Q1	Q2	Q3	Q1	Q2	Q3	Q1	Q2	Q3
0	0.21	0.22	0.23	2057.26	2515.28	2913.33	32.45	35.09	37.86	3.54	4.33	5.92
1	0.12	0.14	0.19	1487.67	1838.97	2258.43	10.56	13.65	19.42	15.31	24.54	39.75
2	1.08	1.18	1.30	106.44	114.19	123.33	20.87	22.67	24.25	0.80	0.99	1.17
3	0.21	0.25	0.28	79.21	83.63	93.00	16.64	35.07	39.76	0.28	0.39	0.60
4	0.22	0.28	0.82	783.33	879.77	997.85	24.58	39.10	41.93	1.23	1.52	6.29
5	0.01	0.02	0.03	116.63	170.57	252.85	32.97	41.34	49.00	0.00	0.06	0.27
6	1.29	1.49	1.65	164.41	214.64	269.16	41.65	44.74	46.56	0.30	0.43	0.60
7	0.08	0.10	0.13	669.64	882.30	1217.77	5.42	17.16	25.95	3.69	9.05	128.11

7 respectively). For AC labels 0, 1, 2, 4, and 6, which represent various other populations within the plasma sheet, there is 100% agreement with the ECLAT label 0, which denotes the plasma sheet. By using this method to characterise full electron pitch angle and energy distributions, instead of using the derived moments, we are successfully able to distinguish between multiple populations within what has historically been considered as one region, due to the lack of variation in the plasma moments (see table 3) as well as the similarity in spatial location. Using 2D pitch angle and energy distributions also improves the time resolution of the plasma region classifications, due to a higher cadence in the spacecraft flux and counts data (e.g. 4 s resolution for the PEACE instrument) in comparison to the moments data (e.g. 8 s resolution for CIS moments and 16 s resolution for PEACE moments).

Table 4: Contingency table comparing the agglomerative clustering (AC) labels of the magnetotail electron data to the original ECLAT labels (0 = PS, 1 = PSBL, and 2 = lobes). The AC labels are the same as in table 3.

AC labels	ECLAT labels		
	0	1	2
0	6549	0	0
1	3074	0	0
2	5092	0	0
3	1590	4188	0
4	2097	0	0
5	156	2228	15641
6	1029	0	0
7	7020	1057	0

6.4 Conclusion

We present a novel machine learning method that characterises full particle distributions in order to classify different space plasma regimes. Our method uses autoencoders and subsequently principal component analysis to reduce the dimensionality of the 2D particle distributions to three dimensions. We then apply the mean shift algorithm to discover the number of populations in the dataset, followed by the agglomerative clustering algorithm to assign each data-point to a population.

To illustrate the effectiveness of our method, we apply it to magnetotail electron data and compare our results to previous classifications, i.e. the ECLAT database, that utilises mo-

ments. With our method, we find multiple distinct electron populations within the plasma sheet, which previous studies have identified as one region (table 4). These findings show that key features in particle distributions are not fully characterised by the plasma moments (e.g. table 3), resulting in important distinctions between populations being overlooked. For example, we find two separate cold dense anisotropic populations in the plasma sheet (clusters 2 and 6), which are less abundant than the hotter and more isotropic plasma sheet populations. By using our clustering method to specify an exact list of times when populations like these are observed, we create a more comprehensive picture of their spatial distribution. Inherent time-dependencies may also contribute to our finding of multiple plasma sheet populations. Even in this case, our method is effective in characterising the evolution of particle populations, made possible by the high time resolution of our region classifications.

In a follow up study, we will use this information to link the occurrence of these populations to other high-resolution spacecraft measurements in different plasma regions, in order to understand the physical processes driving changes in the less abundant particle populations. As an example analysis, our high resolution classifications of the observed anisotropic plasma sheet populations could be combined with previous theories on the sources of these populations [e.g. *Walsh et al.*, 2013; *Artemyev et al.*, 2014], to understand the relative contributions of particle outflows from distinct magnetospheric regions, such as the magnetosheath or ionosphere.

Comparisons between this original method and the previous classifications from ECLAT also show specific periods of disagreement (e.g. we classify a small number of ECLAT periods of plasma sheet as the plasma sheet boundary layer). This discrepancy shows that using

the full 2D pitch angle and energy distributions, without requiring prior assumptions about magnetospheric plasma regions, may redefine the classifications of electron populations, along with our understanding of their plasma properties. Possible future modifications to our model could include applying an outlier detection method to eliminate the distributions before training the autoencoder to reduce the dimensionality of anomalous data - thereby altering its network structure for the rest of the dataset. For instances where larger differences between populations are prevalent in both the distributions and magnetic field parameters, then adding a further input to the autoencoder that contains magnetic field data would allow the autoencoder to better characterise the multiple populations.

Our method, which uses open-source and easily accessible machine learning techniques, can be used to better characterise any space plasma regime with sufficient in-situ observations. By not being constrained to a small number of parameters, this method allows for a more complete understanding of the interactions between various thermal and non-thermal populations. With increasingly large datasets being collected by multi-spacecraft missions, such as Cluster [*Escoubet et al.*, 2001] ($>10^9$ full distributions in 20 years) and MMS [Magnetospheric Multiscale Mission, *Sharma and Curtis*, 2005], similar methods would provide a useful tool to reduce the dimensionality of distributions, thereby optimising data retrieval on Earth. Furthermore, combining this method with large-scale survey data, such as NASA/GSFC's OMNI database, would allow users to isolate a specific population or plasma region for analysis of its properties.

7 Direct evidence of magnetic reconnection onset via the tearing instability

This work is presented in Bakrania et al. ‘Direct evidence of magnetic reconnection onset via the tearing instability’. (Under Review in Frontiers in Astronomy and Space Sciences, endorsed for publication by one Reviewer).

Magnetic reconnection is a fundamental mechanism responsible for explosive energy release in space and laboratory plasmas. The onset of reconnection is via a plasma instability that leads to the formation of closed magnetic islands, called the tearing instability. Due to its elusive nature, there is an absence of in-situ spacecraft observations of the tearing instability. Using neural network outlier detection methods, in conjunction with Cluster spacecraft data, we present the first direct observations of the tearing instability and the subsequent evolution of plasma electrons within the Earth’s magnetosphere: a natural plasma laboratory.

7.1 Introduction

Magnetic reconnection is a universal plasma process that changes the topology of the magnetic field and converts magnetic energy into particle kinetic and thermal energy [Birn and Priest, 2007]. This process is responsible for explosive phenomena in laboratory, astrophysical, and space plasmas, such as planetary magnetospheres. The Earth’s nightside magnetosphere, i.e. the magnetotail, provides an accessible medium to directly measure reconnection with in-situ spacecraft. The recent introduction of the MMS mission in particular has enabled reconnection physics at the electron scale to be studied [Burch and Phan,

2016]. For example, distinct regions of electron energisation and mixing have been observed within the diffusion region of a reconnection site [Chen *et al.*, 2016]. Although there are in-situ observations of ongoing magnetic reconnection [Eastwood *et al.*, 2010; Øieroset *et al.*, 2001; Borg *et al.*, 2012; Hwang *et al.*, 2013; Nagai *et al.*, 2001], the question remains what triggers this process that sporadically changes the magnetic topology, as this process has not been directly measured [Galeev and Zelenii, 1976; Pellat *et al.*, 1991].

The tearing instability is the central candidate mechanism that creates conditions required for the onset of reconnection [Coppi *et al.*, 1966; Chen *et al.*, 1997]. In the magnetotail, this instability may occur for sufficiently thin current sheet and small values of the magnetic field normal to the current sheet, and causes quasi-periodic spatial perturbations of the magnetic field and the associated particle distribution functions [Sitnov *et al.*, 2019]. The instability takes place within an externally driven current sheet (current sheet thinning caused by an external factor), which usually occurs during the substorm expansion phase [Bessho and Bhattacharjee, 2014]. The result of magnetic reconnection is a rearrangement of the magnetic field topology threading the thin current sheet [Galeev and Zelenii, 1976], leading to the formation of plasmoids and X-lines [Zanna *et al.*, 2016], as well as heating and acceleration of the plasma along the field lines. Using kinetic models, two-dimensional Particle-In-Cell (PIC) simulations [Bessho and Bhattacharjee, 2014; Pellat *et al.*, 1991] have shown that in Earth’s magnetotail, the electron tearing instability is the most relevant instability for the initiation of reconnection. However, observational signatures of such a process are still lacking.

On the other hand, simulations have found electron distributions that exhibit a strong counter-streaming field-aligned distribution as the tearing mode develops [Furth, 1963;

Markidis et al., 2012; *Zeiler et al.*, 2001; *Buechner and Zelenyi*, 1987], followed by an isotropisation across all pitch angles over 5 minutes [*Buechner and Zelenyi*, 1987]. The counterstreaming electron distributions during the early evolution of tearing correspond with a rapid growth in energy and temperature [*Buechner and Zelenyi*, 1987; *Walker et al.*, 2018]. Following this stage, the perpendicular temperature increases [*Liu et al.*, 2014], driving the onset of magnetic reconnection. Here we hypothesise that these field-aligned distributions and their subsequent evolution can be identified in the magnetotail current sheet in order to locate the tearing instability. We apply a neural network outlier detection method to Cluster spacecraft electron data to identify the location where the tearing mode develops. We verify that the plasma and magnetic field parameters at those locations are consistent with tearing instability by applying the stability criterion derived by *Schindler et al.* [1973]; *Liu et al.* [2014], valid for a collisionless plasma with a finite normal component. It is found that tearing mode events identified via our neural network outlier method are consistent with the tearing instability. Furthermore, data analyses of the subsequent evolution of particles and magnetic fields confirm the typical features found in reconnection simulations. The present work provides strong observational support to theories predicting tearing mode as the onset mechanism for reconnection in the magnetotail.

7.2 Method

7.2.1 Data

We use electron data [*Laakso et al.*, 2010] from the Cluster [*Escoubet et al.*, 2001] mission’s PEACE [*Johnstone et al.*, 1997; *Fazakerley et al.*, 2010] (Plasma Electron And Current Experiment) instrument on all of the four spacecraft to detect signatures of the tearing mode in

the electron distribution functions. Cluster's four spacecraft fly in a tetrahedral formation with a spin period of 4 seconds. We use pitch angle distributions from the PITCH-SPIN data product, which have a 4 s time resolution and are constructed from two instantaneous pitch angle measurements per spin. Each distribution consists of a two-dimensional differential energy flux product with twelve 15° pitch angle bins and 26 logarithmically spaced energy bins ranging from 93 eV to 24 keV. Therefore, each distribution has a dimensionality of 312 (12×26). We correct our PEACE measurements with the method presented by *Cully et al.* [2007] to account for the effect of the spacecraft potential measured by the Cluster-EFW instrument [*Gustafsson et al.*, 2001]. We normalise the value of differential energy flux between 0 and 1, based on the value of maximum flux in the dataset, in order to concentrate on the shape of the distribution rather than the flux value, given that the Earth's magnetotail plasma sheet can vary by 5 orders of magnitude with different conditions [*Artemyev et al.*, 2014].

We use the ECLAT database [*Boakes et al.*, 2014] to isolate relevant times for detecting the tearing instability. The ECLAT database uses data from PEACE, FGM [*Balogh et al.*, 1997], and CIS [*Rème et al.*, 2001] to construct a list of plasma regions encountered by the four Cluster spacecraft in the magnetotail from July to October, during the years 2001-2009. The ECLAT database associates the measurement intervals with three magnetotail regions: the plasma sheet, the plasma sheet boundary layer, and the lobes [*Hughes*, 1995], which are defined by their plasma and magnetic field characteristics. The database also lists times of current sheet crossings at the centre of the plasma sheet. We obtain PEACE data from times when the spacecraft has spent at least 30 minutes in the plasma sheet, as this region is most likely to undergo magnetotail reconnection [*Angelopoulos et al.*, 2008].

7.2.2 Autoencoder

We employ an autoencoder [Hinton and Salakhutdinov, 2006] to detect anomalous distributions from the entire set of plasma sheet data [Bakrania et al., 2020]. Autoencoders are a class of unsupervised neural networks which are trained to learn compressed representations of data. These compressed representations are achieved via a ‘bottleneck’ layer which maps (encodes) the input data to a lower-dimensional latent space, and subsequently reconstructs (decodes) the original input from this latent space. By minimising the reconstruction error, or ‘loss’ between the input and output data, the autoencoder retains the most important characteristics in the compressed version of the data. For an anomalous distribution, its most important features are not present in the latent space, which results in a large reconstruction error between the input and output data. Autoencoders are therefore an effective method for isolating outliers [Kube et al., 2019]. Figure 6.1 illustrates the typical architecture of an autoencoder [Sakurada and Yairi, 2014]. A detailed description of autoencoders is provided by Hinton and Salakhutdinov [Hinton and Salakhutdinov, 2006].

We construct our autoencoder using the Keras library [Chollet et al., 2015]. Building an autoencoder requires the definition of the number of neurons in each layer. The number of neurons in the input and output layers equals the dimensionality of each distribution: 312 in our case. We set the number of neurons in the bottleneck layer at 32, representing a compression factor of 9.75. Each layer uses an activation function to pass on signals to the next layer [Kube et al., 2019]. For the encoder part, we use the ReLU activation function [Hahnloser et al., 2000], and for the decoder part, we use the sigmoid activation function [Chandra and Singh, 2004], which normalises the output between 0 and 1. We then define the loss function and optimiser, which the autoencoder uses to representatively

compress and reconstruct the input data. We choose the binary cross-entropy loss function [de Boer et al., 2005] and the Adadelta [Zeiler, 2012] optimiser. All activation functions, loss functions, and optimisers are available in the Keras library. We set the number of epochs to 500 and the batch size, i.e. the number of distributions propagated through the network at each epoch, to 256. The validation split ratio defines the ratio of distributions that remain ‘unseen’ to the autoencoder in order to avoid overfitting. We set this to 1/12. At each epoch a training loss and validation loss value are produced, which both converge to <0.1 after training, indicating that the autoencoder accurately reconstructs the majority of the dataset.

To isolate the field-aligned tearing distributions from the dataset, we calculate the mean square error (MSE) between each original and reconstructed distribution. We set the MSE threshold to 99.5%, which locates all distributions which have a MSE in the upper 0.5% of the dataset. We subsequently visually inspect each anomalous distribution to find signatures of the tearing instability based on the flux anisotropy, as outlined in section 7.1. We then obtain a list of outlier measurements to be studied further.

7.3 Coordinate system

For the intervals which contain a current sheet crossing, we transform the coordinate system from the GSM coordinate system to the local (LMN) coordinate system. This coordinate system provides a more accurate representation of the magnetic field vectors as it takes into account the current sheet tilt. We obtain the local coordinate system from a minimum variance analysis [Sonnerup and Scheible, 1998] of the magnetic field data during a short interval before each instance of tearing. In this coordinate system, L is in the direction of the anti-parallel magnetic field, M is in the direction of the current, and N is in the normal

direction to the current sheet. Our algorithm identifies an event on 07/08/2004. For this event, we obtain this coordinate system from the minimum variance analysis of the magnetic field data from 23:26:30 UT to 23:27:30 UT. The vector representations of the local magnetic coordinates are: $L = (0.9859, -0.1110, -0.1253)$, $M = (0.1491, 0.9221, 0.3570)$ and $N = (0.0759, -0.3707, 0.9257)$ in GSM coordinates. We also account for a small out-of-plane (M -direction) guide field of +1.06 nT during this event.

7.4 Tearing mode stability criteria

We determine whether an outlier event is tearing unstable based on the instability criteria set out by *Schindler et al.* [1973], *Liu et al.* [2014], and in other studies (see below). Simulations [*Bessho and Bhattacharjee*, 2014] show that the electron tearing instability only occurs when the magnitude of B_N is small (<10 nT), in agreement with other studies [*Galeev and Zelenii*, 1976; *Pellat et al.*, 1991]. *Schindler et al.* [1973] predicts that B_N must be positive for the instability to arise. Both theory [*Coppi et al.*, 1966; *Zanna et al.*, 2016; *Schindler et al.*, 1973] and simulations [*Bessho and Bhattacharjee*, 2014], show that current sheet thinning is especially important for the tearing mode instability.

By applying the energy principle to two-dimensional Vlasov equilibria, *Schindler et al.* [1973] derived a stability criterion that predicts instability when $k\rho_e \geq 1$, where k is the wavenumber of the perturbation and ρ_e the electron gyroradius associated with the normal magnetic field component. This criterion can be equivalently written as [*Liu et al.*, 2014]:

$$b \frac{L_N}{d_i} < \frac{f}{\zeta} \sqrt{\frac{m_e T_e}{m_i T}}, \quad (7.1)$$

where $b = B_n/B_0$, B_0 is the lobe magnetic field, L_N is the half-current sheet height, d_i is the ion inertial length, $f = k_L L_N$, ζ is a parameter which we set to 1, $T = T_e + T_i$, and T_e and T_i

are the electron and ion temperatures.

After identifying possible candidate measurement points for tearing, we check if each candidate complies with all three of the following instability criteria:

1. The criterion in equation 7.1, which we determine by comparing the corresponding magnetic field measurements (GSM coordinate system) from the FGM instrument, and electron temperature measurements from the PEACE instrument.
2. The presence of a rapid growth in temperature, in conjunction with an isotropisation, shortly after the anomalous distribution is observed, in line with the results from PIC simulations described in section 7.1 [*Buechner and Zelenyi, 1987; Liu et al., 2014; Walker et al., 2018*].

7.5 Hall quadrupole field

To link our events to magnetic reconnection, we look for evidence of a Hall quadrupole magnetic field and flow reversals. The Hall quadrupole field shows that B_M exhibits a correlation with v_L above the current sheet (Northern Hemisphere), and an anti-correlation with v_L below the current sheet (Southern Hemisphere). During the intervals in which we observe flow reversals, a small out-of-plane (M -direction) guide magnetic field [*Denton et al., 2016*] may be present which needs to be accounted for. Averaging B_M prior to the flow reversal informs us of the magnitude of this guide field. We therefore correct for this by shifting all B_M values in this interval until the average B_M vanishes.

7.6 Results

7.6.1 Tearing mode stability check

In order to find signatures of the tearing instability, we apply our neural network outlier detection method [Bakrania *et al.*, 2020] to Cluster-PEACE data from the magnetotail plasma sheet (see section 7.2.2). From the collection of outlier events, we identify 15 separate time intervals, between 2001 and 2009, (see Table 5) that all fulfill the criteria for field-aligned distributions described in section 7.1, as well as the magnetic field criteria (see section 7.4). We refer to the field-aligned distributions as tearing distributions. Figure 7.1 shows the results of our stability analysis for all events. We create the plot by inputting measurements during each event into equation (7.1) [Liu *et al.*, 2014], with the only unknown being f . The figure 7.1 confirms that all events adhere to the instability criterion in equation (7.1). Using multi-spacecraft measurements, we calculate for this figure the magnetic field, current sheet height (see below), ion internal length, mass ratio and temperature ratio for each event. As the parameter f relates to the wavenumber, we provide different estimates for f based on the analysis by Liu *et al.* [2014]. For a realistic mass ratio (m_e/m_i) of 1/1836, Liu *et al.* [2014] predict that $f = 0.91$. Figure 7.1 shows that all events are below the $f = 0.91$ line and therefore adhere to the instability criterion.

7.6.2 Case study

In this section we discuss the event which occurred on 07/08/2004. We discuss the rest of the events in section 7.6.3. In this case study event, Cluster passed from North to South through the magnetotail, crossing the current sheet at 23:27:13 UT before encountering an electron population that shows signatures of the tearing mode instability, followed by

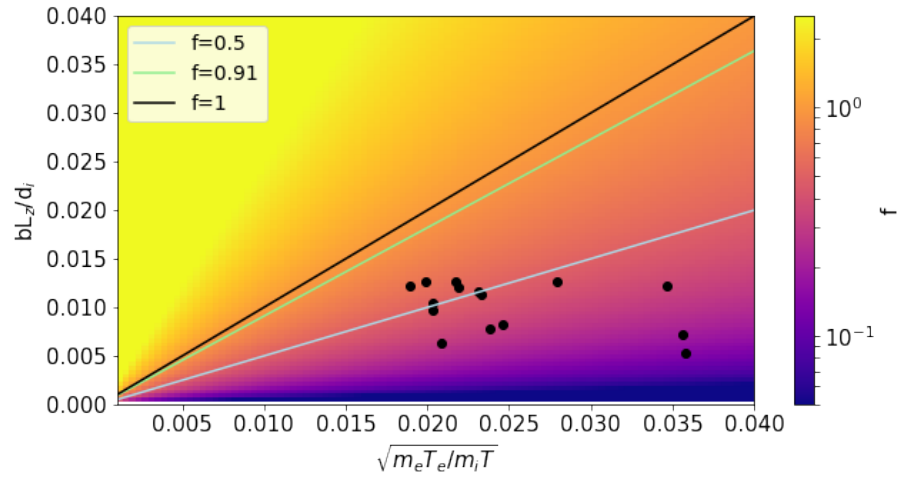


Figure 7.1: Verification of the tearing instability. The black dots represent each of the 15 events identified by our neural network method. The axes correspond to the terms on the left and right hand side of equation (7.1), while the background colour represents the parameter f in equation (7.1). The straight lines represent the boundaries for different values of f , below which the plasma is tearing unstable [Liu *et al.*, 2014].

a crossing through a diffusion region. The first outlier distribution, or tearing distribution, was detected by the C4 spacecraft at 23:29:05 UT, when the spacecraft was below the current sheet in the position $(-16.4, -9.0, 0.1) R_E$ (where $1 R_E = 6,371$ km) in GSM (Geocentric Solar Magnetospheric) coordinates. The remaining three Cluster spacecraft, which were separated by $0.2 R_E$ from the C4 spacecraft, also observed similar tearing distributions.

Figure 7.2 shows how the electron temperature, magnetic field, and plasma flow evolve during this particular event. The times of tearing distributions are indicated by red dots. The lines A, B, and C represent the times of the distributions which we show in Figure 7.3, line A represents a time before the detection of the tearing distribution at which C4 crossed the tail current sheet, line B represents the time of a tearing distribution detection, and line C represents a time after this detection.

According to the data presented in Figure 7.2, this event fulfills the tearing criteria listed in section 7.4 [Schindler *et al.*, 1973; Liu *et al.*, 2014]:

1. The plasma fulfills the criterion in equation 7.1 (see Figure 7.1).
2. The temperature increases rapidly after the detection of the tearing distribution, in conjunction with an increase in electron anisotropy (T_{\perp}/T_{\parallel}) from ~ 0.6 to ~ 1 . These anisotropy changes agree with PIC simulations [Buechner and Zelenyi, 1987; Liu *et al.*, 2014; Walker *et al.*, 2018] that predict that the tearing distribution evolves into an isotropic distribution during the growth of the tearing instability. Figure 7.3 illustrates this temperature and anisotropy evolution. A low energy isotropic distribution prior to tearing evolves into a strong field-aligned distribution, followed by an isotropic distribution with a higher temperature, as expected from theory.

After noting the close correspondence between the observations and simulations of the

Table 5: Times of the 15 tearing events, along with the spacecraft which detected the tearing distributions and the subsequent magnetic reconnection signatures.

Event #	Spacecraft	Time of Tearing	Reconnection Seen
1	C1, C2, C3, C4	17:11:12 UT, 18/08/2002	Yes
2	C1, C2, C3, C4	13:26:57 UT, 18/09/2002	Yes
3	C1, C2, C3, C4	20:48:37 UT, 02/10/2002	Yes
4	C1, C2, C3, C4	21:21:21 UT, 02/10/2002	Yes
5	C1, C2, C3, C4	16:43:17 UT, 17/08/2003	Yes
6	C1, C2, C3, C4	18:57:27 UT, 24/08/2003	Yes
7	C1, C2, C3, C4	06:19:12 UT, 04/10/2003	Yes
8	C1, C2, C3, C4	23:29:05 UT, 07/08/2004	Yes
9	C2, C3, C4	02:16:57 UT, 10/08/2005	Yes
10	C2, C3, C4	02:58:28 UT, 10/08/2005	No
11	C3, C4	21:52:25 UT, 07/08/2008	No
12	C1	01:19:21 UT, 15/09/2008	Yes
13	C1, C3, C4	01:17:59 UT, 02/09/2009	No
14	C1, C3, C4	21:19:37 UT, 13/09/2009	No
15	C1, C3, C4	21:31:52 UT, 13/09/2009	No

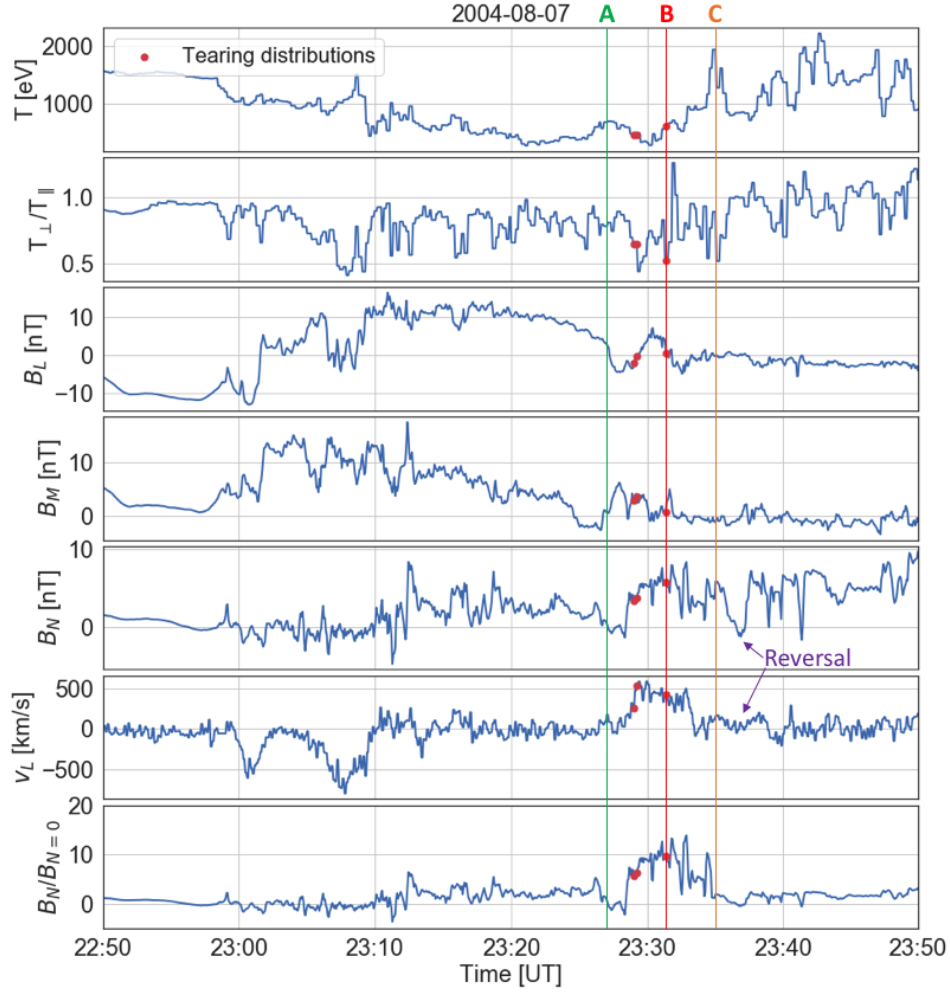


Figure 7.2: Spacecraft measurements indicating the presence of the tearing instability.

The plasma and magnetic field parameters obtained by the C4 spacecraft across times 22:50:00 - 23:50:00 on 07/08/2004. From top to bottom: electron temperature, electron T_{\perp}/T_{\parallel} , magnetic field in the L , M , N -directions respectively (in local magnetic coordinates), plasma flow velocity in the L -direction, and the $B_N/B_{N=0}$ ratio. A flow reversal is highlighted in the B_N and v_L panels. The red points indicate times of the tearing distributions identified by our outlier detection method. The lines labelled A, B, and C represent times of pre-tearing, tearing, and post-tearing distributions respectively. We show the distributions measured at these times in Figure 7.3.

tearing mode, we can gain further insight into the time evolution of the tearing mode. Firstly, the field-aligned population lasts for just over two minutes, during which the total temperature remains approximately stable at ~ 400 eV. After the last tearing distribution is detected, a rapid growth in temperature reaches a peak of 1979 eV, 336 s after the first tearing distribution. As the tearing mechanism is characterised by the evolution of a field-aligned distribution into an isotropic distribution at higher temperatures, we attribute this time of 336 s to the growth time of the instability for this event. After this temperature increase, the spacecraft observes direct evidence of magnetic reconnection at 23:36:52 UT, i.e. 467 s (or 7 min 47 s) after the first tearing distribution, as shown by the simultaneous reversal in B_N and v_L (from positive to negative values) in Figure 7.2 after the tearing distributions.

To calculate the current sheet thickness, a (where $a = 2L_N$), we use the following equation [Thompson *et al.*, 2005]:

$$a = 2 \frac{B_0^2 - B_L^2}{\mu_0 B_0 J_M}, \quad (7.2)$$

where B_0 is the lobe magnetic field strength, obtained from Bakrania *et al.* [2020], B_L is the local magnetic field in the L direction (depending on the coordinate system), and J_M is the local current density in the M direction. We obtain the current density using multi-spacecraft measurements from [Perri *et al.*, 2017; Dunlop *et al.*, 1988]:

$$\mu_0 \mathbf{J}_{ijk} \cdot (\Delta \mathbf{r}_{ik} \times \Delta \mathbf{r}_{jk}) = \Delta \mathbf{B}_{ik} \cdot \Delta \mathbf{r}_{jk} - \Delta \mathbf{B}_{jk} \cdot \Delta \mathbf{r}_{ik}, \quad (7.3)$$

where i, j, k represent the C1, C3, and C4 spacecraft respectively. \mathbf{J}_{ijk} and \mathbf{B}_{ijk} are the local current density and magnetic field. For our 07/08/2004 event, we estimate a current sheet width of $0.72 R_E$, corresponding to ~ 2 ion gyroradii.

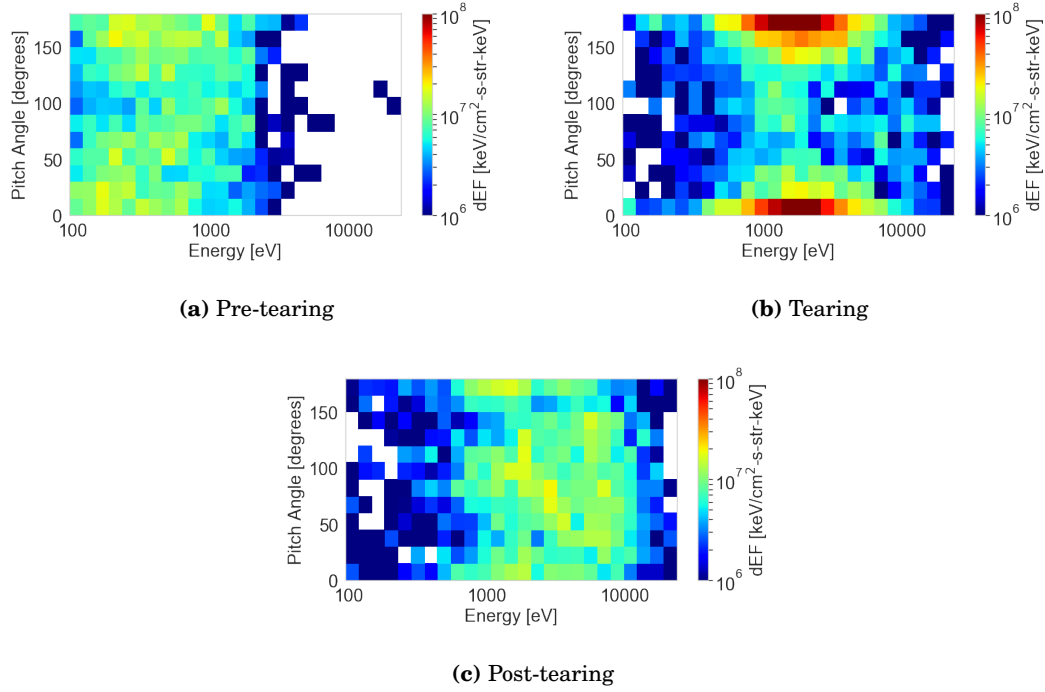


Figure 7.3: The evolution of a tearing distribution into an isotropic distribution with a higher bulk energy. The differential energy flux distributions as a function of pitch angle and energy, which correspond to the times A (23:27:13 UT), B (23:34:23 UT), and C (23:34:41 UT) in Figure 7.2 as measured by the C4 PEACE instrument.

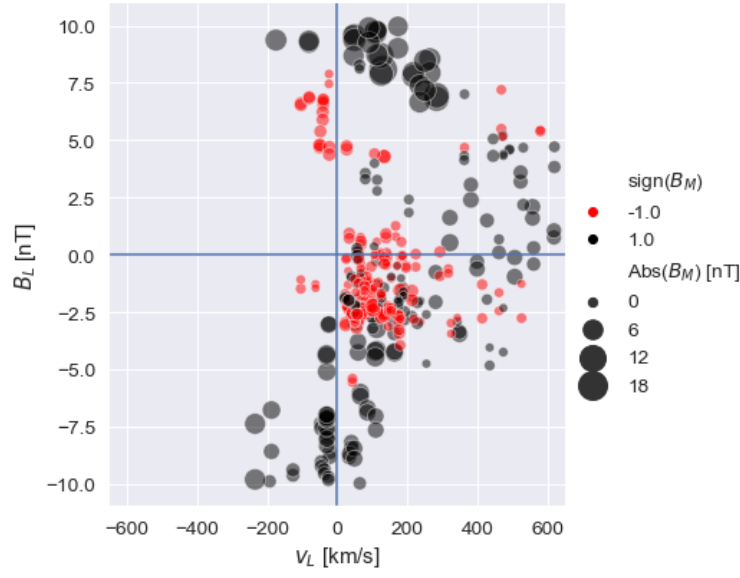
The local Alfvén speed is calculated as [Landi *et al.*, 2015]:

$$v_A = B_L / \sqrt{4\pi\rho_0}, \quad (7.4)$$

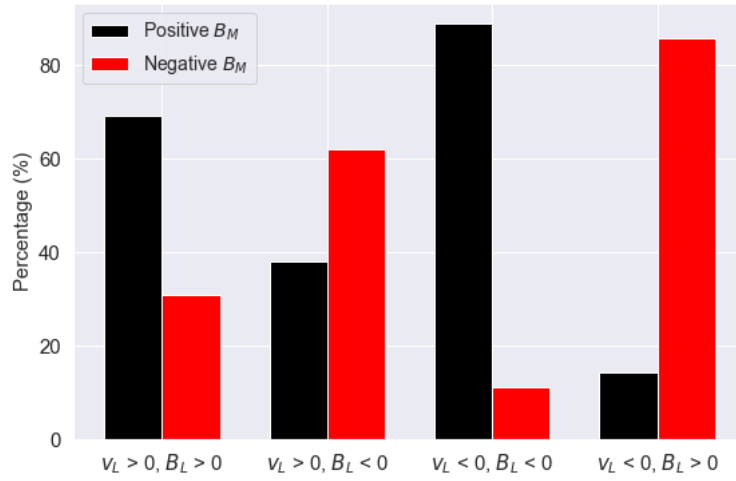
where B_L is the L -component of the background magnetic field and ρ_0 is the plasma density. The magnetic field and ion density used for calculating the Alfvén speed (Eq. 7.4) are obtained by averaging the measurements across all Cluster spacecraft when they were outside the current sheet, within ~ 30 min of the tearing event. With an average background density and B_L field of 0.14 cm^{-3} and 13.1 nT respectively, we calculate an Alfvén speed of $7.6 \times 10^5 \text{ m/s}$ for our case study event.

Nagai *et al.* [2001] find that the reconnection process generates a current system known as the Hall quadrupole magnetic field [Karimabadi *et al.*, 2004]. Figure 7.4 shows the out-of-plane magnetic field (B_M) values in the along-current sheet (B_L - v_L) plane after our 07/08/2004 tearing event, which confirms the presence of this characteristic Hall quadrupolar field (see section 7.5). The scatter of the points in Figure 7.4 shows that negative B_M values dominate in the upper left and bottom right quadrants, while positive B_M values dominate in the other two quadrants. This pattern corresponds to the quadrupole signature of correlation (anti-correlation) with v_L , i.e. the speed of plasma flow in the L -direction, in the Northern (Southern) Hemisphere (this quadrupole pattern is also illustrated in Figure 7.5). The bar chart in Figure 7.4b confirms this quadrupole observation, as there is a clear dominance of positive or negative B_M depending on the respective quadrant, in keeping with the expected signatures from magnetic reconnection.

Figure 7.5 provides a schematic detailing the evolution of a laminar current sheet into a reconnection site via the tearing instability consistent with the observations of our 07/08/2004 event. We also illustrate the magnetic islands [Ishizawa and Nakajima, 2010] in 3D along



(a)



(b)

Figure 7.4: (a) Statistical determination of a reconnection site. Quadrupole plot showing B_M as a function of B_L and v_L , across a 10 minute window centered on the B_N reversal in Figure 7.2 (at 23:36:52 UT) after the tearing instability distributions. Black dots correspond to $B_M > 0$ and red dots correspond to $B_M < 0$. The size of the dots is proportional to the magnitude of B_M . **(b)** The percentage of instances with $B_M > 0$ and $B_M < 0$ in each quadrant.

with their expected location in near-Earth space. Each panel corresponds to the timestamps A, B, or C in Figure 7.2. The green crosses show the C4 spacecraft position at each time, and the green arrow shows the overall trajectory, as informed by the magnetic field measurements. The background colours illustrate the electron temperature in the reconnection site and the surrounding magnetic islands [Lu *et al.*, 2019], with the scale informed by temperature measurements in our event. As the diagram shows, the magnetic island formation coincides with an increase in electron temperature, as observed by the spacecraft after time B in Figure 7.2. The spacecraft then observes the X-point, as signified by the flow reversal in Figure 7.2, which aligns with a region of lower temperature. Subsequently, the spacecraft observes the second region of high temperature.

From our case study, we construct a picture of the tearing instability, incorporating the temperature profiles and electron distribution functions of a tearing unstable plasma. We also relate the instability to the onset of reconnection. Our statistical survey will allow us to further quantify the tearing instability and its relationship with reconnection, building in analysis from all 15 of our tearing events.

7.6.3 Statistical survey of tearing events

Our method finds 14 other events that we use to explore the properties of the tearing mode. We carry out a superposed epoch analysis of the SML (SuperMAG Auroral Lower) [Gjerloev, 2012] indices around each of the 15 tearing events, to determine how they relate to substorm phase [Forsyth *et al.*, 2015]. At the end of the expansion phase, the SML index is at its maximum magnitude, and subsequently decreases in the recovery phase. Fig. 7.6 shows that the tearing events occur during the expansion and recovery phase, with the average time located at the end of the expansion phase. The box plot shows that the majority of the

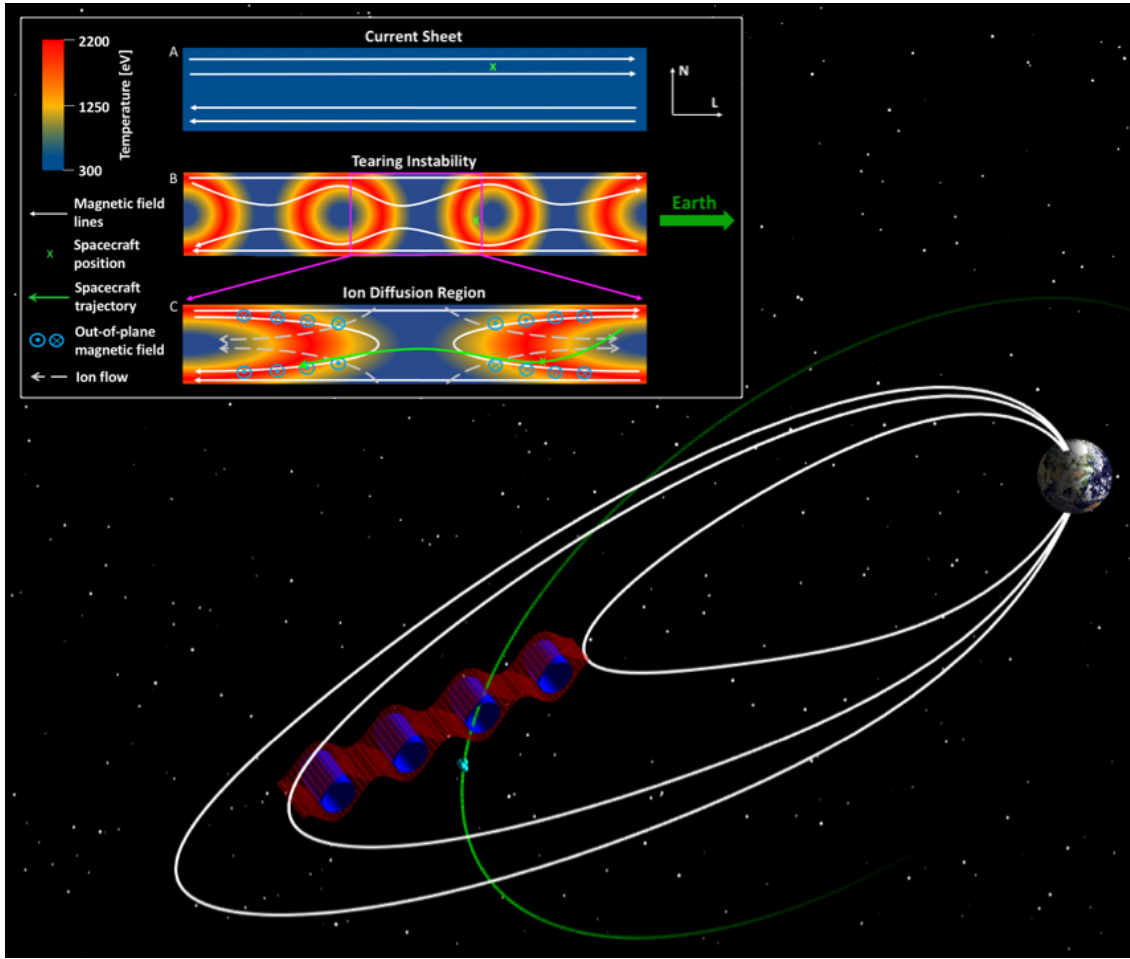


Figure 7.5: Illustration of the evolution of magnetic field lines from a flat current sheet into a reconnection site via the tearing instability, with a 3D representation of the magnetic islands in the Earth's vicinity. The background colours represent the local electron temperature [Lu *et al.*, 2019], with the scales based on the temperatures observed by the C4 spacecraft during the 07/08/2004 tearing event. The white lines represent the magnetic field lines. The three panels correspond to the times A, B, and C in Fig. 7.2, and the green crosses show the location the C4 spacecraft at each time. The green arrow shows the overall trajectory of the spacecraft across this reconnection region in our case study event. The Hall quadrupole field (blue dots and crosses) and corresponding ion flows (dotted grey arrows) are also displayed.

tearing times are located closer to the maximum SML magnitude. As the growth phase is by far the most prevalent phase of a substorm [*Forsyth et al.*, 2015] (see Fig. 7.7), a chi-squared test [*Tallarida and Murray*, 1987] between the tearing events and plasma sheet distributions in Fig. 7.7 shows that the occurrence of all tearing events during the expansion and recovery phase is statistically significant to a p-value of <0.05 , as the two distributions cannot be derived from the same source. This analysis confirms that our tearing events occur under an externally driven current sheet (which is the case during the expansion phase), as expected from simulations [*Bessho and Bhattacharjee*, 2014].

Fig. 7.8 shows a histogram of the amount of time Cluster spent in each MLT bin during the times ECLAT recorded the spacecraft to be in the plasma sheet. We see that the plasma sheet is clearly more prevalent on the dawn side, especially between MLT 3 and 4. There is also a smaller peak in the dusk side between MLTs 21 and 22. Fig. 7.9 shows a histogram of MLTs for each of the 15 tearing events. Similar to Fig. 7.8, there are peaks in both the dusk side and the dawn side, with the dawn side peak appearing much larger. These peaks are located at different MLT bins however: 22-23 and 1-2 respectively. We perform a Kolmogorov-Smirnov (KS) 2-sample test [*Jr.*, 1951] on the distributions in Fig. 7.8 and 7.9, to determine whether they are derived from the same or different distributions. We obtain a KS statistic of 0.46 with a p-value of 0.0019, which confirm that the longitudinal location of tearing events is independent of the location of the magnetotail plasma sheet.

Fig. 7.10 shows a histogram of MLTs of the 15 substorm events (obtained from the SOPHIE dataset) that took place at similar times to our 15 tearing events. Unlike the previous two histograms, this substorm MLT distribution only has one peak, which is located in the dawn side in the MLT bin 1-2 (the same as the dawn side peak in the tearing MLT

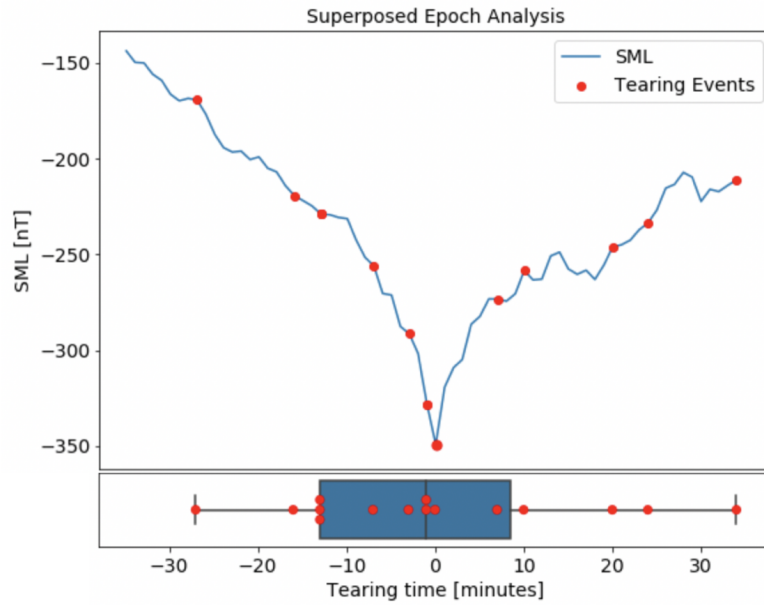


Figure 7.6: Superposed epoch analysis of SML relating tearing to substorms. The spread of tearing times for all 15 events compared to the superposed epoch analysis of SML measurements across each of the 15 events. The blue curve is calculated by averaging the SML peak around each of the 15 tearing events, while the location of the red dots represents the relative timings of each particular tearing event in comparison to its associated peak in SML. The box plot underneath summarises the distribution of tearing event timings in comparison to the peak in SML. Red dots overlay the box plot to distribution of tearing times independent of the SML value. The vertical lines of the red box show the lower quartile, mean, and upper quartile of the relative times, while the two longest lines show the earliest and latest tearing event.

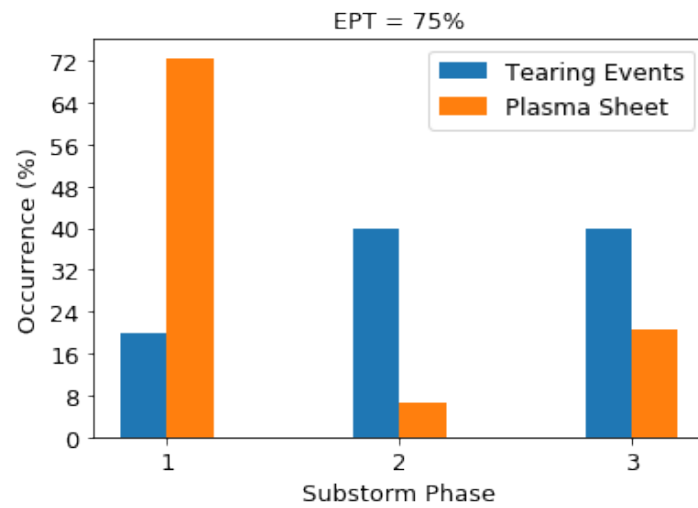


Figure 7.7: Bar chart comparing the substorm phase occurrence during each tearing event to the overall substorm phase occurrence when the spacecraft was in the plasma sheet.

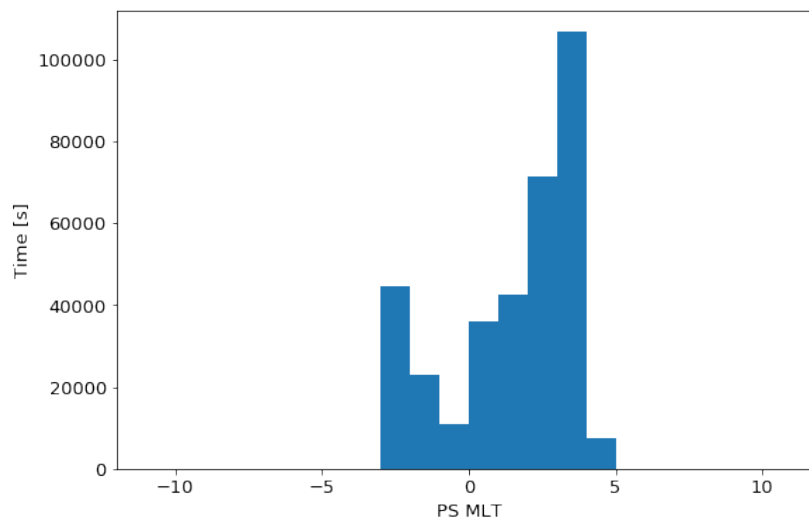


Figure 7.8: Histogram of the time Cluster spent in each MLT bin when the spacecraft was in the plasma sheet.

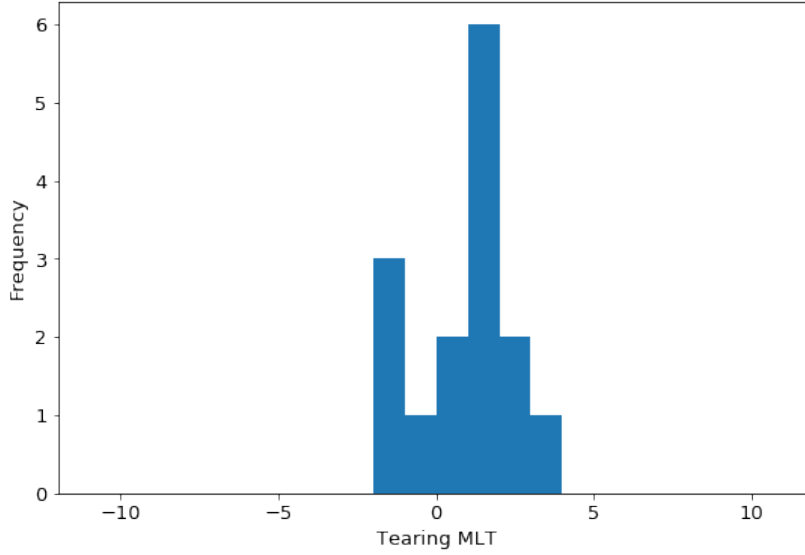


Figure 7.9: Histogram of MLTs of all 15 tearing events.

histogram). As previously, we apply the KS 2-sample test to compare this substorm MLT distribution to both the plasma sheet MLT distribution and the tearing MLT distribution. Firstly, we obtain a KS statistic of 0.46 with a p-value of 0.0018 when comparing the plasma sheet to the substorm MLT distributions. This again shows that the longitudinal locations of substorm events are independent of the location of the plasma sheet, highlighting the fact that other factors are important in determining where substorms are found to take place. Finally, we obtain a KS statistic of 0.13 with an associated p-value of 0.9998 when comparing the tearing to substorm MLT distributions. As the p-value is larger than 0.95, these distributions can therefore be derived from the same source (to a confidence level of 5%). This confirms that the location of substorm events, that occurred during our tearing events, is linked to the location of our tearing events.

Our calculations of the current sheet thickness [*Thompson et al.*, 2005] using equation (7.2) also reveal evidence of current sheet thinning, further showing that the current sheet is

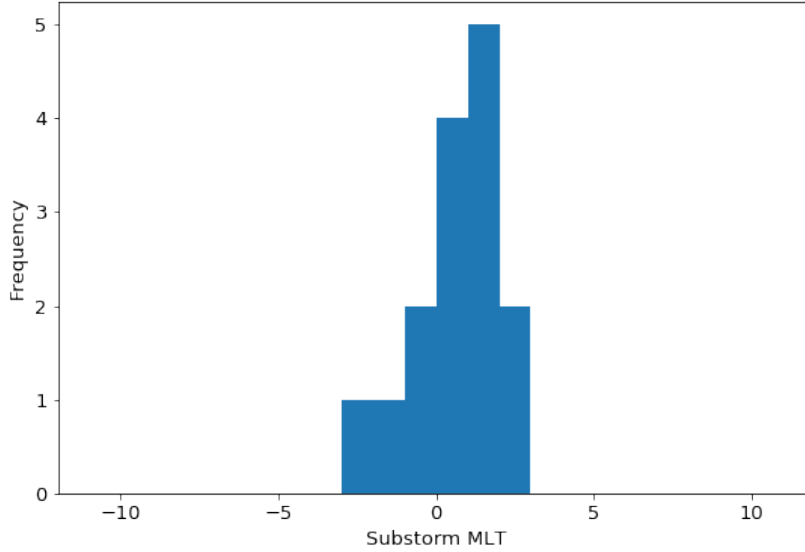


Figure 7.10: Histogram of MLTs of the recorded substorms linked to the 15 tearing events.

being driven by the substorm expansion phase. *Saito* [2015] finds that the average current sheet thickness is roughly $6 R_E$. Across each of the tearing events, we calculate an average of $0.6 R_E$, with a minimum value of $0.39 R_E$ and a maximum value of $0.77 R_E$.

In our statistical survey, we determine the growth times of the instability across all events, based on the time between the first detection of a field-aligned distribution and the subsequent peak in temperature. In the 15 events, we find that the average growth time is 601 s, with a lower quartile of 348 s and an upper quartile of 766 s. The minimum and maximum growth times are 224 s and 1200 s respectively. The average peak temperature across all events is 2691 eV, with a lower quartile of 1766 eV and an upper quartile of 2871 eV. The average change in temperature is 1712 eV. Our analysis shows large variations in the temperature of a tearing unstable plasma. As expected [*Galeev and Zelenii*, 1976], we do not observe a correlation between the temperature and growth time of the instability.

Using multi-spacecraft techniques, we also constrain the size of the region undergoing

tearing. In the 07/08/2004 event (Fig. 7.2), we find that all four Cluster spacecraft observe the characteristic field-aligned distributions indicating tearing. The maximum distance between the spacecraft is $0.20 R_E$ at this time, and for all events, when the spacecraft are less than $1 R_E$ from an observed tearing distribution, a similar field-aligned tearing distribution is observed; spacecraft that are more than $1 R_E$ from an observed tearing distribution do not observe tearing distributions. However, all four spacecraft in all tearing events observe the characteristic temperature rise after the tearing distribution, suggesting the region of subsequent particle energisation from tearing-initiated reconnection extends to at least $1.36 R_E$ in the surrounding plasma (the largest distance between two spacecraft across all tearing events).

In order to better understand the plasma dynamics experienced by Cluster around a tearing event when either multiple spacecraft or a single spacecraft observes tearing, we produce the quiver plots shown in Fig. 7.11 and 7.12. These plots show the plasma flow velocities experienced by two Cluster spacecraft during their flight around the time a tearing event is observed. Fig. 7.11 is our 07/08/2004 case study event where both C3 and C4 (the two spacecraft shown in the plot) observe tearing. Fig. 7.12 shows the 15/09/2008 event where the flight paths of the C1 spacecraft, which observes tearing, and the C3 spacecraft, which does not observe tearing, are displayed. It is clear that the plasma flow velocities experienced by both C3 and C4 in Fig. 7.11 are very similar across the whole hour of flight shown, with the direction of plasma flow being mirrored for both spacecraft. On the other hand, the plasma flows experienced by the two spacecraft in Fig. 7.12 are noticeably different (before and after tearing), with the direction of flow varying between the spacecraft across the whole flight path shown. These differences show that the spacecraft are far enough away from

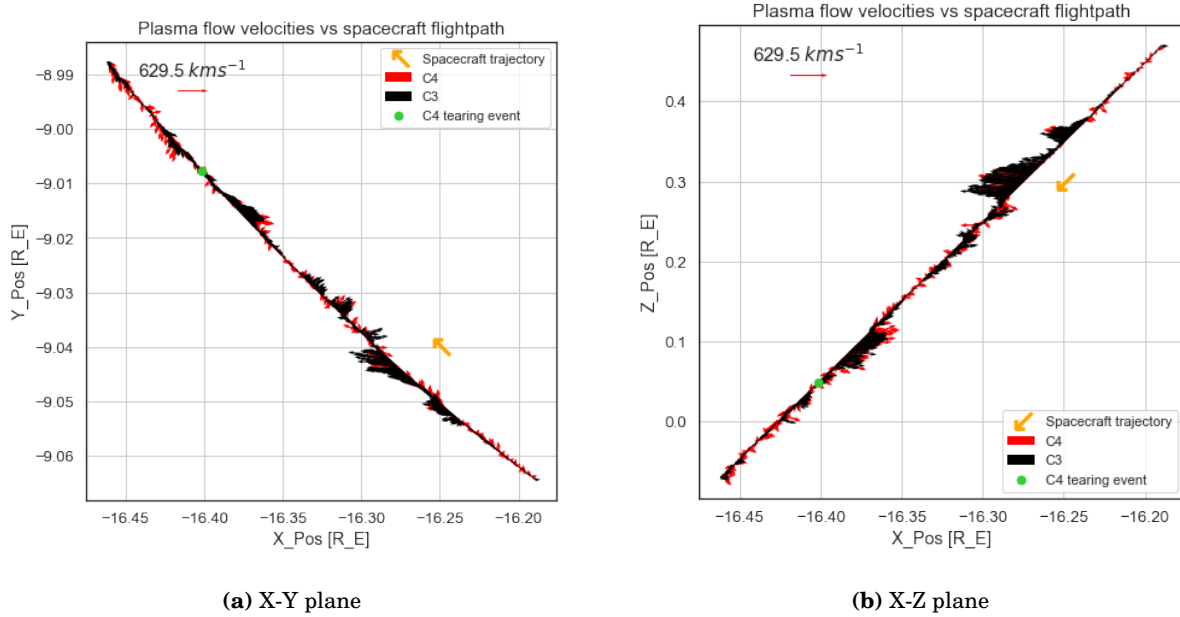
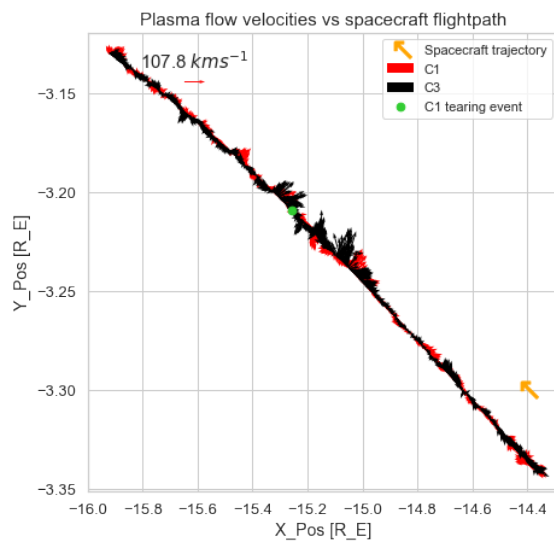


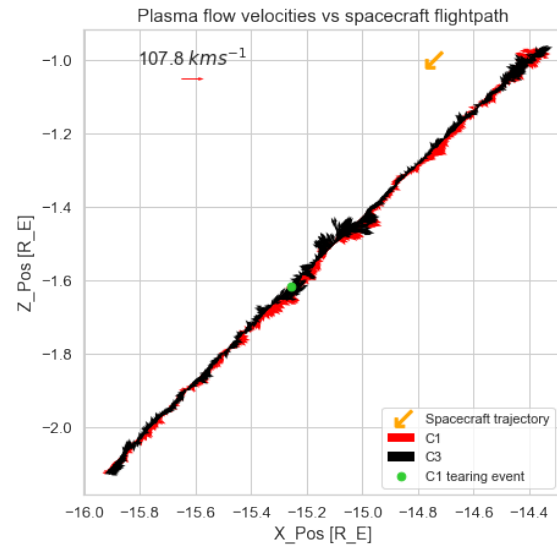
Figure 7.11: A quiver plot showing the plasma flow velocities experienced by the C3 (black arrows) and C4 (red arrows) spacecraft around the 07/08/2004 tearing event from times 22:50 UT to 23:50 UT in the (a) X-Y plane and the (b) X-Z plane (GSM coordinates). Both spacecraft observe tearing. The green dots show the time of the event during the spacecraft trajectory, the orange arrows shows the direction of spacecraft travel, and the length of the red and black arrows correlates to the plasma flow velocity.

each other ($>1 R_E$) so that plasma environments are different, and therefore the signatures of tearing are not observed by both spacecraft, as opposed to Fig. 7.11.

Of the 15 tearing events, we observe signatures of reconnection after 10 of them. For 8 of these 10 events, the spacecraft crosses the current sheet and we observe the characteristic Hall quadrupole magnetic field [Borg *et al.*, 2012]. Eastwood *et al.* [2010] also confirm the presence of a reconnection site for 7 of these events. For the remaining two reconnection events, the spacecraft do not traverse the current sheet; rather they remain below the current sheet and therefore cannot detect all quadrants of the Hall quadrupole field. In



(a) X-Y plane



(b) X-Z plane

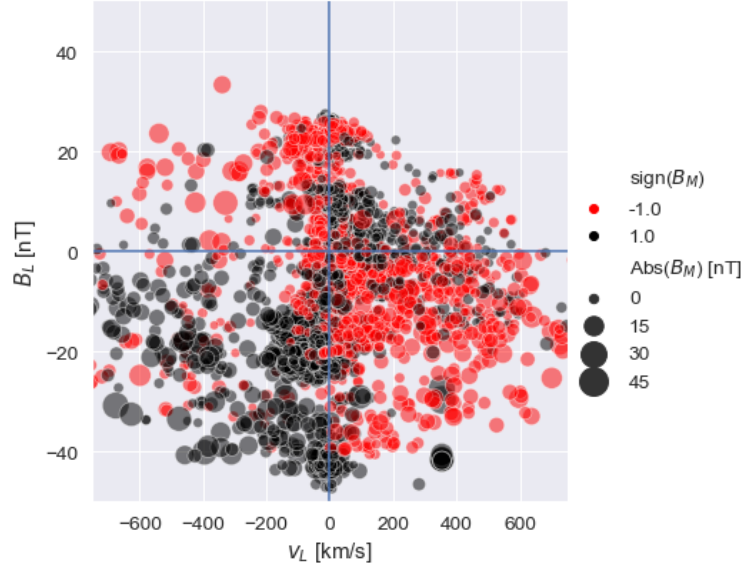
Figure 7.12: A quiver plot showing the plasma flow velocities experienced by the C1 (red arrows) and C3 (black arrows) spacecraft around the 15/09/2008 tearing event from times 00:07:54 UT to 02:21:20 UT in the (a) X-Y plane and the (b) X-Z plane (GSM coordinates). Only the C1 spacecraft observes tearing. All other features are the same as in Fig. 7.11.

these two events, the spacecraft and current sheet are moving closer together, so we observe an anti-correlation between B_M and v_L , i.e. two of the four expected quadrants, highlighting the presence of a diffusion region associated with reconnection [Eastwood *et al.*, 2010]. For the other 5 tearing events where the spacecraft do not observe a diffusion region, the spacecraft remain in the Southern Hemisphere and the B_L field increases in magnitude, indicating that the spacecraft and current sheet are moving apart.

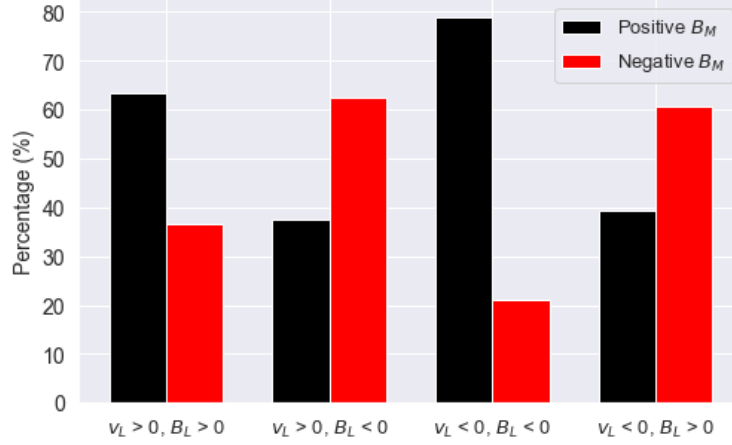
Fig. 7.13 shows a summary of the quadrupolar signatures expected from magnetic reconnection for all 10 of the tearing-reconnection events. It can be seen from Fig. 7.13 that there is a clear average quadrupole signature which the corresponding bar chart confirms. There are similar time delays between the first tearing distribution and the observation of a reconnection X-point across all 8 events where a reconnection X-point is observed. This delay varies between 5 min 32 s and 8 min 20 s, a variation possibly caused by unpredictable current sheet flapping [Sergeev *et al.*, 2003; Forsyth *et al.*, 2009]. These findings provide an insight into the characteristic timescale of reconnection site formation as a result of the tearing instability.

7.7 Discussion

The tearing mode instability is widely considered to be the dominant mechanism responsible for the onset of magnetic reconnection in high- β collisionless plasmas [Galeev and Zelenii, 1976; Schindler *et al.*, 1973]. Although this instability has not previously been observed with in-situ data in space plasmas, past studies have found evidence of the tearing instability and subsequent field line reconnection in laboratory plasmas [Gekelman and Pfister, 1988; Gekelman *et al.*, 1991]. There have also been qualitative observations of tearing-induced reconnection in solar flares [Gekelman *et al.*, 1991], as well as countless simulation studies



(a)



(b)

Figure 7.13: (a) Quadrupole plot showing the out-of-plane magnetic field B_M in the B_L - v_L plane, for 10 of our observations where a reconnection signature is observed after the tearing instability distributions. The features of this plot are consistent with those seen in Fig. 7.4. (b) The percentage of instances with $B_M > 0$ and $B_M < 0$ in each quadrant.

of how the tearing instability leads to reconnection [e.g. *Liu et al.*, 2014].

In this study, we present the first in-situ observations of distributions that are consistent with the tearing mode instability in the high- β environment of Earth's magnetotail plasma sheet. These tearing mode events are discovered by applying a neural network outlier detection method [*Bakrania et al.*, 2020] to Cluster-PEACE data of the electron velocity distribution functions taken within the plasma sheet. These neural network methods have applications in any plasma environment where in-situ measurements are available. We identify 15 separate cases of the tearing mode, and confirm that they fulfill the theoretical tearing instability criteria [*Schindler et al.*, 1973] and match simulations of the evolution of electron anisotropy and temperature.

As magnetotail current sheet plasmas share similarities with other environments in which the tearing instability is important, our observations provide a fundamental understanding of the mechanism responsible for the initiation of magnetic reconnection. We detect signatures of magnetic reconnection after 10 of the 15 events, producing observational evidence for the link between tearing and reconnection, a link which has only been shown in simulations to date [*Bhattacharjee et al.*, 2009]. The lack of reconnection signatures after the other 5 tearing events can be explained by the relative position and trajectory of the spacecraft with respect to the reconnecting current sheet (based on the increase in magnitude of B_L).

Our observations enable us to make the first experimental measurements of the growth times of the tearing mode, improving our understanding of the timescales of the instability. The growth time of each tearing event varies between 4 and 20 minutes, and with no apparent correlation between the tearing growth time and the value of the subsequent peak

temperature, which is a measure of the energisation of the plasma following reconnection. In order to understand how the growth of the tearing instability relates to the properties of the surrounding plasma, we calculate the characteristic Alfvén timescales (τ_A) of the system for each event. We find that the ratio between the tearing and Alfvén timescales is ~ 100 across all 15 events. These results show that the relative growth rate of the tearing mode is in fact one order of magnitude lower than predicted in simulations [Walker *et al.*, 2018; Wang *et al.*, 1988].

The main source of uncertainty in our estimation of the growth time lies in the assumption that the spacecraft observe the true start and end of tearing, which cannot be unambiguously determined by in-situ observations alone. If the spacecraft are not observing the true start of the tearing instability, then our calculated time delays may actually characterise the physical distance between the tearing distribution and isotropic distribution, rather than the growth time. As our calculations of the growth rate are underestimates of the true growth rate, the discrepancy between our calculations and previous studies, regarding the growth time to Alfvén timescales, may not be as large.

With the aid of the SOPHIE dataset, we can link the occurrence of the tearing events, as well as their longitudinal locations, to the substorm phase and location of substorm events that occurred at similar times to our 15 tearing events. We find that the tearing instability is significantly more likely to occur during the expansion and recovery phase, than the growth phase, and on average the tearing instability occurs on the boundary between the expansion and recovery phase. As the expansion phase is initiated due to an externally driven current sheet, we confirm that this externally driven current sheet is also a prerequisite for tearing in the magnetotail, as expected from simulations. In terms of our investigation into the

MLT of tearing and substorm events, we find that the location of both tearing and substorm onset are consistent, based on their MLT distributions. This consistency shows that both phenomena occur under the same process, and that the tearing events we found are part of a larger substorm process in the Earth's magnetosphere.

The time delay between the first tearing distribution and the formation of the reconnection site varies within a narrow range of 5 min 32 s to 8 min 20 s across our events. This narrow range of times points towards a consistent delay between tearing and reconnection site formation, similar to that found in simulations [*Chen et al.*, 1997]. Our multi-spacecraft analysis shows that the size of the tearing region itself is less than $\sim 1 R_E$. More high cadence multi-spacecraft measurements, such as measurements from the MMS [*Sharma and Curtis*, 2005] (Magnetospheric Multiscale Mission) mission, will be important in furthering this investigation into the size and location of tearing regions.

8 Conclusions and Future Work

In our first study, we apply unsupervised K-means clustering algorithms to Cluster-PEACE data to separate solar wind electron pitch angle and energy distributions into the core, halo, and strahl populations. This enables us to perform an accurate statistical analysis of strahl and halo breakpoint energies. In our statistical study, we compare the relationship between core temperature, T_c and both halo and strahl breakpoint energies. We present a strong correlation between suprathermal breakpoint energies and T_c , and conclude this is due to core temperature being a determining factor for breakpoint energy. As a result of higher core temperatures, the Maxwellian part of the total electron velocity distribution function, which represents the core, extends across a wider range of velocity space [Pilipp *et al.*, 1987a]. The core distribution therefore overlaps with the halo and strahl at higher energies and thus increases the suprathermal breakpoint energy.

We find that halo breakpoint energy remains larger than the strahl's across all temperatures. This difference between halo and strahl breakpoint energies suggests that there are certain energies, below the halo breakpoint energy, at which a strahl and core population are both present. At these energies, strahl dominates at parallel pitch angles and core dominates at perpendicular pitch angles. Wave-particle scattering processes [Gary *et al.*, 1994; Vasko *et al.*, 2019; Verscharen *et al.*, 2019] scatter these low energy strahl electrons to higher perpendicular velocities and smaller parallel velocities. At sufficiently high core temperatures, these strahl electrons would be absorbed by the core population [Pilipp *et al.*, 1990], instead of the higher energy halo population. The absorption of strahl electrons by the core increases the number of Coulomb collisions [Landi *et al.*, 2012], which then leads

to an increase in core temperature [Marsch and Goldstein, 1983; Boldyrev *et al.*, 2020]. This scenario is consistent with previous studies [Pilipp *et al.*, 1987b] which show a transfer of electron kinetic energy from the parallel to perpendicular direction, increasing core temperature in the perpendicular direction. The increase of core temperature, due to the absorption of strahl electrons, acts to extend the core component of the electron velocity distribution function to higher velocities [Pilipp *et al.*, 1987a], therefore increasing the halo breakpoint energy at pitch angles at which the strahl is not present. This phenomenon explains the larger difference between strahl and halo breakpoint energies at higher core temperatures, as a larger difference in breakpoint energy means more strahl electrons are scattering into the core population rather than the halo population.

This work signifies the first extensive study in characterising the relation between breakpoint energy and solar wind speed, for each of the suprathermal populations. Our results show there is a significant decrease in both halo and strahl breakpoint energies with increasing solar wind speed, with the halo relation exhibiting a stronger correlation. We find two distinct relationships in the halo breakpoint energy vs. solar wind speed distribution, with a step function at 500 km/s. We predict this step function relates to the difference in origin of fast and slow solar wind electrons [Feldman *et al.*, 2005]. Further investigation, with the aid of new facilities provided by the Parker Solar Probe and Solar Orbiter missions, can test this prediction and investigate why the step function is prevalent in the halo breakpoint energy relationship but not in the strahl breakpoint energy relationship with solar wind speed. In future studies, using Solar Orbiter measurements at smaller heliocentric distances will allow us to better characterise halo and strahl breakpoint energies and improve our understanding of their dependence on bulk solar wind parameters.

In Chapter 6, we employ novel machine learning techniques to characterise particle distribution functions in the magnetotail. Particle populations in collisionless space plasma environments are traditionally characterised by their moments. Distribution functions, however, provide the full picture of the state of each plasma environment. Distribution functions are not easily classified by a small number of parameters. We therefore propose to apply dimensionality reduction and clustering methods to particle distributions in pitch angle and energy space as a new method to distinguish between the different plasma regions. Dimensionality reduction is a specific type of unsupervised learning in which data in high-dimensional space is transformed to a meaningful representation in lower dimensional space. This transformation allows complex datasets to be characterised by analysis techniques with much more computational efficiency. We use the autoencoder to compress the data by a factor of 10 from a high-dimensional representation. We subsequently apply the PCA algorithm to further compress the data to a three-dimensional representation. After compressing the data, we use the mean shift algorithm to inform us of how many populations are present in the data using this three-dimensional representation. And finally, we use an agglomerative clustering algorithm to assign each data-point to one of the populations.

Fig. 6.5 shows the result of applying the agglomerative clustering algorithm to the compressed magnetotail electron. The plot shows that the clustering algorithm is able to assign data-points of varying PCA values to the same cluster if they belong to the same complex non-spherical structure. The clustering algorithm is able to form clear boundaries between clusters with adjacent PCA values, with no mixing of cluster labels on either side of the boundaries.

Fig. 6.6 shows the average electron differential energy flux distributions for each cluster. We see large differences in the average pitch angle/energy distributions. Each distribution differs by the: peak flux energy, peak flux value, or the pitch angle anisotropy. The lack of identical distributions shows mean shift has not overestimated the number of clusters.

Table 4 shows a contingency table comparing our classifications to the original ECLAT labels. The majority of clustering labels are in agreement with the ECLAT regions. For AC labels 0, 1, 2, 4, and 6, which represent various populations within the plasma sheet, there is 100% agreement with the ECLAT label 0.

By using this method to characterise pitch angle and energy distributions, instead of using the derived moments, we successfully distinguish between multiple populations within what has historically been considered as one region, due to the lack of variation in the plasma. The automated classification of different regions in space plasma environments provides a useful tool to identify the physical processes governing particle populations in near-Earth space. These tools are model independent, providing reproducible results without requiring the placement of arbitrary thresholds, limits or expert judgment. Similar methods could be used onboard spacecraft to reduce the dimensionality of distributions in order to optimize data collection and downlink resources in future missions.

Magnetic reconnection is a ubiquitous process in space, laboratory, and astrophysical plasmas that converts magnetic energy to kinetic energy and results in a large variety of energetic events, including aurora, solar flares, astrophysical jets, and tokamak disruptions. Since the start of the space age, reconnection has been widely studied in different physical environments. Relatively little has been known, however, about the process by which reconnection is triggered. And until now, theory and simulations have provided the only insight

into this elusive tearing instability mechanism. The novel machine learning techniques we employ make our identification of the tearing instability possible on a consistent basis. In 10 years of high-resolution magnetotail plasma sheet crossings, we find 15 clear examples of tearing unstable distributions that occur prior to observations of magnetic reconnection, providing a clear link between these two physical processes. We show that the time delay between the two processes is of the order of a few minutes, which is also similar to the growth time of the instability prior to reconnection. Furthermore, we show that the timing of these events are linked to current sheet thinning, which occurs during the substorm expansion and recovery phases, confirming that the electron tearing instability results from externally driven processes.

In Chapter 7, we provide a comprehensive analysis of the temperature profiles and timescales during the tearing instability. Furthermore, we produce observational evidence for the connection between the tearing mode and reconnection, taking the first step in solving the longstanding problem of reconnection initiation with real-world data. More high cadence multi-spacecraft measurements, such as measurements from the MMS [*Sharma and Curtis, 2005*] (Magnetospheric Multiscale Mission) mission, will be important in furthering this investigation into the size and location of tearing regions. Our study serves as the groundwork for future studies that would investigate how tearing mode growth times vary across different plasma environments, from the magnetosphere to the solar corona and beyond.

References

- Abdi, H., and L. J. Williams (2010), Principal component analysis, *WIREs Computational Statistics*, 2(4), 433–459, doi:10.1002/wics.101.
- Agarap, A. F. (2018), Deep Learning using Rectified Linear Units (ReLU), *arXiv e-prints*, arXiv:1803.08375.
- Alfvén, H. (1942), Existence of electromagnetic-hydrodynamic waves, *Nature*, 150(3805), doi:10.1038/150405d0.
- Anderson, B. R., R. M. Skoug, J. T. Steinberg, and D. J. McComas (2012), Variability of the solar wind suprathermal electron strahl, *Journal of Geophysical Research: Space Physics*, 117(A4), doi:10.1029/2011JA017269.
- Angelopoulos, V., J. P. McFadden, D. Larson, C. W. Carlson, S. B. Mende, H. Frey, T. Phan, D. G. Sibeck, K.-H. Glassmeier, U. Auster, E. Donovan, I. R. Mann, I. J. Rae, C. T. Russell, A. Runov, X.-Z. Zhou, and L. Kepko (2008), Tail Reconnection Triggering Substorm Onset, *Science*, 321(5891), 931, doi:10.1126/science.1160495.
- Antiochos, S. K., Z. Mikić, V. S. Titov, R. Lionello, and J. A. Linker (2011), A model for the sources of the slow solar wind, *The Astrophysical Journal*, 731(2), 112, doi:10.1088/0004-637x/731/2/112.
- Artemyev, A. V., A. P. Walsh, A. A. Petrukovich, W. Baumjohann, R. Nakamura, and A. N. Fazakerley (2014), Electron pitch angle/energy distribution in the magnetotail, *Journal of Geophysical Research: Space Physics*, 119(9), 7214–7227, doi:10.1002/2014JA020350.

- Arthur, D. (2007), k-means++ : The advantages of careful seeding, *Proceedings of the eighteenth annual ACM-SIAM symposium on Discrete algorithms*, pp. 1027–1035.
- Bakrania, M. R., I. J. Rae, A. P. Walsh, D. Verscharen, and A. W. Smith (2020), Using dimensionality reduction and clustering techniques to classify space plasma regimes, *Frontiers in Astronomy and Space Sciences*, 7, 80, doi:10.3389/fspas.2020.593516.
- Bale, S. D., M. Pulupa, C. Salem, C. H. K. Chen, and E. Quataert (2013), Electron heat conduction in the solar wind: Transition from spitzer-hÄrm to the collisionless limit, *The Astrophysical Journal*, 769(2), L22, doi:10.1088/2041-8205/769/2/l22.
- Balogh, A., and E. J. Smith (2001), The heliospheric magnetic field at solar maximum: Ulysses observations, in *The 3-D Heliosphere at Solar Maximum*, pp. 147–160, Springer Netherlands, Dordrecht.
- Balogh, A., M. W. Dunlop, S. W. H. Cowley, D. J. Southwood, J. G. Thomlinson, K. H. Glassmeier, G. Musmann, H. LÜHR, S. Buchert, M. H. Acuña, D. H. Fairfield, J. A. Slavin, W. Riedler, K. Schwingenschuh, and M. G. Kivelson (1997), The cluster magnetic field investigation, *Space Science Reviews*, 79(1), 65–91, doi:10.1023/A:1004970907748.
- Bessho, N., and A. Bhattacharjee (2014), Instability of the current sheet in the earth’s magnetotail with normal magnetic field, *Physics of Plasmas*, 21(10), 102,905, doi:10.1063/1.4899043.
- Bhattacharjee, A., Y. M. Huang, H. Yang, and B. Rogers (2009), Fast reconnection in high-Lundquist-number plasmas due to secondary tearing instabilities, in *Solar Heliospheric and INTERplanetary Environment (SHINE 2009)*, p. 161.

- Birn, J., and E. R. Priest (2007), *Reconnection of Magnetic Fields*, Cambridge University Press.
- Bishop, C. M. (1998), Bayesian pca, in *Proceedings of the 11th International Conference on Neural Information Processing Systems*, p. 382–388, MIT Press.
- Boakes, P. D., R. Nakamura, M. Volwerk, and S. E. Milan (2014), ECLAT Cluster Spacecraft Magnetotail Plasma Region Identifications (2001-2009), *Dataset Papers in Science*, 2014, 84,305, doi:10.1155/2014/684305.
- Boldyrev, S., C. Forest, and J. Egedal (2020), Electron temperature of the solar wind, *Proceedings of the National Academy of Sciences*, doi:10.1073/pnas.1917905117.
- Borg, A. L., M. G. G. T. Taylor, and J. P. Eastwood (2012), Electron pitch angle distribution during magnetic reconnection diffusion region observations in the earth’s magnetotail, *Annales Geophysicae*, 30(1), 109–117, doi:10.5194/angeo-30-109-2012.
- Buechner, J., and L. M. Zelenyi (1987), Chaotization of the electron motion as the cause of an internal magnetotail instability and substorm onset, *J. Geophys. Res.*, 92(A12), 13,456–13,466, doi:10.1029/JA092iA12p13456.
- Burch, J. L., and T. D. Phan (2016), Magnetic reconnection at the dayside magnetopause: Advances with mms, *Geophysical Research Letters*, 43(16), 8327–8338, doi:https://doi.org/10.1002/2016GL069787.
- Chandra, B., and R. K. Sharma (2014), Adaptive noise schedule for denoising autoencoder, in *Neural Information Processing*, edited by C. K. Loo, K. S. Yap, K. W. Wong, A. Teoh, and K. Huang, pp. 535–542, Springer International Publishing.

- Chandra, P., and Y. Singh (2004), An activation function adapting training algorithm for sigmoidal feedforward networks, *Neurocomputing*, 61, 429 – 437, doi:<https://doi.org/10.1016/j.neucom.2004.04.001>.
- Chao, J., D. Wu, C.-H. Lin, Y.-H. Yang, X. Wang, M. Kessel, S. Chen, and R. Lepping (2002), Models for the size and shape of the earth’s magnetopause and bow shock, in *Space Weather Study Using Multipoint Techniques, COSPAR Colloquia Series*, vol. 12, pp. 127 – 135, Pergamon.
- Che, H., and M. L. Goldstein (2014), The origin of non-maxwellian solar wind electron velocity distribution function: connection to nano flares in the solar corona, *The Astrophysical Journal*, 795(2), L38, doi:[10.1088/2041-8205/795/2/L38](https://doi.org/10.1088/2041-8205/795/2/L38).
- Chen, L.-J., M. Hesse, S. Wang, D. Gershman, R. Ergun, C. Pollock, R. Torbert, N. Bessho, W. Daughton, J. Dorelli, B. Giles, R. Strangeway, C. Russell, Y. Khotyaintsev, J. Burch, T. Moore, B. Lavraud, T. Phan, and L. Avanov (2016), Electron energization and mixing observed by mms in the vicinity of an electron diffusion region during magnetopause reconnection, *Geophysical Research Letters*, 43(12), 6036–6043, doi:<https://doi.org/10.1002/2016GL069215>.
- Chen, Q., A. Otto, and L. C. Lee (1997), Tearing instability, kelvin-helmholtz instability, and magnetic reconnection, *Journal of Geophysical Research: Space Physics*, 102(A1), 151–161, doi:[10.1029/96ja03144](https://doi.org/10.1029/96ja03144).
- Chollet, F., et al. (2015), Keras, <https://keras.io>.
- Comaniciu, D., and P. Meer (2002), Mean shift: a robust approach toward feature space

- analysis, *IEEE Transactions on Pattern Analysis and Machine Intelligence*, 24(5), 603–619.
- Coppi, B., G. Laval, and R. Pellat (1966), Dynamics of the geomagnetic tail, *Physical Review Letters*, 16(26), 1207–1210, doi:10.1103/physrevlett.16.1207.
- Cully, C. M., R. E. Ergun, and A. I. Eriksson (2007), Electrostatic structure around spacecraft in tenuous plasmas, *Journal of Geophysical Research: Space Physics*, 112(A9), doi:10.1029/2007JA012269.
- de Boer, P.-T., D. Kroese, S. Mannor, and R. Rubinstein (2005), A tutorial on the cross-entropy method, *Annals of Operations Research*, 134(1), 19–67.
- Dempster, A. P., N. M. Laird, and D. B. Rubin (1977), Maximum likelihood from incomplete data via the em algorithm, *Journal of the Royal Statistical Society: Series B (Methodological)*, 39(1), 1–22, doi:10.1111/j.2517-6161.1977.tb01600.x.
- Denton, R., B. Ö. Sonnerup, H. Hasegawa, T. Phan, C. Russell, R. Strangeway, B. Giles, D. Gershman, and R. Torbert (2016), Motion of the mms spacecraft relative to the magnetic reconnection structure observed on 16 october 2015 at 1307 ut, *Geophysical Research Letters*, 43(11), 5589–5596.
- Dungey, J. W. (1961), Interplanetary magnetic field and the auroral zones, *Phys. Rev. Lett.*, 6, 47–48.
- Dunlop, M., D. Southwood, K.-H. Glassmeier, and F. Neubauer (1988), Analysis of multi-point magnetometer data, *Advances in Space Research*, 8(9-10), 273–277.
- Dupuis, R., M. V. Goldman, D. L. Newman, J. Amaya, and G. Lapenta (2020), Character-

- izing magnetic reconnection regions using gaussian mixture models on particle velocity distributions, *The Astrophysical Journal*, 889(1), 22, doi:10.3847/1538-4357/ab5524.
- Eastwood, J. P., T. D. Phan, M. Øieroset, and M. A. Shay (2010), Average properties of the magnetic reconnection ion diffusion region in the earth's magnetotail: The 2001–2005 cluster observations and comparison with simulations, *Journal of Geophysical Research: Space Physics*, 115(A8), doi:<https://doi.org/10.1029/2009JA014962>.
- Edmondson, J. K. (2012), On the role of interchange reconnection in the generation of the slow solar wind, *Space Science Reviews*, 172(1), 209–225.
- Escoubet, C. P., R. Schmidt, and M. L. Goldstein (1997), *Cluster - Science and Mission Overview*, pp. 11–32, Springer Netherlands.
- Escoubet, C. P., M. Fehringer, and M. Goldstein (2001), Introduction: The Cluster mission, *Annales Geophysicae*, 19(10/12), 1197–1200.
- Farnell, C. C., C. C. Farnell, S. C. Farnell, and J. D. Williams (2017), Recommended practice for use of electrostatic analyzers in electric propulsion testing, *Journal of Propulsion and Power*, 33(3), 638–658, doi:10.2514/1.B35413.
- Fazakerley, A. N., A. D. Lahiff, R. J. Wilson, I. Rozum, C. Anekallu, M. West, and H. Bacai (2010), Peace data in the cluster active archive, in *The Cluster Active Archive*, edited by H. Laakso, M. Taylor, and C. P. Escoubet, pp. 129–144, Springer Netherlands.
- Feldman, U., E. Landi, and N. A. Schwadron (2005), On the sources of fast and slow solar wind, *Journal of Geophysical Research: Space Physics*, 110(A7), doi:10.1029/2004JA010918.

- Feldman, W. C., J. R. Asbridge, S. J. Bame, M. D. Montgomery, and S. P. Gary (1975), Solar wind electrons, *Journal of Geophysical Research (1896-1977)*, *80*(31), 4181–4196, doi:10.1029/JA080i031p04181.
- Feldman, W. C., J. R. Asbridge, S. J. Bame, J. T. Gosling, and D. S. Lemons (1978), Characteristic electron variations across simple high-speed solar wind streams, *Journal of Geophysical Research: Space Physics*, *83*(A11), 5285–5295, doi:10.1029/JA083iA11p05285.
- Fitzenreiter, R. J., K. W. Ogilvie, D. J. Chornay, and J. Keller (1998), Observations of electron velocity distribution functions in the solar wind by the wind spacecraft: High angular resolution strahl measurements, *Geophysical Research Letters*, *25*(3), 249–252, doi:10.1029/97GL03703.
- Flach, P. A., and M. Kull (2015), Precision-recall-gain curves: Pr analysis done right, *Proceedings of the 28th International Conference on Neural Information Processing Systems*, *1*, 838–846.
- Forsyth, C., M. Lester, R. C. Fear, E. Lucek, I. Dandouras, A. N. Fazakerley, H. Singer, and T. K. Yeoman (2009), Solar wind and substorm excitation of the wavy current sheet, *Annales Geophysicae*, *27*(6), 2457–2474, doi:10.5194/angeo-27-2457-2009.
- Forsyth, C., I. J. Rae, J. C. Coxon, M. P. Freeman, C. M. Jackman, J. Gjerloev, and A. N. Fazakerley (2015), A new technique for determining Substorm Onsets and Phases from Indices of the Electrojet (SOPHIE), *Journal of Geophysical Research (Space Physics)*, *120*(12), 10,592–10,606, doi:10.1002/2015JA021343.
- Fukunaga, K., and L. Hostetler (1975), The estimation of the gradient of a density function,

- with applications in pattern recognition, *IEEE Transactions on Information Theory*, 21(1), 32–40.
- Furth, H. P. (1963), Prevalent instability of nonthermal plasmas, *The Physics of Fluids*, 6(1), 48–57, doi:10.1063/1.1724507.
- Galeev, A. A., and L. M. Zelenii (1976), Tearing instability in plasma configurations.
- Gary, S., E. Scime, J. Phillips, and W. Feldman (1994), The whistler heat flux instability: Threshold conditions in the solar wind, *Journal of Geophysical Research*, 99(A12), doi:10.1029/94JA02067.
- Geiss, J., G. Gloeckler, and R. von Steiger (1995), Origin of the Solar Wind From Composition Data, *Space Sci Rev*, 72(1-2), 49–60, doi:10.1007/BF00768753.
- Gekelman, W., and H. Pfister (1988), Experimental observations of the tearing of an electron current sheet, *The Physics of Fluids*, 31(7), 2017–2025, doi:10.1063/1.866650.
- Gekelman, W., H. Pfister, and J. R. Kan (1991), Experimental observations of patchy reconnections associated with the three-dimensional tearing instability, *Journal of Geophysical Research: Space Physics*, 96(A3), 3829–3833, doi:https://doi.org/10.1029/90JA02630.
- Gekelman, W., H. Pfister, and J. Kan (1991), Experimental observations of patchy reconnections associated with the three-dimensional tearing instability, *JGR*, 96(A3), 3829–3833, doi:10.1029/90JA02630.
- Gjerloev, J. W. (2012), The SuperMAG data processing technique, *Journal of Geophysical Research (Space Physics)*, 117(A9), A09213, doi:10.1029/2012JA017683.

- Gosling, J. T., D. N. Baker, S. J. Bame, W. C. Feldman, R. D. Zwickl, and E. J. Smith (1987), Bidirectional solar wind electron heat flux events, *Journal of Geophysical Research: Space Physics*, *92*(A8), 8519–8535, doi:10.1029/JA092iA08p08519.
- Graham, G. (2018), The evolution of solar wind strahl, Ph.D. thesis, University College London.
- Graham, G. A., I. J. Rae, C. J. Owen, A. P. Walsh, C. S. Arridge, L. Gilbert, G. R. Lewis, G. H. Jones, C. Forsyth, A. J. Coates, and J. H. Waite (2017), The evolution of solar wind strahl with heliospheric distance, *Journal of Geophysical Research: Space Physics*, *122*(4), 3858–3874, doi:10.1002/2016JA023656.
- Graham, G. A., I. J. Rae, C. J. Owen, and A. P. Walsh (2018), Investigating the effect of IMF path length on pitch-angle scattering of strahl within 1 au, *The Astrophysical Journal*, *855*(1), 40, doi:10.3847/1538-4357/aaaf1b.
- Gurgiolo, C., and M. L. Goldstein (2017), Absence of the strahl during times of slow wind, *Annales Geophysicae*, *35*(1), 71–85, doi:10.5194/angeo-35-71-2017.
- Gustafsson, G., M. André, T. Carozzi, A. I. Eriksson, C.-G. Fälthammar, R. Grard, G. Holmgren, J. A. Holtet, N. Ivchenko, T. Karlsson, Y. Khotyaintsev, S. Klimov, H. Laakso, P.-A. Lindqvist, B. Lybekk, G. Marklund, F. Mozer, K. Mursula, A. Pedersen, B. Popielawska, S. Savin, K. Stasiewicz, P. Tanskanen, A. Vaivads, and J.-E. Wahlund (2001), First results of electric field and density observations by Cluster EFW based on initial months of operation, *Annales Geophysicae*, *19*(10/12), 1219–1240.
- Guyon, I. (1997), A scaling law for the validation-set training-set size ratio, in *AT & T Bell Laboratories*.

- Habbal, S. R., R. Woo, S. Fineschi, R. O. Neal, J. Kohl, G. Noci, and C. Korendyke (1997), Origins of the slow and the ubiquitous fast solar wind, *The Astrophysical Journal*, 489(1), L103–L106, doi:10.1086/310970.
- Hahnloser, R., R. Sarpeshkar, M. Mahowald, R. Douglas, and H. Seung (2000), Digital selection and analogue amplification coexist in a cortex- inspired silicon circuit, *Nature*, 405(6789), 947–951, doi:10.1038/35016072.
- Hammond, C., W. Feldman, D. McComas, J. Phillips, and R. Forsyth (1996), Variation of electron-strahl width in the high-speed solar wind: ULYSSES observations., *aap*, 316, 350–354.
- Hapgood, M., C. Perry, J. Davies, and M. Denton (2011), The role of suprathermal particle measurements in crossscale studies of collisionless plasma processes, *Planetary and Space Science*, 59(7), 618 – 629, doi:https://doi.org/10.1016/j.pss.2010.06.002, cross-Scale Coupling in Plasmas.
- Hinton, G. E., and R. R. Salakhutdinov (2006), Reducing the dimensionality of data with neural networks, *Science*, 313(5786), 504–507, doi:10.1126/science.1127647.
- Horaites, K., S. Boldyrev, and M. V. Medvedev (2019), Electron strahl and halo formation in the solar wind, *MNRAS*, 484(2), 2474–2481, doi:10.1093/mnras/sty3504.
- Hughes, W. J. (1995), The magnetopause, magnetotail, and magnetic reconnection, in *Introduction to Space Physics*, edited by M. G. Kivelson and C. T. Russell, chap. 9, pp. 227–288, Cambridge University Press.
- Hwang, K.-J., M. L. Goldstein, D. E. Wendel, A. N. Fazakerley, and C. Gurgiolo (2013), Cluster observations near reconnection x lines in earth’s magnetotail current sheet, *Journal of*

- Geophysical Research: Space Physics*, 118(7), 4199–4209, doi:<https://doi.org/10.1002/jgra.50403>.
- Ishizawa, A., and N. Nakajima (2010), Turbulence driven magnetic reconnection causing long-wavelength magnetic islands, *Physics of Plasmas*, 17(7), 072,308.
- Janocha, K., and W. M. Czarnecki (2017), On loss functions for deep neural networks in classification, *arXiv*.
- Johnstone, A. D., C. Alsop, S. Burge, P. J. Carter, A. J. Coates, A. J. Coker, A. N. Fazakerley, M. Grande, R. A. Gowen, C. Gurgiolo, B. K. Hancock, B. Narheim, A. Preece, P. H. Sheather, J. D. Winningham, and R. D. Woodliffe (1997), *Peace: A Plasma Electron and Current Experiment*, pp. 351–398, Springer Netherlands, Dordrecht.
- Jr., F. J. M. (1951), The kolmogorov-smirnov test for goodness of fit, *Journal of the American Statistical Association*, 46(253), 68–78, doi:10.1080/01621459.1951.10500769.
- Kajdič, P., O. Alexandrova, M. Maksimovic, C. Lacombe, and A. N. Fazakerley (2016), Suprathermal Electron Strahl Widths in the Presence of Narrow-band Whistler Waves in the Solar Wind, *ApJ*, 833(2), 172, doi:10.3847/1538-4357/833/2/172.
- Karimabadi, H., J. D. Huba, D. Krauss-Varban, and N. Omidi (2004), On the generation and structure of the quadrupole magnetic field in the reconnection process: Comparative simulation study, *GRL*, 31(7), L07806, doi:10.1029/2004GL019553.
- Kepko, L., N. M. Viall, S. K. Antiochos, S. T. Lepri, J. C. Kasper, and M. Weberg (2016), Implications of l1 observations for slow solar wind formation by solar reconnection, *Geophysical Research Letters*, 43(9), 4089–4097, doi:10.1002/2016GL068607.

- Khandelwal, R. (2019), Overview of different optimizers for neural networks, <https://medium.com/datadriveninvestor/overview-of-different-optimizers-for-neural-networks-e0ed119440c3>, [Accessed: 01.07.2020].
- Kohavi, R. (1995), A study of cross-validation and bootstrap for accuracy estimation and model selection, *Proceedings of the 14th International Joint Conference on Artificial Intelligence*, 2, 1137–1143.
- Kube, R., F. M. Bianchi, D. Brunner, and B. LaBombard (2019), Outlier classification using autoencoders: Application for fluctuation driven flows in fusion plasmas, *Review of Scientific Instruments*, 90(1), 013,505, doi:10.1063/1.5049519.
- Laakso, H., C. Perry, S. McCaffrey, D. Herment, A. J. Allen, C. C. Harvey, C. P. Escoubet, C. Gruenberger, M. G. G. T. Taylor, and R. Turner (2010), Cluster active archive: Overview, in *The Cluster Active Archive*, edited by H. Laakso, M. Taylor, and C. P. Escoubet, pp. 3–37, Springer Netherlands.
- Lance, G. N., and W. T. Williams (1967), A General Theory of Classificatory Sorting Strategies: 1. Hierarchical Systems, *The Computer Journal*, 9(4), 373–380, doi:10.1093/comjnl/9.4.373.
- Landi, S., L. Matteini, and F. Pantellini (2012), On the competition between radial expansion and coulomb collisions in shaping the electron velocity distribution function: Kinetic simulations, *The Astrophysical Journal*, 760(2), 143, doi:10.1088/0004-637x/760/2/143.
- Landi, S., L. D. Zanna, E. Papini, F. Pucci, and M. Velli (2015), RESISTIVE MAGNETOHY-

- DRODYNAMICS SIMULATIONS OF THE IDEAL TEARING MODE, *The Astrophysical Journal*, 806(1), 131, doi:10.1088/0004-637x/806/1/131.
- Le, L., A. Patterson, and M. White (2018), Supervised autoencoders: Improving generalization performance with unsupervised regularizers, in *Advances in Neural Information Processing Systems 31*, pp. 107–117, Curran Associates, Inc.
- Lie-Svendsen, Ø., V. H. Hansteen, and E. Leer (1997), Kinetic electrons in high-speed solar wind streams: Formation of high-energy tails, *Journal of Geophysical Research: Space Physics*, 102(A3), 4701–4718, doi:10.1029/96JA03632.
- Liu, C. M., H. S. Fu, Y. Y. Liu, Z. Wang, G. Chen, Y. Xu, and Z. Z. Chen (2020), Electron pitch-angle distribution in earth’s magnetotail: Pancake, cigar, isotropy, butterfly, and rolling-pin, *Journal of Geophysical Research: Space Physics*, 125(4), doi:10.1029/2020JA027777.
- Liu, Y.-H., J. Birn, W. Daughton, M. Hesse, and K. Schindler (2014), Onset of reconnection in the near magnetotail: Pic simulations, *Journal of Geophysical Research: Space Physics*, 119(12), 9773–9789, doi:https://doi.org/10.1002/2014JA020492.
- Lu, S., V. Angelopoulos, A. V. Artemyev, P. L. Pritchett, J. Liu, A. Runov, A. Tenerani, C. Shi, and M. Velli (2019), Turbulence and Particle Acceleration in Collisionless Magnetic Reconnection: Effects of Temperature Inhomogeneity across Pre-reconnection Current Sheet, *ApJ*, 878(2), 109, doi:10.3847/1538-4357/ab1f6b.
- Lui, A. T. Y. (1987), *Road map to magnetotail domains.*, pp. 3–5, John Hopkins University Press.
- Lukasová, A. (1979), Hierarchical agglomerative clustering procedure, *Pattern Recognition*, 11(5), 365 – 381, doi:https://doi.org/10.1016/0031-3203(79)90049-9.

- Maksimovic, M., I. Zouganelis, J.-Y. Chaufray, K. Issautier, E. E. Scime, J. E. Littleton, E. Marsch, D. J. McComas, C. Salem, R. P. Lin, and H. Elliott (2005), Radial evolution of the electron distribution functions in the fast solar wind between 0.3 and 1.5 au, *Journal of Geophysical Research: Space Physics*, *110*(A9), doi:10.1029/2005JA011119.
- Markidis, S., P. Henri, G. Lapenta, A. Divin, M. V. Goldman, D. Newman, and S. Eriksson (2012), Collisionless magnetic reconnection in a plasmoid chain, *Nonlinear Processes in Geophysics*, *19*(1), 145–153, doi:10.5194/npg-19-145-2012.
- Marsch, E., and H. Goldstein (1983), The effects of coulomb collisions on solar wind ion velocity distributions, *Journal of Geophysical Research: Space Physics*, *88*(A12), 9933–9940, doi:10.1029/JA088iA12p09933.
- McComas, D. J., S. J. Bame, W. C. Feldman, J. T. Gosling, and J. L. Phillips (1992), Solar wind halo electrons from 1–4 au, *Geophysical Research Letters*, *19*(12), 1291–1294, doi:10.1029/92GL00631.
- McComas, D. J., S. J. Bame, B. L. Barraclough, W. C. Feldman, H. O. Funsten, J. T. Gosling, P. Riley, R. Skoug, A. Balogh, R. Forsyth, B. E. Goldstein, and M. Neugebauer (1998), Ulysses’ return to the slow solar wind, *Geophysical Research Letters*, *25*(1), 1–4, doi:10.1029/97GL03444.
- McLachlan, G., and D. Peel (2000), *ML Fitting of Mixture Models*, chap. 2, pp. 40–80, John Wiley & Sons, Ltd, doi:10.1002/0471721182.ch2.
- Mcpherron, R. L., C. T. Russell, and M. P. Aubry (1973), Satellite studies of magnetospheric substorms on august 15, 1968: 9. phenomenological model for substorms, *Journal of Geophysical Research*, *78*(16), 3131–3149, doi:10.1029/ja078i016p03131.

- Mirkes, E. (2011), KNN and Potential Energy: applet., <http://www.math.le.ac.uk/people/ag153/homepage/KNN/KNN3.html>, accessed: 2019-10-18.
- Nagai, T., I. Shinohara, M. Fujimoto, M. Hoshino, Y. Saito, S. Machida, and T. Mukai (2001), Geotail observations of the hall current system: Evidence of magnetic reconnection in the magnetotail, *Journal of Geophysical Research: Space Physics*, *106*(A11), 25,929–25,949, doi:<https://doi.org/10.1029/2001JA900038>.
- Øieroset, M., T. D. Phan, M. Fujimoto, R. P. Lin, and R. P. Lepping (2001), In situ detection of collisionless reconnection in the Earth’s magnetotail, *Nature*, *412*(6845), 414–417, doi:10.1038/35086520.
- Øieroset, M., R. P. Lin, T. D. Phan, D. E. Larson, and S. D. Bale (2002), Evidence for electron acceleration up to ~ 300 keV in the magnetic reconnection diffusion region of earth’s magnetotail, *Phys. Rev. Lett.*, *89*, 195,001, doi:10.1103/PhysRevLett.89.195001.
- Owens, M. J., and R. J. Forsyth (2013), The heliospheric magnetic field, *Living Reviews in Solar Physics*, *10*(1), 5, doi:10.12942/lrsp-2013-5.
- Owens, M. J., N. U. Crooker, and N. A. Schwadron (2008), Suprathermal electron evolution in a parker spiral magnetic field, *Journal of Geophysical Research: Space Physics*, *113*(A11), doi:10.1029/2008JA013294.
- Pagel, C., S. P. Gary, C. A. de Koning, R. M. Skoug, and J. T. Steinberg (2007), Scattering of suprathermal electrons in the solar wind: Ace observations, *Journal of Geophysical Research: Space Physics*, *112*(A4), doi:10.1029/2006JA011967.
- Parker, E. N. (1963), *Interplanetary dynamical processes.*, Interscience Publishers, New York.

- Patil, P. (2018), K Means Clustering : Identifying F.R.I.E.N.D.S in the World of Strangers, <https://towardsdatascience.com/>, accessed: 2010-09-30.
- Pedregosa, F., G. Varoquaux, A. Gramfort, V. Michel, B. Thirion, O. Grisel, M. Blondel, P. Prettenhofer, R. Weiss, V. Dubourg, J. Vanderplas, A. Passos, D. Cournapeau, M. Brucher, M. Perrot, and E. Duchesnay (2011), Scikit-learn: Machine learning in Python, *Journal of Machine Learning Research*, 12, 2825–2830.
- Peerenboom, K., A. Parente, T. Kozák, A. Bogaerts, and G. Degrez (2015), Dimension reduction of non-equilibrium plasma kinetic models using principal component analysis, *Plasma Sources Science and Technology*, 24(2), 025,004, doi:10.1088/0963-0252/24/2/025004.
- Pellat, R., F. V. Coroniti, and P. L. Pritchett (1991), does ion tearing exist?, *Geophysical Research Letters*, 18(2), 143–146, doi:https://doi.org/10.1029/91GL00123.
- Perri, S., F. Valentini, L. Sorriso-Valvo, A. Reda, and F. Malara (2017), On the estimation of the current density in space plasmas: Multi-versus single-point techniques, *Planetary and Space Science*, 140, 6–10.
- Peterson, L. (2009), K-nearest neighbor, *Scholarpedia*, 4(2), 1883, doi:10.4249/scholarpedia.1883.
- Pierrard, V., M. Maksimovic, and J. Lemaire (2001), Core, halo and strahl electrons in the solar wind, *Astrophysics and Space Science*, 277(1), 195–200, doi:10.1023/A:1012218600882.
- Pilipp, W. G., H. Miggenrieder, M. D. Montgomery, K. H. Mühlhäuser, H. Rosenbauer, and R. Schwenn (1987a), Characteristics of electron velocity distribution functions in the solar

- wind derived from the helios plasma experiment, *Journal of Geophysical Research: Space Physics*, 92(A2), 1075–1092, doi:10.1029/JA092iA02p01075.
- Pilipp, W. G., H. Miggenrieder, K. H. Mühlhäuser, H. Rosenbauer, R. Schwenn, and F. M. Neubauer (1987b), Variations of electron distribution functions in the solar wind, *Journal of Geophysical Research: Space Physics*, 92(A2), 1103–1118, doi:10.1029/JA092iA02p01103.
- Pilipp, W. G., H. Miggenrieder, K.-H. Mühläuser, H. Rosenbauer, and R. Schwenn (1990), Large-scale variations of thermal electron parameters in the solar wind between 0.3 and 1 au, *Journal of Geophysical Research: Space Physics*, 95(A5), 6305–6329, doi:10.1029/JA095iA05p06305.
- Qian, Y., W. Zhou, J. Yan, W. Li, and L. Han (2015), Comparing machine learning classifiers for object-based land cover classification using very high resolution imagery, *Remote Sensing*, 7(1), 153–168, doi:10.3390/rs70100153.
- Rème, H., J. M. Bosqued, J. A. Sauvaud, A. Cros, J. Dandouras, C. Aoustin, J. Bouyssou, T. Camus, J. Cuvilo, C. Martz, J. L. Médale, H. Perrier, D. Romefort, J. Rouzaud, C. d’Uston, E. Möbius, K. Crocker, M. Granoff, L. M. Kistler, M. Popecki, D. Hovestadt, B. Klecker, G. Paschmann, M. Scholer, C. W. Carlson, D. W. Curtis, R. P. Lin, J. P. McFadden, V. Formisano, E. Amata, M. B. Bavassano-Cattaneo, P. Baldetti, G. Belluci, R. Bruno, G. Chionchio, A. Di Lellis, E. G. Shelley, A. G. Ghielmetti, W. Lennartsson, A. Korth, H. Rosenbauer, R. Lundin, S. Olsen, G. K. Parks, M. McCarthy, and H. Balsiger (1997), *The Cluster Ion Spectrometry (CIS) Experiment*, pp. 303–350, Springer Netherlands, doi:10.1007/978-94-011-5666-0_12.

Rème, H., C. Aoustin, J. M. Bosqued, I. Dandouras, B. Lavraud, J. A. Sauvaud, A. Barthe, J. Bouyssou, T. Camus, O. Coeur-Joly, A. Cros, J. Cuvilo, F. Ducay, Y. Garbarowitz, J. L. Medale, E. Penou, H. Perrier, D. Romefort, J. Rouzaud, C. Vallat, D. Alcaydé, C. Jacquey, C. Mazelle, C. D’Uston, E. Möbius, L. M. Kistler, K. Crocker, M. Granoff, C. Mouikis, M. Popecki, M. Vosbury, B. Klecker, D. Hovestadt, H. Kucharek, E. Kuenneth, G. Paschmann, M. Scholer, N. Sckopke, E. Seidenschwang, C. W. Carlson, D. W. Curtis, C. Ingraham, R. P. Lin, J. P. McFadden, G. K. Parks, T. Phan, V. Formisano, E. Amata, M. B. Bavassano-Cattaneo, P. Baldetti, R. Bruno, G. Chionchio, A. Di Lellis, M. F. Mar-cucci, G. Pallochia, A. Korth, P. W. Daly, B. Graeve, H. Rosenbauer, V. Vasyliunas, M. Mc-carthy, M. Wilber, L. Eliasson, R. Lundin, S. Olsen, E. G. Shelley, S. Fuselier, A. G. Ghiel-metti, W. Lennartsson, C. P. Escoubet, H. Balsiger, R. Friedel, J.-B. Cao, R. A. Kovrazhkin, I. Papamastorakis, R. Pellat, J. Scudder, and B. Sonnerup (2001), First multispacecraft ion measurements in and near the Earth’s magnetosphere with the identical Cluster ion spec-trometry (CIS) experiment, *Annales Geophysicae*, 19(10/12), 1303–1354.

Rice, W. R. (1990), A consensus combined p-value test and the family-wide significance of component tests, *Biometrics*, 46(2), 303–308, doi:10.2307/2531435.

Ruder, S. (2016), An overview of gradient descent optimization algorithms, *arXiv e-prints*.

Russel, C. T. (2011), Catching Space Weather in the Act, https://www.nasa.gov/mission_pages/ibex/news/spaceweather.html, accessed: 2022-12-06.

Saito, M. (2015), THEMIS two-point measurements of the cross-tail current density: A thick bifurcated current sheet in the near-Earth plasma sheet, *Journal of Geophysical Research (Space Physics)*, 120(8), 6258–6275, doi:10.1002/2015JA021142.

- Saito, S., and S. P. Gary (2007), All whistlers are not created equally: Scattering of strahl electrons in the solar wind via particle-in-cell simulations, *Geophysical Research Letters*, 34(1), doi:10.1029/2006GL028173.
- Sakurada, M., and T. Yairi (2014), Anomaly detection using autoencoders with nonlinear dimensionality reduction, in *Proceedings of the MLSDA 2014 2nd Workshop on Machine Learning for Sensory Data Analysis*, p. 4–11, Association for Computing Machinery, doi: 10.1145/2689746.2689747.
- Salem, C., D. Hubert, C. Lacombe, S. D. Bale, A. Mangeney, D. E. Larson, and R. P. Lin (2003), Electron properties and coulomb collisions in the solar wind at 1 au: Wind observations, *The Astrophysical Journal*, 585(2), 1147–1157, doi:10.1086/346185.
- Sarkar, D., R. Bali, and T. Sharma (2018), *Machine Learning Basics*, pp. 3–65, Apress, Berkeley, CA, doi:10.1007/978-1-4842-3207-1_1.
- Schindler, K., D. Pfirsch, and H. Wobig (1973), Stability of two-dimensional collision-free plasmas, *Plasma Physics*, 15(12), 1165–1184, doi:10.1088/0032-1028/15/12/001.
- Scikit-Learn (2007), Cross-validation: evaluating estimator performance, https://scikit-learn.org/stable/modules/cross_validation.html, accessed: 2019-10-21.
- Scime, E. E., S. J. Bame, W. C. Feldman, S. P. Gary, J. L. Phillips, and A. Balogh (1994), Regulation of the solar wind electron heat flux from 1 to 5 au: Ulysses observations, *Journal of Geophysical Research: Space Physics*, 99(A12), 23,401–23,410, doi:10.1029/94JA02068.
- SciPy (2016), `scipy.optimize`, https://docs.scipy.org/doc/scipy-0.18.1/reference/generated/scipy.optimize.curve_fit.html, accessed: 2019-10-27.

- Scudder, J. D. (1992), On the Causes of Temperature Change in Inhomogeneous Low-Density Astrophysical Plasmas, *ApJ*, 398, 299, doi:10.1086/171858.
- Scudder, J. D., and S. Olbert (1979), A theory of local and global processes which affect solar wind electrons, 1. the origin of typical 1 au velocity distribution functions—steady state theory, *Journal of Geophysical Research: Space Physics*, 84(A6), 2755–2772, doi:10.1029/JA084iA06p02755.
- Sergeev, V., A. Runov, W. Baumjohann, R. Nakamura, T. L. Zhang, M. Volwerk, A. Balogh, H. Rème, J. A. Sauvaud, M. André, and B. Klecker (2003), Current sheet flapping motion and structure observed by Cluster, *GRL*, 30(6), 1327, doi:10.1029/2002GL016500.
- Sharma, A. S., and S. A. Curtis (2005), *Magnetospheric Multiscale Mission*, pp. 179–195, Springer Netherlands, doi:10.1007/1-4020-3109-2_8.
- Sitnov, M., J. Birn, B. Ferdousi, E. Gordeev, Y. Khotyaintsev, V. Merkin, T. Motoba, A. Otto, E. Panov, P. Pritchett, and et al. (2019), Explosive magnetotail activity, *Space Science Reviews*, 215(4), doi:10.1007/s11214-019-0599-5.
- Sonnerup, B., and M. Scheible (1998), Analysis methods for multi-spacecraft data, *ISSI Scientific Report*.
- Tallarida, R. J., and R. B. Murray (1987), *Chi-Square Test*, pp. 140–142, Springer New York, New York, NY, doi:10.1007/978-1-4612-4974-0_43.
- Thompson, S., M. Kivelson, K. Khurana, R. McPherron, J. Weygand, A. Balogh, H. Reme, and L. Kistler (2005), Dynamic harris current sheet thickness from cluster current density and plasma measurements, *Journal of Geophysical Research: Space Physics*, 110(A2).

- Vallantin, L. (2018), Why you should not trust only in accuracy to measure machine learning performance, <https://medium.com/@limavallantin/>, accessed: 2019-10-21.
- Vasko, I. Y., V. Krasnoselskikh, Y. Tong, S. D. Bale, J. W. Bonnell, and F. S. Mozer (2019), Whistler fan instability driven by strahl electrons in the solar wind, *The Astrophysical Journal*, 871(2), L29, doi:10.3847/2041-8213/ab01bd.
- Verscharen, D., B. D. G. Chandran, S.-Y. Jeong, C. S. Salem, M. P. Pulupa, and S. D. Bale (2019), Self-induced scattering of strahl electrons in the solar wind, *The Astrophysical Journal*, 886(2), 136, doi:10.3847/1538-4357/ab4c30.
- Vinas, A. F., H. K. Wong, and A. J. Klimas (2000), Generation of electron suprathermal tails in the upper solar atmosphere: Implications for coronal heating, *The Astrophysical Journal*, 528(1), 509–523, doi:10.1086/308151.
- Vocks, C., C. Salem, R. P. Lin, and G. Mann (2005), Electron halo and strahl formation in the solar wind by resonant interaction with whistler waves, *The Astrophysical Journal*, 627(1), 540–549, doi:10.1086/430119.
- Vocks, C., G. Mann, and G. Rausche (2008), Formation of suprathermal electron distributions in the quiet solar corona, *ApJ*, 480, 527–536, doi:10.1051/0004-6361:20078826.
- Walker, J., S. Boldyrev, and N. F. Loureiro (2018), Influence of tearing instability on magnetohydrodynamic turbulence, *PRE*, 98(3), 033209, doi:10.1103/PhysRevE.98.033209.
- Walsh, A. P. (2009), New perspectives on magnetotail dynamic processes from combined cluster and double star observations, Ph.D. thesis, University College London.
- Walsh, A. P., C. J. Owen, A. N. Fazakerley, C. Forsyth, and I. Dandouras (2011), Average

- magnetotail electron and proton pitch angle distributions from cluster peace and cis observations, *Geophysical Research Letters*, 38(6), doi:10.1029/2011GL046770.
- Walsh, A. P., A. N. Fazakerley, C. Forsyth, C. J. Owen, M. G. G. T. Taylor, and I. J. Rae (2013), Sources of electron pitch angle anisotropy in the magnetotail plasma sheet, *Journal of Geophysical Research: Space Physics*, 118(10), 6042–6054, doi:10.1002/jgra.50553.
- Wang, S., L. C. Lee, and C. Q. Wei (1988), Streaming tearing instability in the current sheet with a super-Alfvénic flow, *Physics of Fluids*, 31(6), 1544–1548, doi:10.1063/1.866693.
- Wang, Y.-M., J. N. R. Sheeley, J. L. Phillips, and B. E. Goldstein (1997), Solar wind stream interactions and the wind speed–expansion factor relationship, *The Astrophysical Journal*, 488(1), L51–L54.
- Ward, J. H. (1963), Hierarchical grouping to optimize an objective function, *Journal of the American Statistical Association*, 58(301), 236–244, doi:10.1080/01621459.1963.10500845.
- Wüest, M., D. S. Evans, and R. von Steiger (2007), *Calibration of Particle Instruments in Space Physics*, 189 pp., International Space Science Institute by ESA Communications.
- Zanna, L. D., S. Landi, E. Papini, F. Pucci, and M. Velli (2016), The ideal tearing mode: theory and resistive MHD simulations, *Journal of Physics: Conference Series*, 719, 012,016, doi:10.1088/1742-6596/719/1/012016.
- Zeiler, A., D. Biskamp, J. F. Drake, B. N. Rogers, M. A. Shay, M. Swisdak, and M. Scholer (2001), Three-dimensional particle simulations of collisionless magnetic reconnection, in *APS Division of Plasma Physics Meeting Abstracts, APS Meeting Abstracts*, vol. 43.
- Zeiler, M. D. (2012), Adadelta: An adaptive learning rate method, *arXiv e-prints*.

- Zhang, J., Z. Wang, and N. Verma (2017), In-memory computation of a machine-learning classifier in a standard 6t sram array, *IEEE Journal of Solid-State Circuits*, 52(4), 915–924, doi:10.1109/JSSC.2016.2642198.
- Zirker, J. B. (1977), Coronal holes and high-speed wind streams, *Reviews of Geophysics*, 15(3), 257–269, doi:10.1029/RG015i003p00257.
- Štverák, Š., P. Trávníček, M. Maksimovic, E. Marsch, A. N. Fazakerley, and E. E. Scime (2008), Electron temperature anisotropy constraints in the solar wind, *Journal of Geophysical Research: Space Physics*, 113(A3), doi:10.1029/2007JA012733.
- Štverák, Š., M. Maksimovic, P. M. Trávníček, E. Marsch, A. N. Fazakerley, and E. E. Scime (2009), Radial evolution of nonthermal electron populations in the low-latitude solar wind: Helios, cluster, and ulysses observations, *Journal of Geophysical Research: Space Physics*, 114(A5), doi:10.1029/2008JA013883.